A FAST VECTOR RADIATIVE TRANSFER MODEL FOR POLARIMETRIC REMOTE SENSING

A Dissertation

by

JIACHEN DING

Submitted to the Office of Graduate and Professional Studies of
Texas A&M University
in partial fulfillment of the requirements for the degree of

DOCTOR OF PHILOSOPHY

Chair of Committee,	Ping Yang
Co-Chair of Committee,	Andrew Dessler
Committee Members,	Kenneth Bowman
	Anita Rapp
	Edward Fry
Head of Department,	Ramalingam Saravanan

May 2019

Major Subject: Atmospheric Sciences

ABSTRACT

Polarimetric remote sensing technologies have been demonstrated to be irreplaceable and effective for inferring cloud, aerosol, and ocean properties. To infer atmospheric and oceanic constituent properties from observational data, an efficient and accurate retrieval algorithm is needed. The accuracy and efficiency of the retrieval algorithm depends on the radiative transfer model (RTM) used in the forward calculations involved in implementing the retrieval algorithm.

If a radiative transfer calculation is implemented in-line as part of a retrieval algorithm, rather than simply generating and interpolating from a look-up table, the atmospheric profiles and surface properties can be directly incorporated into the retrieval system to improve accuracy. Some interpolation errors can also be avoided. However, an in-line radiative transfer calculation usually does not satisfy computational efficiency requirements for an operational remote sensing application. To fully exploit the capability of satellite polarimetric instruments, it is imperative to develop an accurate and fast vector RTM.

The reported research develops a fast vector RTM in support of atmospheric and oceanic polarimetric remote sensing. This model is capable of simulating the Stokes vector observed at the top of the atmosphere and at the terrestrial surface by considering absorption, scattering, and emission in the atmosphere and ocean. Gas absorption is parameterized in terms of gas concentration, temperature, and pressure. The parameterization scheme uses a regression method and can be easily applied to an inhomogeneous atmospheric path. An efficient two-component approach combining the small-angle approximation and the adding-doubling method is utilized to solve the vector radiative transfer equation (RTE). The thermal emission source is approximated as a linear function of optical thickness in homogeneous layers. Based on this approximation, the thermal emission component of the RTE solution can be obtained by an efficient doubling process. The air-sea interface is treated as a wind-ruffled rough surface in the model to mimic a realistic ocean surface. Several bio-optical models are introduced to model ocean inherent optical properties.

It is shown that the developed RTM can be used in a retrieval algorithm by comparing the simulation results with observations by POLDER and MODIS satellite instruments.

DEDICATION

To my parents and Jinyang Han

ACKNOWLEDGEMENTS

I would like to express my sincere gratitude to my committee chair Dr. Ping Yang. His insightful and experienced guidance not only taught me a lot in my field of study, but also inspired me to find methodologies to learn new knowledge and to explore the unknown. His long-term encouragement and support gave me confidence to overcome the difficulties during study and research.

I am grateful to my committee members, Dr. Andrew Dessler, Dr. Kenneth Bowman, Dr. Anita Rapp, and Dr. Edward Fry. Their constructive comments and suggestions on my research helped me broaden my understanding of my research and related topics. I would also express my appreciation to Dr. Michael King for his significant suggestions and answers on some problems and questions I encountered during the research. Special thanks are given to Dr. Steven Schroeder, who helped me a lot in improving my English writing.

I appreciated and enjoyed communicating with all my current and previous group members at Texas A&M University, which not only helped me in study and research, but also made me feel I am staying in a friendly environment. I am also thankful to my friends for their friendship.

Finally, I am thankful to my parents, my fiancée, Jinyang Han, and other relatives, for their support and love.

CONTRIBUTORS AND FUNDING SOURCES

Contributors

This work was supervised by a dissertation committee consisting of Professors Ping Yang, Andrew Dessler, Kenneth Bowman and Anita Rapp of the Department of Atmospheric Sciences, and Professor Edward Fry of the Department of Physics & Astronomy.

All work for the dissertation was completed by the student under the guidance of Dr. Ping Yang of the Department of Atmospheric Sciences.

Funding Sources

The research reported in this dissertation was partly supported by a NASA grant NNX15AG66G.

NOMENCLATURE

3MI	Multi-Viewing -Channel -Polarisation Imager
ACE	Aerosol/Cloud/Ecosystem Mission
AD	Adding-Doubling
AirMSPI	Airborne Multiangle SpectroPolarimetric Imager
AOS	Atmosphere-Ocean System
BRDF	Bidirectional Reflectance Distribution Function
BT	Brightness Temperature
BTD	Brightness Temperature Difference
BTDF	Bidirectional Transmission Distribution Function
CAOT	Channel-Averaged Optical Thickness
CAT	Channel-Averaged Transmittance
CDOM	Colored Dissolved Organic Matter
CKD	Correlated K-Distribution
COT	Cloud Optical Thickness
DISORT	Discrete Ordinate Radiative Transfer
DMM	Delta-M Truncation Method
DO	Discrete Ordinate
GSF	General Spherical Functions
IITM	Invariant Imbedding T-Matrix
IOP	Inherent Optical Property

IR	Infrared
LBL	Line-by-line
LBLRTM	Line-by-line Radiative Transfer Model
LTE	Local Thermal Equilibrium
LUT	Look-Up Table
MAIA	Multi-Angle Imager for Aerosol
MC	Monte Carlo
MERRA-2	Modern-Era Retrospective Analysis for Research and Application, Version 2
MODIS	Moderate Resolution Imaging Radiometer
NAP	Non-Algae Particles
NASEM	National Academies of Sciences, Engineering and Medicine
NIR	Near Infrared
OSS	Optimal Spectral Sampling
PACE	Plankton, Aerosol, Cloud, Ocean Ecosystem
PARASOL	Polarization & Anisotropy of Reflectances for Atmospheric Sciences Coupled with Observations from a Lidar
PCRTM	Principal Component Radiative Transfer Model
PGOM	Physical-Geometric Optics Method
POLDER	Polarization and Directionality of the Earth's Reflectances
RMSE	Root-Mean-Square Error
RTE	Radiative Transfer Equation

RTM	Radiative Transfer Model
SAA	Small-Angle Approximation
SOS	Successive Order of Scattering
SRF	Spectral Response Function
SVD	Singular Value Decomposition
SWIR	Shortwave Infrared
TIR	Thermal Infrared
TOA	Top of Atmosphere
UTC	Coordinated Universal Time
UV	Ultraviolet
VIIRS	Visible Infrared Imaging Radiometer Suite
VIS	Visible

TABLE OF CONTENTS

Page

LIST OF FIGURES

CHAPTER I

INTRODUCTION

1.1 Background

Radiative transfer is a process where electromagnetic radiation interacts with a medium by scattering, absorption, and emission. In the earth system, the atmosphere and terrestrial surface absorb and scatter incoming solar radiation. The absorbed radiation is eventually reemitted in the whole electromagnetic spectrum, particularly at meteorological temperature ranging from near infrared (NIR) to microwave bands. The radiative transfer process in the atmosphere and ocean is not only a flow of radiation, but also a flow of information about the earth system. The variations of radiance and polarization of the radiation contain useful information about atmospheric gases, clouds, aerosols, and the terrestrial surface including the ocean.

Spaceborne remote sensing instruments have provided decades of continuous observations of the earth system by measuring the outgoing radiation from the earth. The instruments are designed for different observation purposes with different observation capabilities. Passive instruments such as the Moderate Resolution Imaging Radiometer (MODIS) (King et al. 1992) and the Visible Infrared Imaging Radiometer Suite (VIIRS) (Cao et al. 2014) measure reflected solar radiation and thermal emission, whereas active instruments such as Cloud-Aerosol Lidar with Orthogonal Polarization (Winker et al. 2009) and Cloud Profiling Radar onboard CloudSat (Stephens et al. 2002) emit radiation to the earth and measure backscattered signals. Passive instruments usually have a larger field of view than active instruments so that they can obtain wider spatial coverage with each orbit. Active instruments can easily measure the vertical profile of the atmosphere with much better resolution than passive instrument.

Different instruments may conduct measurements in different spectral bands. For example, MODIS and VIIRS measure radiation ranging from visible (VIS) to thermal infrared (TIR) bands, in which radiation is sensitive to cloud and aerosol microphysical and optical properties. VIS to NIR bands are also used for ocean remote sensing because water and the atmosphere above it have relatively low absorption. The Advanced Microwave Scanning Radiometer for EOS (Kawanishi et al. 2003) measures microwave radiation, which is sensitive to precipitation and cloud water content. The instruments also have different spectral and spatial resolution. For example, in TIR bands, MODIS has 16 channels with moderate spectral resolution and spatial resolution less than 1 km, whereas Atmospheric Infrared Sounder (Aumann et al. 2003) has 2378 channels with hyperspectral resolution and with spatial resolution over 10 km. Compared to atmospheric gas concentration measurement, which requires high spectral resolution because gases have very narrow absorption lines, spatial resolution may be more demanding for cloud and aerosol remote sensing. Cloud and aerosol optical properties do not vary significantly in a typical spectral band, but they usually have large spatial variation.

1.2 Introduction to Polarimetric Remote Sensing

Although spaceborne observations have tremendously enriched our knowledge of variations in the earth system, and their responses to climate change, there are still substantial uncertainties in inferring global cloud, aerosol and ocean properties due to limited capabilities of remote sensing instruments and techniques. In addition to gradually improving instrument spatial and spectral resolutions, spaceborne and airborne passive polarimetric remote sensing has more recently become feasible (e.g. Mishchenko and Travis 1997; Parol et al. 2004; Dubovik et al. 2011; Chowdhary et al. 2012).

In particular, the Polarization and Directionality of the Earth's Reflectances (POLDER) (Deschamps et al. 1994) and Airborne Multiangle SpectroPolarimetric Imager (AirMSPI) (Diner et al. 2013) have been demonstrated to be effective in inferring cloud, aerosol and ocean properties. The polarimeters not only measure the radiance, but also measure the state of polarization of the radiation reflected and emitted by cloud, aerosol and oceans. Furthermore, for the same target, they conduct nearly simultaneous measurements in multiple angles. Specifically, POLDER and AirMSPI use VIS to NIR bands to observe reflected solar radiation. Recent studies (e.g. Gong and Wu 2017; Gong et al. 2018) show that spaceborne and airborne microwave/submillimeter polarimetric radiometers such as Global Precipitation Measurement Microwave Imager (Draper et al. 2015) and Compact Scanning Submillimeter-wave Imaging Radiometer (Evans et al. 2005) have considerable potential for measuring microphysical properties of ice cloud by observing thermal emission from the earth atmosphere.

The radiation of a beam of light at any location and with any wavelength can be completely expressed by the Stokes vector,

$$\mathbf{I} = \begin{pmatrix} I \\ Q \\ U \\ V \end{pmatrix}, \tag{1.1}$$

in which I, Q, U, and V are Stokes parameters with the units of irradiance or flux (W/m^2) (Wendisch and Yang 2012). I is the intensity of the beam. The Q, U, and V parameters are defined as (Chandrasekhar 1960)

$$Q = I\cos 2\beta \cos 2\chi\,, \tag{1.2a}$$

$$U = I\cos 2\beta \sin 2\chi\,, \tag{1.2b}$$

$$V = I\sin 2\beta\,, \tag{1.2c}$$

where all variables and terms are explained as follows.

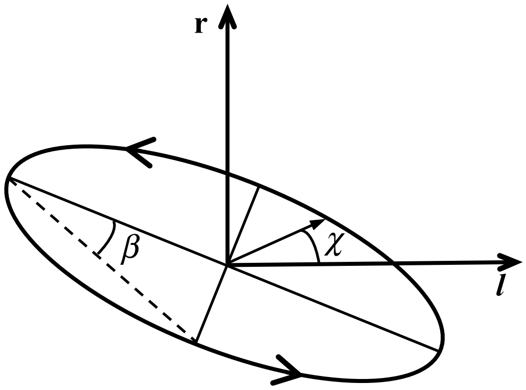

Figure 1 Polarization ellipse formed by the end point of the electric vector of the beam.

Fig. 1 shows the definitions of the angles χ ($0 \le \chi \le \pi$) and β ($-\pi/4 \le \beta \le \pi/4$), and other quantities to describe a beam with general polarization. In Fig. 1, the beam direction (**r**×***l***) is vertically into the paper. A reference plane is arbitrarily chosen along the propagation direction with direction ***l*** parallel to or in the reference plane and **r** perpendicular to the plane. Both **r** and ***l*** are perpendicular to the propagation direction of the beam. χ is the angle between ***l*** and the electric vector of the beam. β defines the ellipticity of the polarization ellipse and the rotation direction of elliptical polarization. Q is the linear polarization component in the **r** and ***l*** directions, U is the linear polarization component in directions 45° and 135° relative to the ***l*** direction, and V is the circular polarization component. Clockwise rotation by viewing toward the source of the beam is defined as right-handed polarization in this dissertation. The polarization ellipse in Fig. 1 represents right-handed polarization.

Because the choice of reference plane is arbitrary, the values of Q and U may be different for different reference planes. The Stokes vectors of the same beam but with two reference planes defined by **r** and ***l***, and **r**′ and ***l***′ are related by a rotation matrix,

$$\mathbf{I}' = \mathbf{L}\left(\alpha\right)\mathbf{I}, \tag{1.3}$$

in which **L** is the rotation matrix, and α is the angle between **r** and **r**′ or ***l*** and ***l***′. α is positive if **r** and ***l*** are rotated clockwise by an angle of α to **r**′ and ***l***′ when viewing toward the source of the beam. The rotation matrix is defined as (Hovenier et al. 2004)

$$\mathbf{L}\left(\alpha\right) = \begin{pmatrix} 1 & 0 & 0 & 0 \\ 0 & \cos 2\alpha & \sin 2\alpha & 0 \\ 0 & -\sin 2\alpha & \cos 2\alpha & 0 \\ 0 & 0 & 0 & 1 \end{pmatrix}. \tag{1.4}$$

Solar radiation and thermal emission are unpolarized, so their Stokes vectors are written as $\left(I, 0, 0, 0\right)$. The scattering properties of particles such as aerosols and phytoplankton can be expressed by a 4×4 Mueller matrix **M**,

$$\mathbf{M}=\begin{pmatrix} M_{11} & M_{12} & M_{13} & M_{14} \\ M_{21} & M_{22} & M_{23} & M_{24} \\ M_{31} & M_{32} & M_{33} & M_{34} \\ M_{41} & M_{42} & M_{43} & M_{44} \end{pmatrix}, \tag{1.5}$$

where M_{ij} (i,j=1, 2, 3, 4) are matrix elements. The particles scatter both incident solar radiation and thermal emission. The Stokes vector of scattered radiation is linearly related to the counterpart of incident radiation through **M**,

$$\mathbf{I}_{sca}=\frac{1}{k^2d^2}\mathbf{M}\mathbf{I}_{inc}\,, \tag{1.6}$$

where subscripts '*sca*' and '*inc*' represent scattering and incidence respectively. k is the wavenumber of the radiation. d is the distance between the particles and the location where $\mathbf{I}_{sca}$ is observed.

From Eqs. (1.5) and (1.6), the scattered radiation is polarized even though the incident radiation is unpolarized, because the Mueller matrix off-diagonal elements are nonzero except for in the 0 and 180° scattering angles. In the scattered Stokes vector, Eq. (1.6), the element I carries the information of M_{11}. Q, U, and V carry the information of all Mueller matrix elements. Eq. (1.6) only describes a single scattering process. In a cloud, aerosol or ocean layer, the incident radiation is always scattered multiple times. Compared with radiance-only measurement, polarization measurement contains more information of particle optical properties including scattering, absorption, and emission properties, from which we can infer more information about clouds, aerosols and oceans.

The spaceborne and airborne polarimeters measure I, Q, and U components of the Stokes vector. The reflectance, defined as

$$R = \frac{\pi I}{\mu_0 F_0}, \tag{1.7}$$

and polarized reflectance, defined as

$$R_{\mathrm{p}} = \frac{\pi \sqrt{Q^2 + U^2}}{\mu_0 F_0}, \tag{1.8}$$

are usually used to infer particle properties if the polarimeter receives reflected solar radiation. μ_0 is the cosine of the solar zenith angle. F_0 is the solar irradiance.

Because thermal emission from the atmosphere is independent of azimuth angle, only I and Q components are nonzero. The polarimetric instrument measures horizontal and vertical polarized intensities of thermal emission instead of I and Q components. The intensities I in the horizontal (H) and vertical (V) polarization directions are defined as

$$I_{\mathrm{H}} = \left(I + Q\right)/2, \tag{1.9a}$$

and

$$I_{\mathrm{V}} = \left(I - Q\right)/2. \tag{1.9b}$$

1.3 Motivation

Both theory and practice have proved the potential of polarimetric remote sensing. The consensus study report *Thriving on Our Changing Planet: A Decadal Startegy for Earth Observation from Space* from the National Academies of Sciences, Engineering and Medicine (NASEM 2018), considers the observations of aerosol and cloud properties and vertical profile with backscatter lidar and multi-channel and multi-angle polarimeter to be the highest priority for future development. Earth observation projects such as the

Plankton, Aerosol, Cloud, ocean Ecosystem (PACE) (PACE Technical Report Series 2018), the Multi-Angle Imager for Aerosol (MAIA) (Liu and Diner 2017), Aerosol/Cloud/Ecosystem mission (ACE) (da Silva et al. 2016) and the Multi-viewing -channel -polarisation Imager (3MI) (Marbach et al. 2015) will deploy such more advanced polarimeters. In addition to enhanced polarimetric capabilities, these future new remote sensing instruments will have higher spectral and spatial resolutions.

The tremendously enhanced data to be obtained from the future instruments will contain much more information about the atmosphere and oceans such as aerosol composition and phytoplankton characterization. Because of the large volume of remote sensing observational data, an efficient retrieval algorithm is needed while achieving accuracy comparable to in-situ measurements. Fig. 2 illustrates the schematic of a retrieval algorithm. The top row of Fig. 2 shows the observation process. A remote sensing instrument measures the radiation coming from the atmosphere and ocean through radiative transfer process. The bottom row of Fig. 2 shows the simulation process. A radiative transfer model (RTM) computes radiation by assuming model atmospheric and oceanic properties. The middle row of Fig. 2 shows the inversion process. The inversion algorithm interprets the observation based on the simulation to generate retrieval results such as cloud optical thickness and chlorophyll concentration.

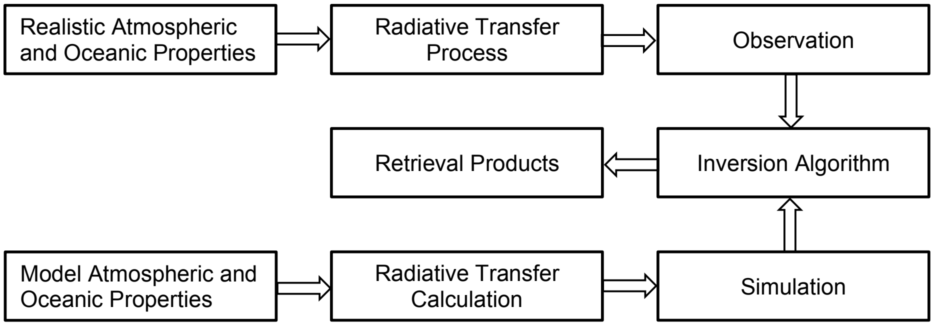

Figure 2 Schematic overview of radiative transfer calculations in retrieval algorithm.

To support polarimetric remote sensing, RTM should be able to compute the state of polarization of radiation. An RTM that outputs the Stokes vector of a radiation is named as vector RTM. Also, the RTM must be applicable in various spectral bands dealing with reflected solar radiation and thermal emission from the earth. The usages of RTM simulations are different in retrieval algorithms. In general, the roles an RTM plays in the retrieval algorithm can be classified as off-line and in-line simulators. An off-line simulator computes the radiative quantities under various atmospheric and oceanic conditions. The results are organized as a look-up table (LUT) to be used in retrieval implementation. Interpolation is always involved in using an LUT, which introduces interpolation error. An in-line simulator is a part of the retrieval algorithm. Radiative transfer calculation is implemented when the retrieval is ongoing. An in-line simulator can incorporate atmospheric and oceanic properties directly into the retrieval algorithm, so there is no interpolation error. Obviously, both off-line and in-line radiative transfer calculations must be accurate and have errors less than measurement uncertainties. The in-line simulator must also work as fast as other parts of the retrieval algorithm, which however is not required for an off-line simulator.

Over the years, tremendous efforts have been expended on developing in-line RTMs for remote sensing applications. Most fast hyperspectral RTMs (e.g. Strow et al. 2003; Liu et al. 2006; Moncet et al. 2008) are limited to clear-sky cases where only gas absorption and emission contribute to the top of atmosphere (TOA) radiation. Some fast hyperspectral RTMs (e.g. Han et al. 2006; Wang et al. 2015; Liu et al. 2016) and wideband RTMs (e.g. Liu et al. 2015) consider both gas absorption and multiple scattering in aerosol and cloud layers. However, these models do not consider polarization of radiation. Polarimetric remote sensing certainly needs an appropriate RTM to account for the polarization state of the radiation field. Without consideration of polarization, radiative transfer calculation has varying degrees of inaccuracy, depending on specific applications. For example, in a Rayleigh scattering atmosphere, neglecting polarization can result in errors up to 10% for radiance simulation (Kattawar et al. 1976; Lacis et al. 1998). The errors are much larger than the instrument calibration error and noise level. The errors have complex dependence on viewing geometry and optical thickness, so it is difficult to correct them (Lacis et al. 1998).

In this study, we develop a fast vector RTM for applications to atmospheric and oceanic remote sensing. The model efficiently simulates the full Stokes vector with various specified spectral resolutions by employing an improved gas absorption parameterization scheme and a flexible vector radiative transfer equation (RTE) solver. Efforts to infer aerosol, cloud, and oceanic properties with the PACE, MAIA, ACE and 3MI observations will benefit from this research. The RTM can also improve remote sensing techniques based on the existing POLDER, AirMSPI, MODIS and VIIRS instruments. Chapter II presents an overview of the developed model. Chapters III to VI describe the details of the model. Chapter VII show calculation results and comparisons with satellite observations. Chapter VIII summarizes the study.

CHAPTER II

AN OVERVIEW OF THE RTM

2.1 Model Layer Setup and Geometry

The developed vector RTM is capable of simulating the full Stokes vector with variable spectral resolution under various atmospheric and oceanic conditions. The vector RTM is based on a plane-parallel approximation, and is a one-dimensional model. The model atmosphere and ocean in the RTM is illustrated in Fig. 3. The atmosphere is composed of multiple homogeneous layers. Each layer composition includes gases, and possibly clouds, aerosols, or a mixture. The ocean layer of Case I water contains pure water, phytoplankton, non-algae particles (NAP) and Colored Dissolved Organic Matter (CDOM) (Chowdhary et al. 2006). There is an interface between the atmosphere and ocean. The transmission and reflection properties of the interface are related to the ocean surface condition. The absorption, scattering and emission by the atmosphere and ocean are considered in the calculation.

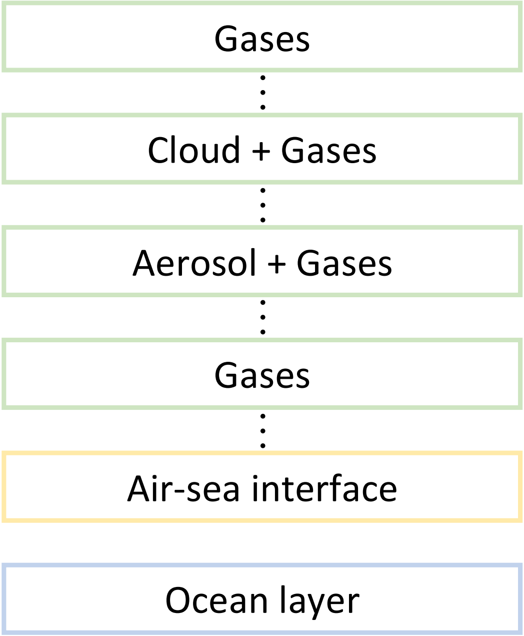

Figure 3 An illustration of the atmosphere and ocean layers in the RTM.

The vector RTE with the plane-parallel approximation is written as

$$\begin{aligned} u\frac{\partial \mathbf{I}(\tau,u,\varphi)}{\partial \tau} &= \mathbf{I}(\tau,u,\varphi) \\ &-\frac{\varpi(\tau)}{4\pi}\int_{-1}^{1} du'\int_{0}^{2\pi} d\varphi' \mathbf{P}(\tau,u,u',\varphi-\varphi')\mathbf{I}(\tau,u',\varphi')-\left[1-\varpi(\tau)\right]\mathbf{B}\left[T(\tau)\right], \end{aligned} \tag{2.1}$$

in which **I** is the Stokes vector, **P** is the phase matrix, **B** is the Planck function vector, ϖ is the single-scattering albedo, T is temperature, τ is optical thickness, u is the cosine of zenith angle, and φ is the azimuth angle. The wavelength dependences of **I**, **P**, **B**, τ and ϖ are implied but not shown in Eq. (2.1). **B** is $\begin{pmatrix} B\left[T(\tau)\right] & 0 & 0 & 0 \end{pmatrix}^{\mathrm{T}}$, in which B is the Planck function.

The zenith and azimuth angles involved in the RTM are shown in Fig. 4. Incident and outgoing zenith angles (θ' and θ), and incident and outgoing azimuth angles (φ' and

φ) describe the viewing geometry. The zenith angle is in the interval (0, π). The zenith angle is the angle between zenith and beam propagation directions. The azimuth angle is the angle between the *x*-axis and the horizontal projection of the beam propagation direction, which is measured clockwise when looking toward the zenith direction. The azimuth angle is in the interval (0, 2π). The relative azimuth angle $\Delta\varphi=\varphi-\varphi'$ is in the interval (0, π) due to symmetry with respect to $\Delta\varphi=\pi$. The absolute value of the cosine of the zenith angle $\mu=|u|$ is also used to describe polar directions, and μ and $-\mu$ specify upward and downward directions respectively. One exception is the solar zenith angle μ_0. Although the incident solar radiation is always downward in a plane-parallel atmosphere, μ_0 rather than $-\mu_0$ specifies its direction.

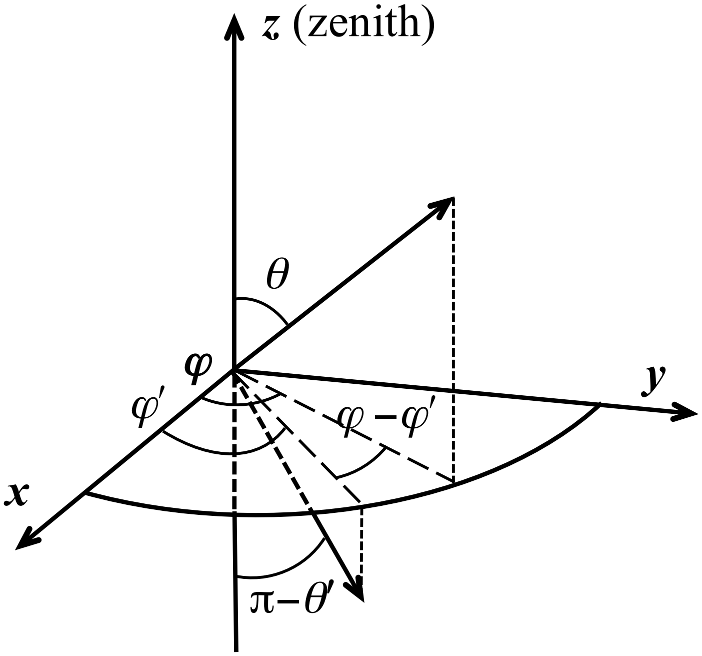

Figure 4 Illustrations of incident zenith angle (θ'), outgoing zenith angle (θ), incident azimuth angle (φ'), outgoing azimuth angle (φ), and relative azimuth angle ($\varphi-\varphi'$).

2.2 RTE with Solar and Thermal Emission Sources

The Stokes vector in Eq. (2.1) can be written as **I**=**I**$_s$+**I**$_t$. **I**$_s$ and **I**$_t$ are the solution components when solar radiation and thermal emission by the atmosphere and surface are sources. Because Eq. (2.1) is a linear integro-differential equation, it can be written as two decoupled equations,

$$\begin{aligned} u\frac{\partial \mathbf{I}_{\mathrm{s}}(\tau,u,\varphi)}{\partial \tau} &= \mathbf{I}_{\mathrm{s}}(\tau,u,\varphi) \\ &-\frac{\varpi(\tau)}{4\pi}\int_{-1}^{1}du'\int_{0}^{2\pi}d\varphi'\mathbf{P}(\tau,u,u',\varphi-\varphi')\mathbf{I}_{\mathrm{s}}(\tau,u',\varphi'), \end{aligned} \tag{2.2a}$$

$$\begin{aligned} u\frac{\partial \mathbf{I}_{\mathrm{t}}(\tau,u,\varphi)}{\partial \tau} &= \mathbf{I}_{\mathrm{t}}(\tau,u,\varphi) \\ &-\frac{\varpi(\tau)}{4\pi}\int_{-1}^{1}du'\int_{0}^{2\pi}d\varphi'\mathbf{P}(\tau,u,u',\varphi-\varphi')\mathbf{I}_{\mathrm{t}}(\tau,u',\varphi')-\left[1-\varpi(\tau)\right]\mathbf{B}\left[T(\tau)\right]. \end{aligned} \tag{2.2b}$$

Eqs. (2.2a) and (2.2b) can be solved separately so the sum of their solutions is the total Stoke vector of the radiation field. The boundary condition of **I**$_s$ in downward direction at the TOA (τ=0) is

$$\mathbf{I}_{\mathrm{s}}(0,-\mu,\varphi)=F_0\delta(\mu-\mu_0)\delta(\varphi-\varphi_0)\begin{pmatrix}1 & 0 & 0 & 0\end{pmatrix}^{\mathrm{T}}, \tag{2.3}$$

in which δ is the Delta function, and φ_0 is the solar azimuth angle. The incident solar radiation is assumed unpolarized. The boundary condition of **I**$_t$ in downward direction at the TOA is a zero vector. Eqs. (2.2a) and (2.2b) are solved separately in the model. In the ultraviolet (UV) to NIR band, the atmospheric thermal emission is very small and is ignored so the solution to Eq. (2.2b) is zero. Similarly, in the far infrared to microwave band, solar radiation can be ignored so the solution to Eq. (2.2a) is zero.

In a clear-sky atmosphere, if Rayleigh scattering is ignored and ϖ is equal to zero, the solutions to Eq. (2.2a) and (2.2b) in the upward direction at the TOA are

$$\mathbf{I}_{\mathrm{s}}\left(0,\mu,\varphi\right)=\frac{\mu_0 F_0}{\pi}e^{-\frac{b}{\mu_0}}\mathbf{R}_{\mathrm{surf}}\left(\mu_0,\varphi_0,\mu,\varphi\right)\begin{pmatrix} 1 & 0 & 0 & 0 \end{pmatrix}^{\mathrm{T}}e^{-\frac{b}{\mu}}, \tag{2.4a}$$

$$\mathbf{I}_{\mathrm{t}}\left(0,\mu,\varphi\right)=\varepsilon_{\mathrm{surf}}\mathbf{B}\left[T(b)\right]e^{-\frac{b}{\mu}}+\int_0^b\mathbf{B}\left[T(\tau)\right]e^{-\frac{\tau}{\mu}}\frac{d\tau}{\mu}, \tag{2.4b}$$

where b is the optical thickness from the TOA to the surface, $\mathbf{R}_{\mathrm{surf}}$ is the reflection matrix at the surface, and $\varepsilon_{\mathrm{surf}}$ is surface emissivity. The first term on the right-hand side of Eq. (2.4b) is thermal emission by the surface. The monochromatic transmittance is defined as

$$t(\tau,\mu)=e^{-\frac{\tau}{\mu}}. \tag{2.5}$$

Eq. (2.4) can be written as

$$\mathbf{I}_{\mathrm{s}}\left(0,\mu,\varphi\right)=\frac{\mu_0 F_0}{\pi}t(b,\mu_0)\mathbf{R}_{\mathrm{surf}}\left(\mu_0,\varphi_0,\mu,\varphi\right)\begin{pmatrix} 1 & 0 & 0 & 0 \end{pmatrix}^{\mathrm{T}}t(b,\mu), \tag{2.6a}$$

$$\mathbf{I}_{\mathrm{t}}\left(0,\mu,\varphi\right)=\varepsilon_{\mathrm{surf}}\mathbf{B}\left[T(b)\right]t(b,\mu)-\int_0^b\mathbf{B}\left[T(\tau)\right]\frac{dt(\tau,\mu)}{d\tau}d\tau. \tag{2.6b}$$

2.3 Introduction to Each Module in the RTM

The remote sensing instrument always receives the channel-averaged radiance defined as

$$\overline{I}=\int_{\nu_1}^{\nu_2}I(\nu)S(\nu)d\nu, \tag{2.7}$$

where $\overline{I}$ is the channel-averaged radiance, $I(\nu)$ is the radiance at wavenumber ν, and $S(\nu)$ is the normalized spectral response function (SRF) of the receiver at wavenumber ν.

The optical properties of cloud, aerosol and ocean vary slightly in the spectral range of a band with moderate and higher spectral resolution such as bands of MODIS and POLDER. However, the absorption by atmospheric gases varies considerably even in a narrow spectral range. If we use Eq. (2.7) to compute $\overline{I}$, though it is accurate, we have to do radiative transfer calculations in many wavelengths, which is computationally expensive and impractical for an in-line RTM.

Instead, we utilize channel-averaged radiative transfer calculation as an approximation to Eq. (2.7). The optical properties (i.e. absorption, scattering and emission) of the model atmosphere and ocean are averaged in the spectral range of a channel. Thus, only one radiative transfer calculation is needed to obtain approximate channel-averaged radiance $\overline{I}$. The channel-averaged optical property is defined as

$$\overline{X} = \int_{\nu_1}^{\nu_2} X(\nu) S(\nu) d\nu, \tag{2.8}$$

where X and $\overline{X}$ are an arbitrary optical property and its channel-averaged counterpart respectively.

2.3.1 Gas Absorption

Gas absorption is a critical process in radiative transfer. We consider channel-averaged transmittance (CAT) in the channel-averaged radiative transfer calculation, defined in a transmission path as

$$\overline{t} = \int_{\nu_1}^{\nu_2} S(\nu) \exp[-\tau_\nu(\nu)] d\nu, \tag{2.9}$$

in which τ_ν is the monochromatic optical thickness of gas absorption along the transmission path. The monochromatic transmittance in Eq. (2.6) should be replaced by

CAT. τ_ν is a function of wavelength as well as gas concentration, pressure and temperature. Eq. (2.9) can be implemented by a line-by-line (LBL) method (e.g. Clough et al. 2005) that is very time-consuming. Because of the complicated dependence of CAT on atmospheric profiles, we perform CAT computation as a part of the RTM. Thus, the LBL method is impractical due to the large computational burden.

Many research efforts have been devoted to efficient and accurate computation of CAT (also called spectral transmittance if the SRF is ignored). Band model methods (e.g. Goody 1952; Malkmus 1967) approximate spectral transmittance as analytical equations. The parameters in the equations are functions of pressure, temperature and gas concentration. For an inhomogeneous atmosphere, the band model methods use various scaling schemes (e.g. Curtis 1952; Godson 1953; Chou and Arking 1980; Fu and Liou 1992a) to scale the parameters to account for pressure, temperature and gas concentration variations in inhomogeneous atmospheric paths. Band model methods and their scaling approximations are accurate for flux and heating rate calculations (e.g. Fu and Liou 1992a; Bernstein et al. 1996).

Another spectral transmittance calculation approach is the correlated k-distribution (CKD) method (e.g. Lacis et al. 1979; Goody 1989; Fu and Liou 1992b). By sorting the absorption coefficients in a spectral range, the k-distribution method can efficiently compute spectral transmittance as accurately as the LBL method. If we assume the orders of absorption coefficients after sorting are the same for all atmospheric conditions, CKD can conveniently deal with an inhomogeneous atmosphere. The errors of CKD are from the correlation assumption. CKD has been successfully implemented (e.g. Edwards and

Francis 2000; Liu et al. 2015) to compute CAT for remote sensor channels. It can easily account for the SRF and solar constant, and be integrated into multiple scattering calculations (Liu et al. 2015).

Except for band model and CKD methods, many other approaches have been developed to compute CAT for remote sensor channels. For example, a Principal Component Radiative Transfer Model (Liu et al. 2006; Liu et al. 2016) is developed for hyperspectral instruments. The Optimal Spectral Sampling (OSS) method (Moncert 2008) selects a few monochromatic absorption coefficients to compute spectral transmittance. The Stand-Alone Radiative Transfer Algorithm (Strow et al. 2003), the Optical Path Transmittance algorithm (McMillin et al. 1995), and the Radiative Transfer TIROS Operational Vertical Sounder (Matricardi and Saunders 1999) are all regression-based methods. They construct regression equations between CAT values and atmospheric variables. The regression coefficients are obtained by fitting to LBL results.

Among the approaches mentioned above, the band model method does not precisely account for a detailed SRF and may not be accurate for remote sensing applications. The errors of the CKD method are hard to control under various atmospheric conditions. The PCRTM and OSS are complicated to implement. The regression-based methods have been proven accurate and efficient in many operational retrieval algorithms, and are relatively easy to implement. Thus, we develop a regression-based algorithm to compute CAT. The previous regression-based methods perform regression layer by layer. In our method, we only perform one regression for an inhomogeneous atmospheric path, which is more efficient especially for solar bands. The details will be discussed in Chapter III.

2.3.2 Multiple Scattering

Eqs. (2.2a) and (2.2b) have a multiple scattering term. An efficient vector RTE solver is needed to account for multiple scatterings in cloud, aerosol and ocean layers. The Successive Order of Scattering (SOS) method (e.g. Min and Duan 2004; Lenoble et al. 2007; Zhai et al. 2010), the Adding-Doubling (AD) method (e.g. de Haan et al. 1987; Evans and Stephens 1991; Hovenier et al. 2004), the Discrete Ordinate (DO) method (e.g. Siewert 2000; Rozanov and Kokhanovsky 2006; Ota et al. 2010) and the Monte Carlo (MC) method (e.g. Tynes et al. 2001; Iwabuchi 2006; Emde et al. 2011) are widely used in solving a vector RTE. In our model, the AD method based on the program developed by Huang et al. (2015) is used as the vector RTE solver, because it is numerically stable and easily accounts for multiple layers.

The phase matrices of atmospheric and oceanic particles are highly anisotropic. Especially in the forward direction, the diagonal elements of the phase matrix always have strong forward peaks. Thus, a number of terms are needed to represent the phase matrix accurately in terms of general spherical functions (GSF) (Wendish and Yang 2012), which will make radiative transfer calculations very time-consuming. To overcome this difficulty, many approaches are developed to truncate the forward peak in the phase function (e.g. Potter 1970; Wiscombe 1977; Hu et al. 2000) and the phase matrix (Zhai et al. 2009; Sanghavi and Stephens 2015; Hioki et al. 2016) so that fewer GSF terms are needed in radiative transfer calculations to attain decent accuracy. Some correction methods such as the TMS and IMS methods (Nakajima and Tanaka 1988) are also developed to correct the single-scattering errors caused by the truncation operation.

A previous study (Hioki et al. 2016) shows that the errors in reflection and polarized reflection calculation caused by the Delta-M truncation method (DMM) (Wiscombe 1977) can be substantially reduced by the TMS single-scattering correction method. However, in the forward direction, there are still large errors. Although for a solar source, remote sensing instrument only receives radiation in reflection directions, an accurate radiative transfer calculation in forward directions is still necessary, since it affects the simulation in reflection directions under certain conditions. For example, forward transmitted solar radiation reflecting off the sea surface leads to sun glint that is received by airborne or spaceborne instruments. The sun glint phenomenon has been utilized to measure sea surface characteristics (Cureton 2015) and proved to have rich information content about aerosol properties (Ottaviani et al. 2013) such as aerosol absorption (Kaufman et al. 2002). Coupled with polarimetric observation, sun glint is useful in detecting ocean surface oil slicks (Lu et al. 2017). Also, transmitted solar radiation through the air-sea interface accounts for as much as 30% of the polarization of water-leaving radiance (Kattawar and Adams 1989). Thus, a method is needed to keep both reflection and transmission accurate while significantly improving the speed of solving the vector RTE.

In this study, a two-component method is developed to solve the vector RTE. The highly anisotropic phase matrix of atmospheric and oceanic particles is decomposed into the forward and diffuse components. The forward component is nonzero only in a small range of angles. The diffuse component is much more isotropic. Similarly, the Stokes vector of the RTE solution is also decomposed into forward and diffuse components. After some approximations, we obtain decoupled forward and diffuse RTEs. The forward RTE is solved by the small-angle approximation (SAA) method (Sun et al. 2017a). The diffuse RTE is solved by the AD method (Huang et al. 2015). The AD computation is substantially accelerated due to the fact that the diffuse phase matrix can be expanded with a much lower order of the GSF. The derivations and detailed descriptions are given in Chapter IV.

2.3.3 Thermal Emission

In Eq. (2.2b), the thermal emission comes from the atmosphere and the surface. In a clear-sky condition, Eq. (2.2b) can be solved if we know the CAT and temperature of each layer. If scattering layers are present, thermal emission experiences multiple scattering. Previous studies (e.g. Wiscombe 1976; Heidinger et al. 2006; Liu and Weng 2006) discuss the thermal emission multiple scattering calculation in the AD method. However, none of them consider the state of polarization. In this study, we develop an efficient thermal emission calculation approach incorporated into the AD method. The approach is illustrated in Chapter V.

2.3.4 Air-Sea Interface and Ocean Model

The radiative transfer processes in the atmosphere and oceans are coupled through the air-sea interface. The vector RTE is solved under the atmosphere-ocean system (AOS). The SOS method is one of the most popular vector RTE solver of an AOS (e.g. Zhai et al. 2010, 2017; Chami et al. 2015). Other AOS vector RTE solvers include the MC method (e.g. Kattawar and Adams 1989), the matrix-operator method (e.g. He et al. 2010), the DO method (e.g. Spurr 2006) and the AD method (e.g. Chowdhary et al. 2006). In this study, we extend the AD vector RTE solver by Huang et al. (2015) to an AOS.

The air-sea interface is assumed to be a rough surface in the model to mimic the realistic ocean surface. There are two schemes for generating the rough surface. The first scheme approximates the rough surface as a number of hypothetical small facets. The orientations of the facets follow a 2-dimensional Gaussian distribution whose variance is determined by wind speed (Cox and Munk 1954). The second scheme expresses the surface wave height variation with a superposition of temporal- and spatial-dependent plane waves (e.g. Schwenger and Repasi 2003). The magnitude and phase of the plane waves are functions of wind speed and direction. The second scheme is much more computationally expensive so we adopt the first scheme to compute the interface reflection and transmission matrices in the RTM.

Pure water, phytoplankton, NAP and CDOM are included in the model of ocean inherent optical property (IOP) computation. Currently, only one homogeneous ocean layer is considered in the model. The details are described in Chapter VI.

The computational setup of the RTM is shown in Fig. 5. Atmospheric gas absorption is computed in terms of CAT. Properties of the atmosphere, ocean, and the interface are then input into the vector RTE solver, which outputs Stokes parameters in different locations.

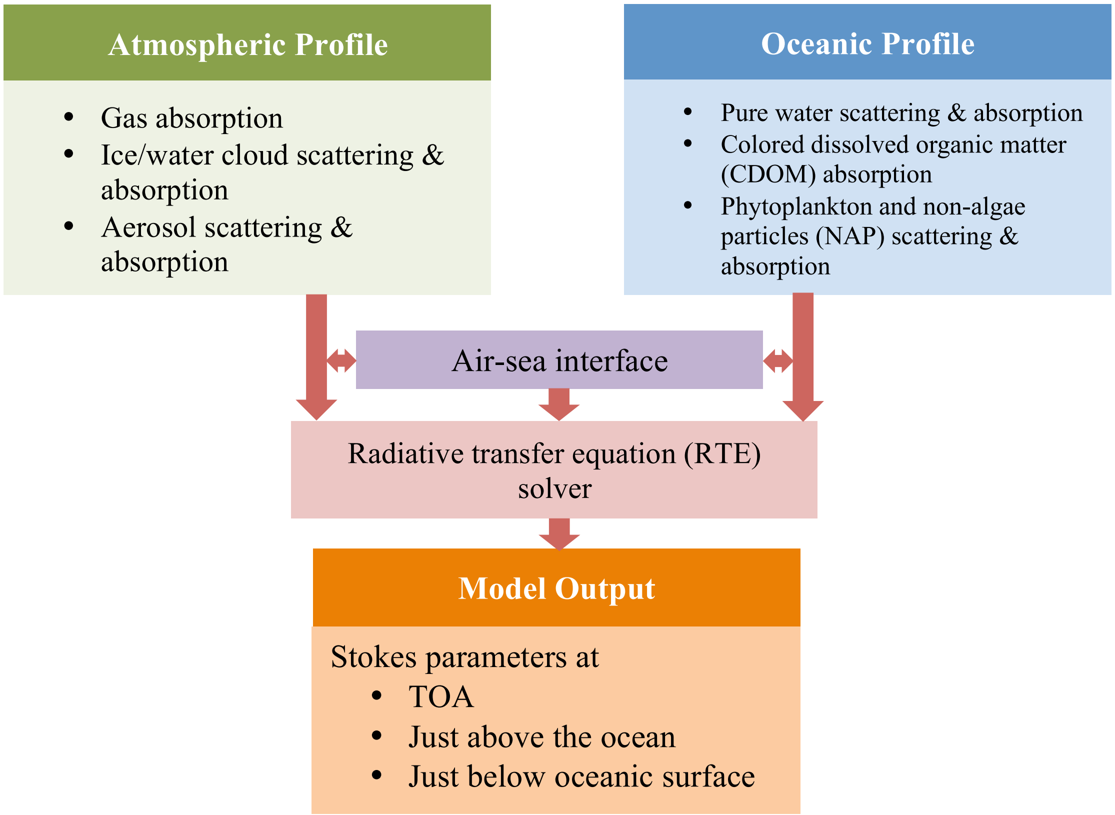

Figure 5 Computational setup of the RTM.

CHAPTER III

GAS ABSORPTION CALCULATION

3.1 Channel-averaged Transmittance and Optical Thickness

As illustrated in Chapter II, CAT is needed for channel-averaged radiative transfer calculation if the atmospheric gases are absorptive. Replacing the monochromatic transmittance in Eq. (2.4b) with the corresponding CAT, Eq. (2.4b) can be written in the discrete form,

$$\mathbf{I}_{\mathrm{t}}\left(0,\mu,\varphi\right)=\varepsilon_{\mathrm{surf}}\mathbf{B}(T_{\mathrm{surf}})\overline{t}_{l_s\sim 1}(\mu)+\sum_{l=1}^{l_s}\mathbf{B}(T_l)\left[\overline{t}_{(l-1)\sim 1}(\mu)-\overline{t}_{l\sim 1}(\mu)\right], \tag{3.1}$$

in which T_{surf} is surface temperature, l_{s} is the number of layers from the surface to TOA, where l_{s} is smaller or equal to the number of layers in the model L. The first layer is at the TOA. The last layer is the bottommost layer. $\overline{t}_{l\sim 1}$ is the CAT from the layer l to the layer 1. The model has 100 pressure layers corresponding to 101 pressure levels ranging from 0.05 hPa to 1100 hPa to be consistent with the pressure layer setup in Strow et al. (2003). In a clear-sky atmosphere, as indicated in Eq. (3.1), the layer-to-TOA CATs are needed in the channel-averaged RT calculation for a thermal emission source. Similarly, for a solar incidence source, as indicated in Eq. (2.4a), the surface-to-TOA CAT is needed. If there are scattering layers, we also need CATs among scattering layers, the surface and TOA as well as CATs within the scattering layers. Therefore, the gas absorption calculation module should be able to compute layer-to-layer CATs between two arbitrary layers in the model in order to account for all the atmospheric conditions.

The layer-to-layer CAT is defined as

$$\overline{t}_{i\sim j} = \sum_{m=1}^{M} S_m \exp\left[-a \sum_{l=i}^{j} \tau_m^l \right], \tag{3.2}$$

in which $\overline{t}_{i\sim j}$ is the CAT from layer i to layer j. M is the number of absorption coefficients considered in the spectral range. S_m is the discretized SRF at the m-th wavenumber in the spectral range. τ_m^l is the monochromatic optical thickness in the layer l at the m-th wavenumber. a is the secant of the zenith angle ($1/\mu$). $\overline{t}_{i\sim j}$ is a function of gas concentration, temperature, pressure and a. We develop a regression approach to parameterize the layer-to-layer CAT with atmospheric variables (e.g. pressure, temperature and gas concentrations). It is shown in Eq. (3.2) that $\overline{t}_{i\sim j}$ exponentially depends on monochromatic optical thickness, but the optical thickness is linearly proportional to gas concentration, for which it is difficult to directly parameterize CAT with respect to atmospheric variables. Alternatively, we define the layer-to-layer channel-averaged optical thickness (CAOT) as

$$\overline{\tau}_{i\sim j} \equiv -\ln \overline{t}_{i\sim j}, \tag{3.3}$$

which is parameterized with respect to atmospheric variables.

Eight gases are considered in the absorption calculation, namely, water vapor (H_2O), carbon dioxide (CO_2), ozone (O_3), nitrous oxide (N_2O), carbon monoxide (CO), methane (CH_4), oxygen (O_2), and nitrogen (N_2). Three kinds of absorption are considered: line absorption by H_2O, CO_2, O_3, N_2O, CO, CH_4, and O_2, continuum absorption by H_2O, CO_2, O_2 and N_2, and O_3 UV absorption. If more than one gas is an absorber in a channel, the CAOTs of all the gases are parameterized and computed separately, and then combined to obtain total CAOT. Note that the total CAOT is not equal to the sum of CAOTs of each gas, since Beer's law is invalid for CAT. To keep the total CAOT correct, we define the CAOT of each gas as

$$\begin{aligned} &\overline{\tau}_{i\sim j,1} \equiv \overline{\tau}_{i\sim j,1\sim N} - \overline{\tau}_{i\sim j,2\sim N}, \\ &\overline{\tau}_{i\sim j,2} \equiv \overline{\tau}_{i\sim j,2\sim N} - \overline{\tau}_{i\sim j,3\sim N}, \\ &\ldots, \\ &\overline{\tau}_{i\sim j,N-1} \equiv \overline{\tau}_{i\sim j,N-1\sim N} - \overline{\tau}_{i\sim j,N}. \end{aligned} \quad , \tag{3.4}$$

in which N is the number of absorptive gases in the channel. The second subscript in each CAOT is the index of the gas in the CAOT calculation. For example, $\overline{\tau}_{i\sim j,1\sim N}$ is the CAOT for gases 1, 2, … N, while $\overline{\tau}_{i\sim j,N}$ is the CAOT of the single gas N. The CAOTs on the right-hand side of Eq. (3.4) are computed by the Line-by-line Radiative Transfer Model (LBLRTM) (Clough et al. 2005). The total CAOT is

$$\overline{\tau}_{i\sim j,tot} \equiv \overline{\tau}_{i\sim j,1\sim N} = \sum_{n=1}^{N} \overline{\tau}_{i\sim j,n} \,. \tag{3.5}$$

3.2 Regression Method

The next step is to find a relation between $\overline{\tau}_{i\sim j,n}$ and the atmospheric variables, and use a polynomial regression approach to quantify this relation. To make regression numerically stable, we define the relative CAOT of a single gas n as,

$$\overline{\tau}_{r,i\sim j,n} \equiv \frac{\overline{\tau}_{i\sim j,n}}{\overline{\tau}_{ref,i\sim j,n}}, \tag{3.6}$$

in which $\overline{\tau}_{ref,i\sim j,n}$ is the reference CAOT of single gas *n* computed under the U.S. standard atmospheric profile. $\overline{\tau}_{r,i\sim j,n}$ is a function of atmospheric temperature, pressure, and gas concentrations in layers *i* to *j*,

$$\overline{\tau}_{r,i\sim j,n} = \overline{\tau}_{r,i\sim j,n}\left(T_i, T_{i+1}, \cdots, T_j \mid P_i, P_{i+1}, \cdots, P_j \mid u_{i,n}, u_{i+1,n}, \cdots, u_{j,n}\right), \tag{3.7}$$

in which T_i is the temperature of layer *i*, P_i the pressure of layer *i*, and $u_{i,n}$ the concentration of gas *n* in layer *i*.

After numerous tests, we construct a polynomial equation to parameterize $\overline{\tau}_{r,i\sim j,n}$,

$$\overline{\tau}_{r,i\sim j,n} = \sum_{k=1}^{K}\sum_{h=0}^{H} c_{kh}\left(\mathrm{G}_{i\sim j,n}^{\gamma}\right)^{k}\left(\mathrm{T}_{i\sim j}\right)^{h}, \tag{3.8}$$

in which $\mathrm{G}_{i\sim j,n}$ is the gas *n* concentration predictor. The exponent γ ranges from 0 to 1. $\mathrm{T}_{i\sim j}$ is the temperature predictor. c_{kh} is a polynomial coefficient. *K* can be 1, 2, 3, or 4; *H* can be 0, 1, 2 or 3. *K* and *H* are determined to satisfy accuracy and computation speed requirements.

$\mathrm{T}_{i\sim j}$ is defined as

$$\mathrm{T}_{i\sim j} = \left(\sum_{l=i}^{j} T_l P_l\right) \Bigg/ \left(\sum_{l=i}^{j} T_{ref,l} P_l\right), \tag{3.9}$$

where $T_{ref,\,i}$ is the layer *i* temperature in the reference atmospheric profile. Eq. (3.9) suggests that $\mathrm{T}_{i\sim j}$ is the sum of pressure-weighted temperature divided by its counterpart for a reference atmospheric profile.

$\mathrm{G}_{i\sim j,n}$ has nine different forms,

unweighted gas concentration:

$$\mathrm{G}^{0}_{i\sim j,n} = \left(\sum_{l=i}^{j} u_{l,n}\right) \Big/ \left(\sum_{l=i}^{j} u_{ref,l,n}\right), \tag{3.10a}$$

pressure-weighted gas concentration:

$$\mathrm{G}^{P}_{i\sim j,n} = \left(\sum_{l=i}^{j} u_{l,n} P_l\right) \Big/ \left(\sum_{l=i}^{j} u_{ref,l,n} P_l\right), \tag{3.10b}$$

temperature-weighed gas concentration:

$$\mathrm{G}^{T}_{i\sim j,n} = \left(\sum_{l=i}^{j} u_{l,n} T_l\right) \Big/ \left(\sum_{l=i}^{j} u_{ref,l,n} T_{ref,l}\right), \tag{3.10c}$$

pressure difference-weighted gas concentration:

$$\mathrm{G}^{\Delta P}_{i\sim j,n} = \left(\sum_{l=i}^{j} u_{l,n} \Delta P_l\right) \Big/ \left(\sum_{l=i}^{j} u_{ref,l,n} \Delta P_l\right), \tag{3.10d}$$

temperature and pressure difference-weighted gas concentration:

$$\mathrm{G}^{T\Delta P}_{i\sim j,n} = \left(\sum_{l=i}^{j} u_{l,n} T_l \Delta P_l\right) \Big/ \left(\sum_{l=i}^{j} u_{ref,l,n} T_{ref,l} \Delta P_l\right), \tag{3.10e}$$

temperature and pressure-weighted gas concentration:

$$\mathrm{G}^{TP}_{i\sim j,n} = \left(\sum_{l=i}^{j} u_{l,n} T_l P_l\right) \Big/ \left(\sum_{l=i}^{j} u_{ref,l,n} T_{ref,l} P_l\right), \tag{3.10f}$$

pressure and pressure difference-weighted gas concentration:

$$\mathrm{G}^{P\Delta P}_{i\sim j,n} = \left(\sum_{l=i}^{j} u_{l,n} P_l \Delta P_l\right) \Big/ \left(\sum_{l=i}^{j} u_{ref,l,n} P_l \Delta P_l\right), \tag{3.10g}$$

squared pressure-weighted gas concentration:

$$\mathrm{G}^{P^2}_{i\sim j,n} = \left(\sum_{l=i}^{j} u_{l,n} P_l^2\right) \Big/ \left(\sum_{l=i}^{j} u_{ref,l,n} P_l^2\right), \tag{3.10h}$$

and square root pressure-weighted gas concentration:

$$\mathrm{G}_{i\sim j,n}^{\sqrt{P}} = \left(\sum_{l=i}^{j} u_{l,n}\sqrt{P_l}\right) \Bigg/ \left(\sum_{l=i}^{j} u_{ref,l,n}\sqrt{P_l}\right), \tag{3.10i}$$

in which ΔP_l is the pressure difference between the top and bottom of a layer.

We compute $\mathrm{G}_{i\sim j,n}$ and $\overline{\tau}_{r,i\sim j,n}$ for various spectral bands with an atmospheric profile dataset used in Strow et al. (2003). The profiles cover varied atmospheric conditions on the earth. Fig. 6 shows the $\mathrm{G}_{i\sim j,n}\sim\overline{\tau}_{r,i\sim j,n}$ relations for H_2O and O_3 in MODIS band 17 and 30 respectively. The SRFs of MODIS bands are obtained from the website (https://mcst.gsfc.nasa.gov/calibration/parameters). For H_2O at band 17, the pressure-weighted gas concentration has the smoothest relation with $\overline{\tau}_{r,i\sim j,n}$, whereas for O_3 at band 30, the square root pressure-weighted gas concentration has the smoothest $\mathrm{G}_{i\sim j,n}\sim\overline{\tau}_{r,i\sim j,n}$ relation. If the $\mathrm{G}_{i\sim j,n}\sim\overline{\tau}_{r,i\sim j,n}$ relation is smooth, the polynomial parameterization should be accurate. The form of $\mathrm{G}_{i\sim j,n}$ that has the smallest polynomial fitting error is selected for each specific gas in a band.

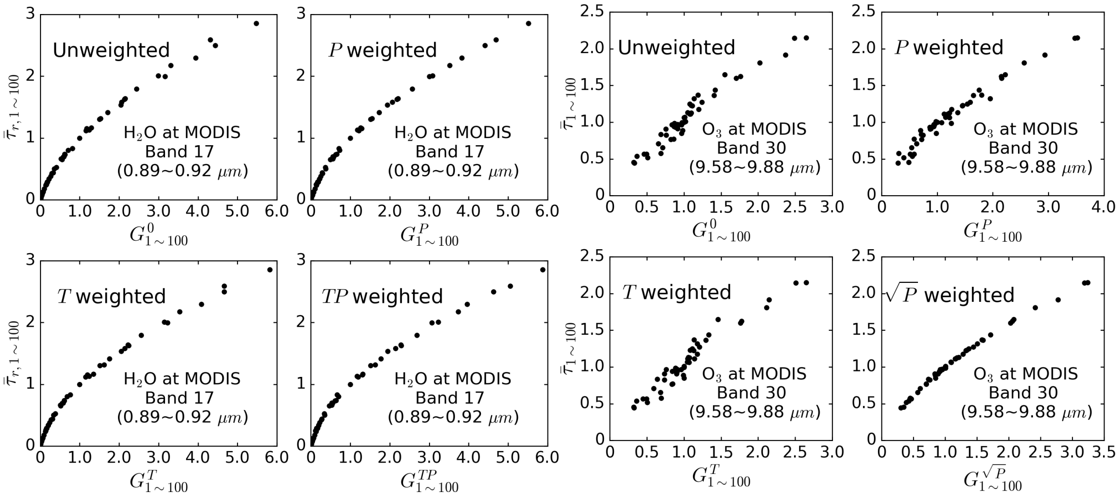

Figure 6 Relative CAOT of H_2O and O_3 in all model pressure layers versus various gas concentration predictors in two MODIS bands. **Left:** MODIS band 17; **Right:** MODIS band 30.

As examples, we select the forms of $G_{i\sim j,n}$ by a trial-and-error approach for all 36 MODIS bands and assumptive hyperspectral channels in UV to shortwave infrared (SWIR) bands (0.3 to 2.4 μm wavelength range). The spacing between two hyperspectral channels is 5 nm, which is consistent with the Ocean Color Imager in PACE project (PACE Technical Report Series 2018). The channel width is set to be 1/1200 of its central wavenumber. The SRF for the hyperspectral channels is assumed to be a rectangular window. Figs. 7 and 8 show the $G_{i\sim j,n}$ forms of H_2O, O_3 and CO_2 for MODIS bands and hyperspectral channels in 0.3 to 2.4 μm. All of the 9 forms in Eq. (3.10) are selected for MODIS bands. For the hyperspectral channels, only the first 3 forms are used. The variation of the selected $G_{i\sim j,n}$ for different gases and channels suggests the complexity of gas absorption properties. The various formulas in Eq. (3.10) are analogous to various scaling approximations for an inhomogeneous atmosphere.

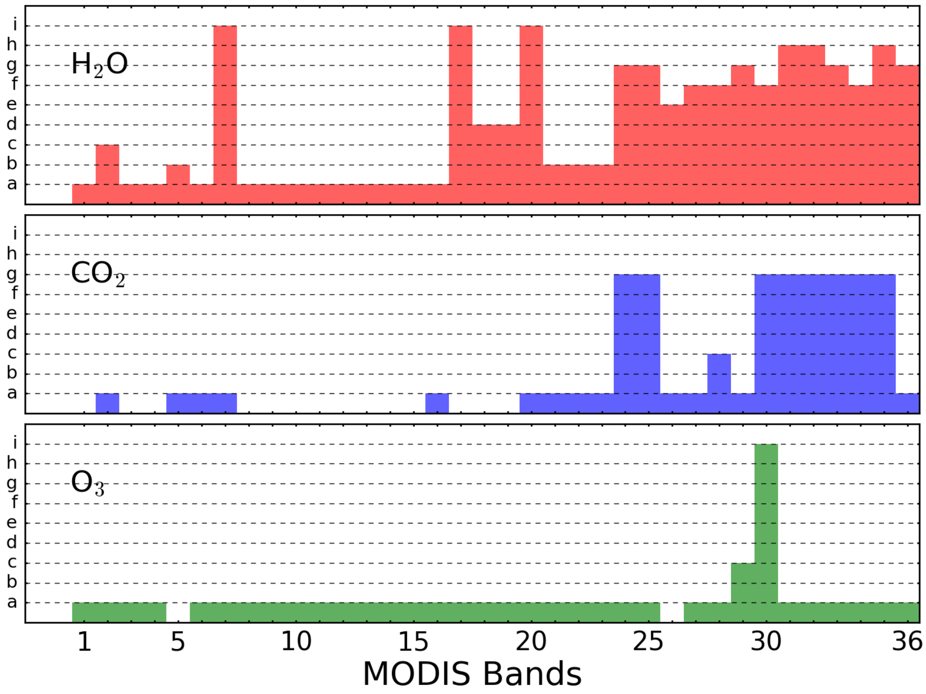

Figure 7 Gas concentration predictor forms of H_2O, CO_2 and O_3 for 36 MODIS bands. The letters in the y-axis correspond to the formulas in Eq. (3.10). If the gas in a band is not absorptive, no predictor form is derived.

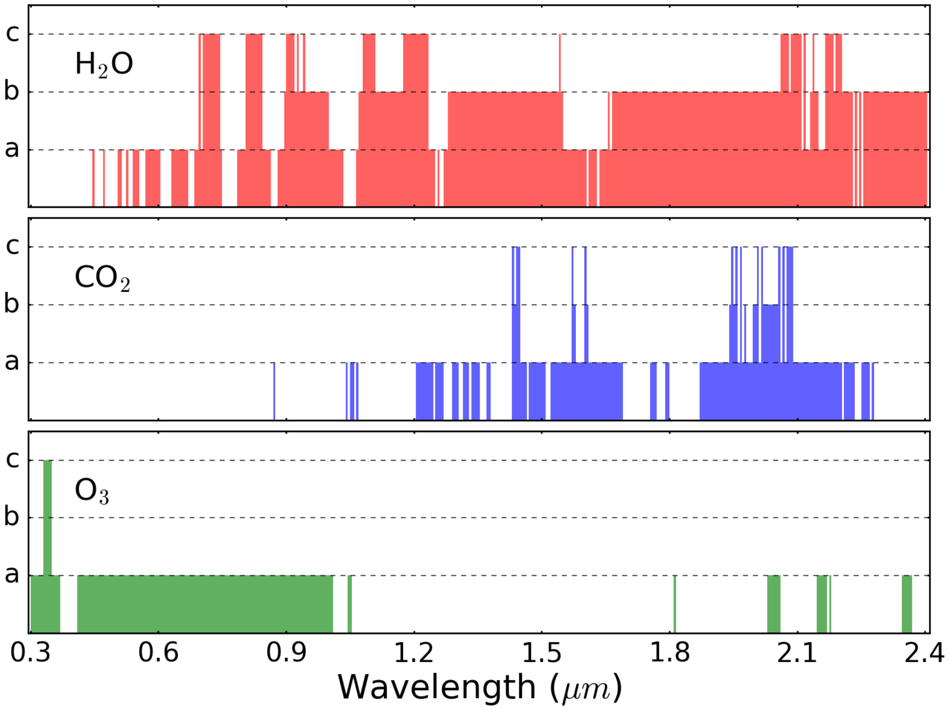

Figure 8 Gas concentration predictor forms of H_2O, CO_2 and O_3 for hyperspectral channels in the 0.3 to 2.4 μm wavelength range. The letters in the y-axis correspond to the formulas in Eq. (3.10). If the gas in a channel is not absorptive, no predictor form is derived.

The exponent γ in Eq. (3.8) is also determined by a trial-and-error approach to obtain the smallest fitting error. Figs. 9 and 10 show the γ values for H_2O, CO_2 and O_3 in different channels. The variation of γ is due to different relations between CAOT and gas concentration. The spectral transmittance in Goody's statistical band model (Goody 1952) can be written as

$$\bar{t} = \exp\left[-\frac{uA_m\alpha}{\Delta\upsilon\sqrt{\alpha^2 + \frac{uA_m\alpha}{\pi}}} \right], \tag{3.11}$$

where $\Delta\upsilon$ is the mean absorption line spacing, α the absorption line width, and A_m the mean absorption line intensity. From the definition of CAOT in Eq. (3.3) and Eq. (3.11), the CAOT is proportional to u^γ in the statistical band model. Because A_m and α are not constant, γ varies in the band model. Although the Goody's statistical band model is an approximation, it shows the reasonableness of including the exponent γ in the gas concentration predictors.

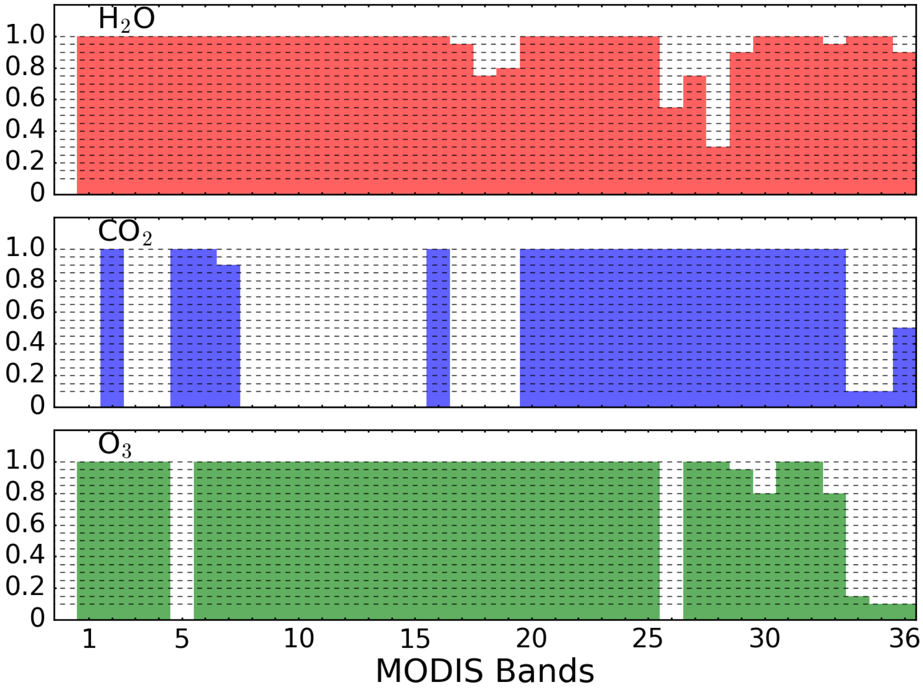

Figure 9 The exponent γ in Eq. (3.8) for H_2O, CO_2 and O_3 for 36 MODIS bands. If the gas in a band is not absorptive, no exponent γ is computed.

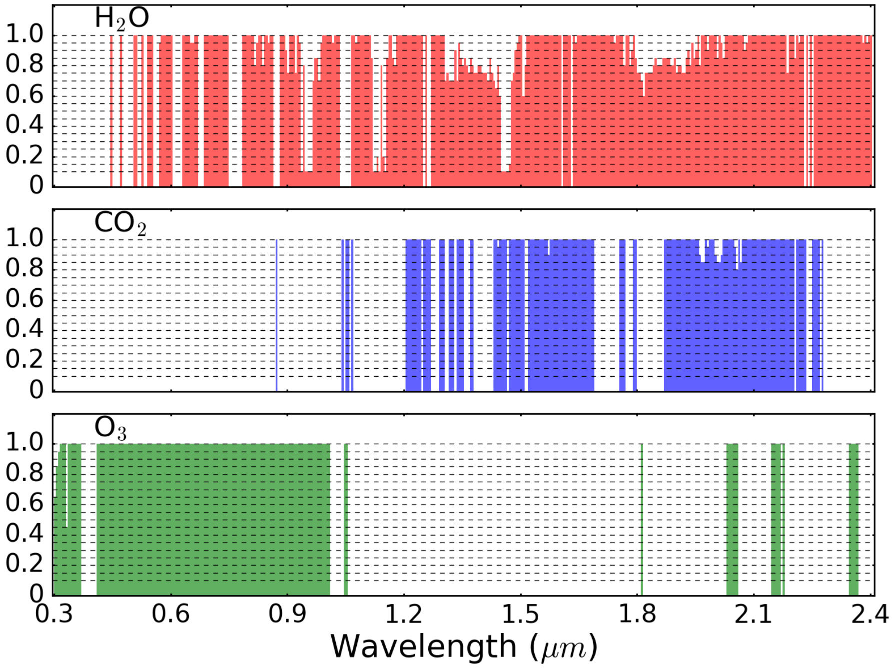

Figure 10 The exponent γ in Eq. (3.8) for H_2O, CO_2 and O_3 for hyperspectral channels in the 0.3 to 2.4 μm wavelength range. If the gas in a channel is not absorptive, no exponent γ is computed.

Many channels have more than one absorptive gas as shown in Figs. 7 to 10. According to Eq. (3.4), except for gas *N*, the CAOT of an absorptive gas depends on the CAOTs of other gases with larger indices. For example, $\overline{\tau}_{i\sim j,1}$ is dependent on the CAOTs of gases 2~*N*. To simplify the parameterization of CAOT, the CAOT interdependence is ignored in the channels where one gas is much more absorptive than others. The most strongly absorptive gas is assigned to be gas *N*. Its CAOT is computed by Eq. (3.2). In most of the channels in the UV-IR band, only one gas dominates absorption. There are a few channels in the IR band where CO_2 and other gases dominate absorption. Because the CO_2 concentration variation is small, we choose CO_2 as gas *N* in these channels. The CAOT of other gases is affected by the CO_2 concentration. We thus add an extra CO_2 predictor term in Eq. (3.8),

$$\overline{\tau}_{r,i\sim j,n}=\sum_{k=1}^{K}\sum_{h=0}^{H}c_{kh}\left(\mathrm{G}_{i\sim j,n}^{\gamma}\right)^{k}\left(\mathrm{T}_{i\sim j}\right)^{h}+\mathrm{G}_{i\sim j,\mathrm{CO}_2}\sum_{h=0}^{H}c_{h,\mathrm{CO}_2}\left(\mathrm{T}_{i\sim j}\right)^{h}, \tag{3.12}$$

in which $\mathrm{G}_{i\sim j,\mathrm{CO}_2}$ is the predictor for CO_2.

If the polynomial coefficients in Eqs. (3.8) or (3.12) are known for a channel, for a specific atmospheric profile, we can first compute predictors $\mathrm{G}_{i\sim j,n}$, and then use Eqs. (3.8) or (3.12) to compute CAOTs of the atmosphere for the channel. The polynomial coefficients are determined by a regression approach. The regression can be described by a matrix equation,

$$\mathbf{GC}=\mathbf{O}, \tag{3.13}$$

in which **G** is the predictor matrix, **C** the regression coefficient vector and **O** the relative CAOT vector. **G** is

$$\mathbf{G}=\begin{bmatrix} \left\langle\left(G_{i\sim j,n}^{\gamma}\right)^{K}\left(\mathrm{T}_{i\sim j}\right)^{H}\right\rangle_{1} & \cdots & \left\langle G_{i\sim j,n}^{\gamma}\mathrm{T}_{i\sim j}\right\rangle_{1} & \left\langle G_{i\sim j,n}^{\gamma}\right\rangle_{1} \\ \vdots & \vdots & \vdots & \vdots \\ \left\langle\left(G_{i\sim j,n}^{\gamma}\right)^{K}\left(\mathrm{T}_{i\sim j}\right)^{H}\right\rangle_{M} & \cdots & \left\langle G_{i\sim j,n}^{\gamma}\mathrm{T}_{i\sim j}\right\rangle_{M} & \left\langle G_{i\sim j,n}^{\gamma}\right\rangle_{M} \end{bmatrix}, \tag{3.14}$$

in which M here is the number of atmospheric profiles used in the regression calculation. **G** has dimension $M \times K(H+1)$ for Eq. (3.8), and $M \times (K+1)(H+1)$ for Eq. (3.12). **C** is

$$\mathbf{C}=\begin{bmatrix} c_{KH} & \cdots & c_{10} \end{bmatrix}^{\mathrm{T}}. \tag{3.15}$$

O is

$$\mathbf{O}=\begin{bmatrix} \left\langle\overline{\tau}_{r,i\sim j,n}\right\rangle_{1} & \cdots & \left\langle\overline{\tau}_{r,i\sim j,n}\right\rangle_{M} \end{bmatrix}^{\mathrm{T}}. \tag{3.16}$$

The regression coefficient vector Eq. (3.15) can be computed by

$$\mathbf{C}=\left(\mathbf{G}^{\mathrm{T}}\mathbf{G}\right)^{-1}\mathbf{G}^{\mathrm{T}}\mathbf{O}, \tag{3.17}$$

which, however, is not numerically stable. An alternative approach to solve Eq. (3.13) is to use singular value decomposition (SVD) to first decompose **G**,

$$\mathbf{G}=\mathbf{V}_1\boldsymbol{\Sigma}\mathbf{V}_2^{\mathrm{T}}, \tag{3.18}$$

in which $\mathbf{V}_1$ and $\mathbf{V}_2$ are orthogonal matrices, and $\boldsymbol{\Sigma}$ is a diagonal matrix. Substituting Eq. (3.18) into Eq. (3.17), the regression coefficient vector is obtained by

$$\mathbf{C}=\mathbf{V}_1^{\mathrm{T}}\boldsymbol{\Sigma}^{-1}\mathbf{V}_2\mathbf{O}. \tag{3.19}$$

For one atmospheric profile, radiative transfer calculations are usually implemented in multiple viewing geometries, so CATs are needed in different zenith angles. The secant of zenith angle *a* is a variable in Eq. (3.2), but *a* can be a regression variable, which however, makes regression inaccurate according to our tests. Instead, *a* is set to be a constant in regression. The regressions are performed with 7 secants of zenith angles (1, 1.1, 1.5, 2.0, 3.0, 5.0, and 10.0) respectively, which correspond to zenith angles from 0 to over 84°, and cover the applicable solar and viewing zenith angle ranges in remote sensing. To compute the total CAOT at an arbitrary zenith angle, first, the CAOTs of all absorptive gases are computed at the two *a* values above and below the desired *a* value. Then, the total CAOT at the desired zenith angle is obtained by linear or spline interpolations. As shown in Fig. 11, the total CAOT is a smooth function with respect to *a*, though it is not linear. Interpolation does not reduce accuracy a lot.

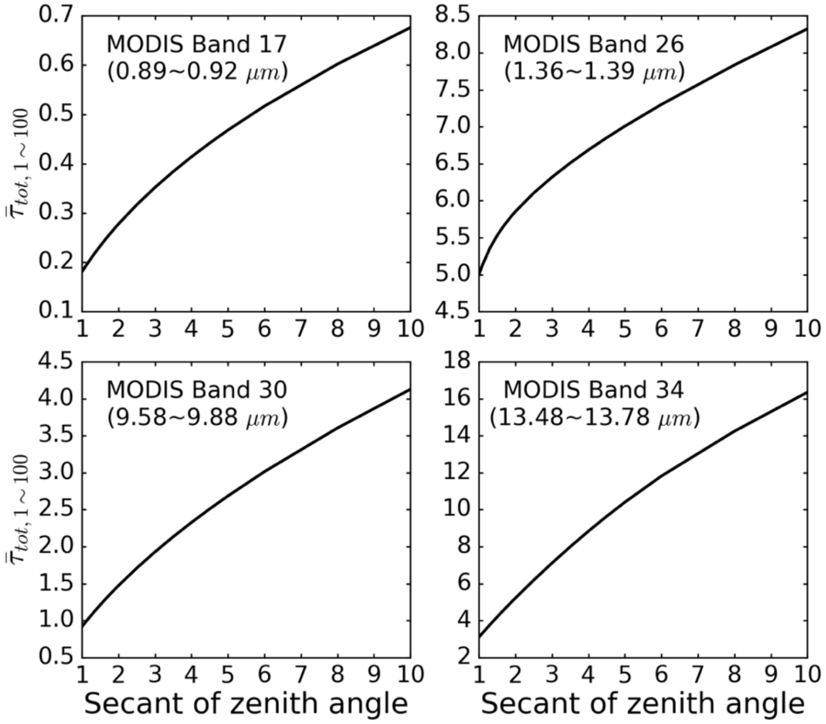

Figure 11 Total CAOTs in MODIS bands 17, 26, 30 and 34 in all pressure layers of the model versus the secant of zenith angle.

3.3 Validation

The regression calculations are performed for all MODIS bands and the hyperspectral channels mentioned above. The regression coefficients are used to compute CAOTs for independent atmospheric profiles. Two illustrative examples are shown in Figs. 12 and 13.

Fig. 12 shows the hyperspectral CAT with 5 nm resolution computed by the regression method and the line-by-line method. The independent atmospheric profiles are from the Borbas et al. (2005) training database of global profiles. We obtain the temperature profile, H_2O mixing ratio, O_3 mixing ratio, surface pressure, and surface temperature of each atmospheric profile from the database. Global mean mixing ratios for other gases are used in the computation. We randomly select 50 clear-sky profiles from the database and compute CAT from the surface to TOA for two zenith angles. The root-mean-square error (RMSE) is computed by comparing with line-by-line results. As shown in Fig. 12, in UV-SWIR bands, there is significant absorption in certain wavelength ranges. Most of the channels have RMSE less than 0.005. The channels around 2.0 μm have larger errors, since around 2.0 μm both H_2O and CO_2 dominate absorption, which makes regression not very accurate. The surface to TOA CATs can be directly used in solar clear-sky radiative transfer calculations using Eq. (2.4a).

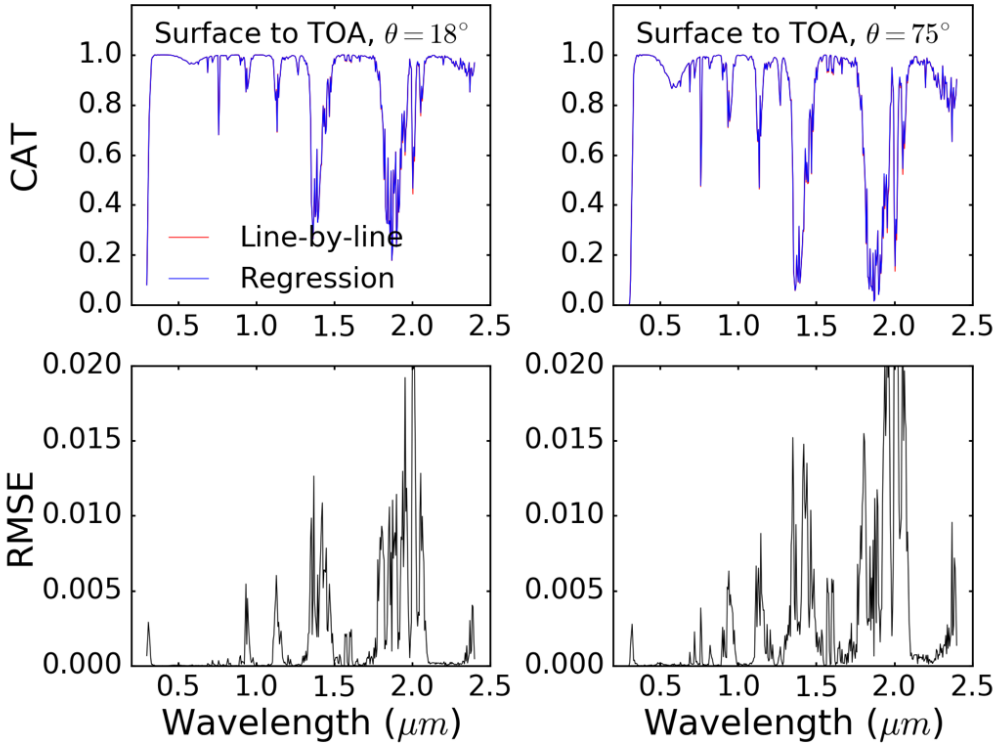

Figure 12 Hyperspectral CAT with 5 nm resolution computed by the regression method and the rigorous LBLRTM for two zenith angles θ=18° and θ=75°. The bottom row shows the RMSE of CAT.

For MODIS TIR bands, we compute the layer-to-TOA CATs by the regression method, line-by-line method and CKD method for the same atmospheric profiles as described above. The layer-to-TOA CATs are used in Eq. (3.1) to compute the brightness temperature (BT) at the TOA. The CKD implementation here is similar to Liu et al. (2015) and uses 64 integration points. Fig. 13 shows the comparisons of BTs at the TOA in 16 MODIS TIR bands computed by the three methods. In terms of RMSE relative to LBLRTM, the regression method performs more accurately than the 64-point CKD method. At band 25, the CKD has a large RMSE. Seven gases are absorptive in band 25. The absorption line overlapping may cause extra errors in the CKD method.

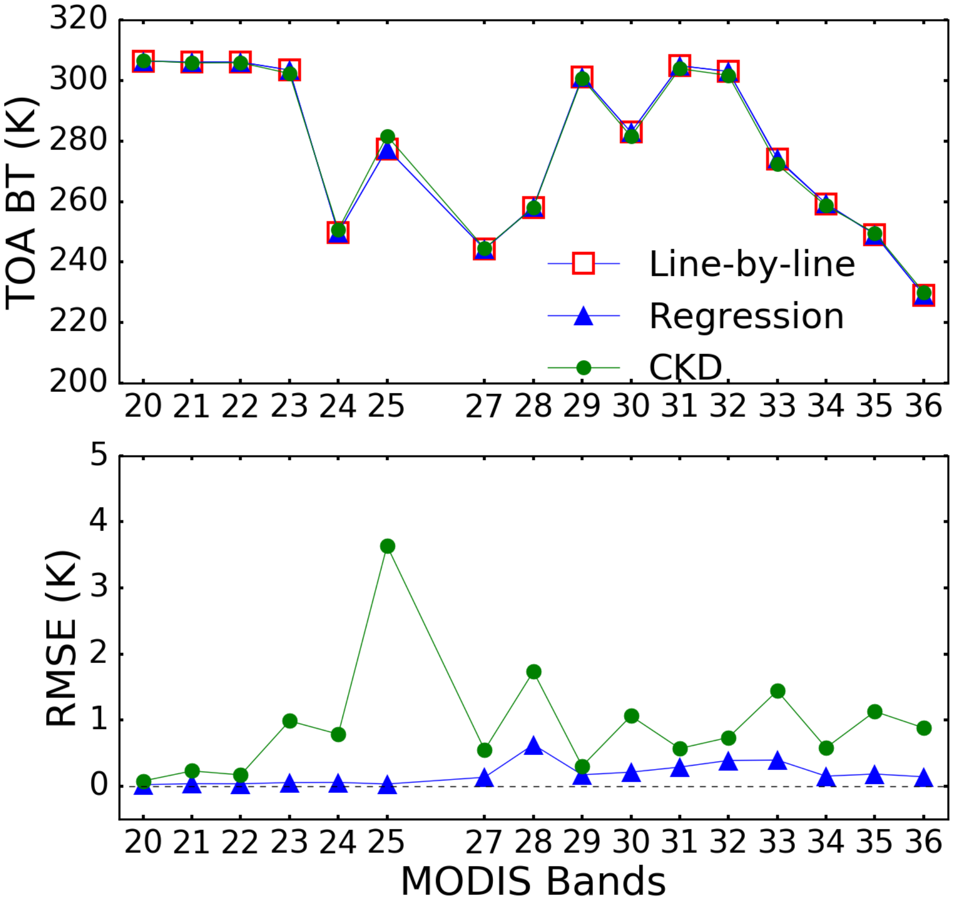

Figure 13 MODIS TIR band TOA BT simulation with CAT computed by LBLRTM, 64-point CKD, and the proposed regression method. The bottom row shows the RMSE of BT compared to LBLRTM.

In terms of implementation speed, the regression method is four orders of magnitude faster than the line-by-line method. It is also twice as fast as the 64-point CKD method. Compared with previous regression-based methods, the strength of the new regression method is that it directly parameterizes the CAOT for an inhomogeneous atmospheric path rather than making parameterizations for each homogeneous layer. This strength makes regression more efficient, especially for solar band radiative transfer calculations. For example, in Eq. (2.4a), only the surface-to-TOA CAT is needed so only one calculation is needed to compute the surface-to-TOA CAT by the new regression method in the study. However, previous regression-based methods have to do computations for each layer and then combine the results to obtain the surface-to-TOA CAT. In other words, the speed of the new regression method is independent of the number of layers. In TIR bands, all of the layer-to-TOA CATs are needed so the speed of the new regression method is not significantly faster.

CHAPTER IV

TWO-COMPONENT METHOD IN MULTIPLE SCATTERING CALCULATION

4.1 Derivation of the Two Components

The two-component method (referred to as SAA+AD) combines the improved SAA scheme by Sun et al. (2017a) and the AD method by Huang et al. (2015). Before introducing the method, some variables are defined as follows. The phase matrix in Eq. (2.1) is defined as

$$\mathbf{P}\left(\tau,u,u',\varphi-\varphi'\right)=\mathbf{L}\left(\pi-\eta_2\right)\mathbf{F}\left(\tau,\Theta\right)\mathbf{L}\left(-\eta_1\right), \tag{4.1}$$

where **F** is the scattering matrix of the scattering medium. **F** is related to the Mueller matrix, Eq. (1.5) by

$$\mathbf{F}=\frac{4\pi}{k^2C_{sca}}\mathbf{M}, \tag{4.2}$$

where C_{sca} is the bulk-averaged scattering cross section of a particle in the scattering medium. η_1 is the angle between the incident meridional plane and scattering plane, and η_2 is the angle between scattering plane and scattering meridional plane. The expressions for η_1 and η_2 are given in Hovenier et al. (2004).

Here we assume the particles in the scattering medium are randomly oriented with mirror symmetry so **F** can be explicitly written as

$$\mathbf{F}(\tau,\Theta)=\begin{pmatrix} a_1 & b_1 & 0 & 0 \\ b_1 & a_2 & 0 & 0 \\ 0 & 0 & a_3 & -b_2 \\ 0 & 0 & b_2 & a_4 \end{pmatrix}, \tag{4.3}$$

in which a_1, a_2, a_3 and a_4 are diagonal elements, and b_1 and b_2 are off-diagonal elements. Θ is the scattering angle defined as

$$\Theta=\arccos\left[uu'+\sqrt{\left(1-u^2\right)\left(1-u'^2\right)}\cos\left(\varphi-\varphi'\right)\right]. \tag{4.4}$$

Following Sun et al. (2017a), the a_1 element (i.e. scattering function) can be written as

$$a_1\left(\tau,\Theta\right)=f_1 a_1^f\left(\tau,\Theta\right)+(1-f_1)a_1^d\left(\tau,\Theta\right), \tag{4.5}$$

where $a_1^f\left(\tau,\Theta\right)$ and $a_1^d\left(\tau,\Theta\right)$ are forward (superscript '*f*') and diffuse (superscript '*d*') scattering functions respectively. f_1 is a constant representing the proportion of total scattering energy that is in the forward directions. $a_1^f\left(\tau,\Theta\right)$ is

$$a_1^f\left(\tau,\Theta\right)=\begin{cases}\frac{1}{f_1}\left[a_1\left(\tau,\Theta\right)-g\left(\tau,\Theta\right)\right], & \Theta\le\Theta_t \\ 0, & \Theta>\Theta_t\end{cases}, \tag{4.6}$$

and $a_1^d\left(\tau,\Theta\right)$ is

$$a_1^d\left(\tau,\Theta\right)=\frac{1}{1-f_1}\begin{cases}g\left(\tau,\Theta\right), & \Theta\le\Theta_t \\ a_1\left(\tau,\Theta\right), & \Theta>\Theta_t\end{cases}, \tag{4.7}$$

in which Θ_t is the truncation angle. The forward scattering function is nonzero only with scattering angles smaller than Θ_t. The function $g(\tau,\Theta)$ is introduced to keep the diffuse scattering function nonzero in forward scattering angles. The goal is to make $a_1^d(\tau,\Theta)$ a less anisotropic and smooth function so that it can be expanded accurately with a few GSF terms. Thus, $g(\tau,\Theta)$ should be a smooth function without sharp peaks. Here the $g(\tau,\Theta)$ function is consistent with Sun et al. (2017a),

$$g(\tau,\Theta) = a_1(\tau,\Theta_t)\exp\left[-\zeta(\tau)\left(\frac{\cos\Theta - \cos\Theta_t}{1-\cos\Theta_t}\right)\right], \tag{4.8}$$

where ζ is a parameter that determines the gradient of $g(\tau,\Theta)$. A value of ζ is selected to make the expansion of Eq. (4.7) accurate for radiative transfer calculations with certain number of GSF terms. The forward and diffuse scattering functions are all normalized, so f_1 is computed by

$$f_1 = \frac{1}{2}\int_0^{\Theta_t}\left[a_1(\tau,\Theta) - g(\tau,\Theta)\right]\sin\Theta \, d\Theta. \tag{4.9}$$

The forward and diffuse scattering matrices are defined as

$$\mathbf{F}^f(\tau,\Theta) = \frac{a_1^f(\tau,\Theta)}{a_1(\tau,\Theta)}\mathbf{F}(\tau,\Theta), \tag{4.10a}$$

$$\mathbf{F}^d(\tau,\Theta) = \frac{a_1^d(\tau,\Theta)}{a_1(\tau,\Theta)}\mathbf{F}(\tau,\Theta). \tag{4.10b}$$

Thus, the forward and diffuse scattering matrices satisfy

$$\mathbf{F}(\tau,\Theta) = f_1\mathbf{F}^f(\tau,\Theta) + (1-f_1)\mathbf{F}^d(\tau,\Theta). \tag{4.11}$$

Fig. 14 shows an example of a forward scattering matrix that is nonzero only within a few degrees of the forward scattering direction. Fig. 15 shows the corresponding original and diffuse scattering matrix. The diffuse scattering function is smooth in forward scattering directions.

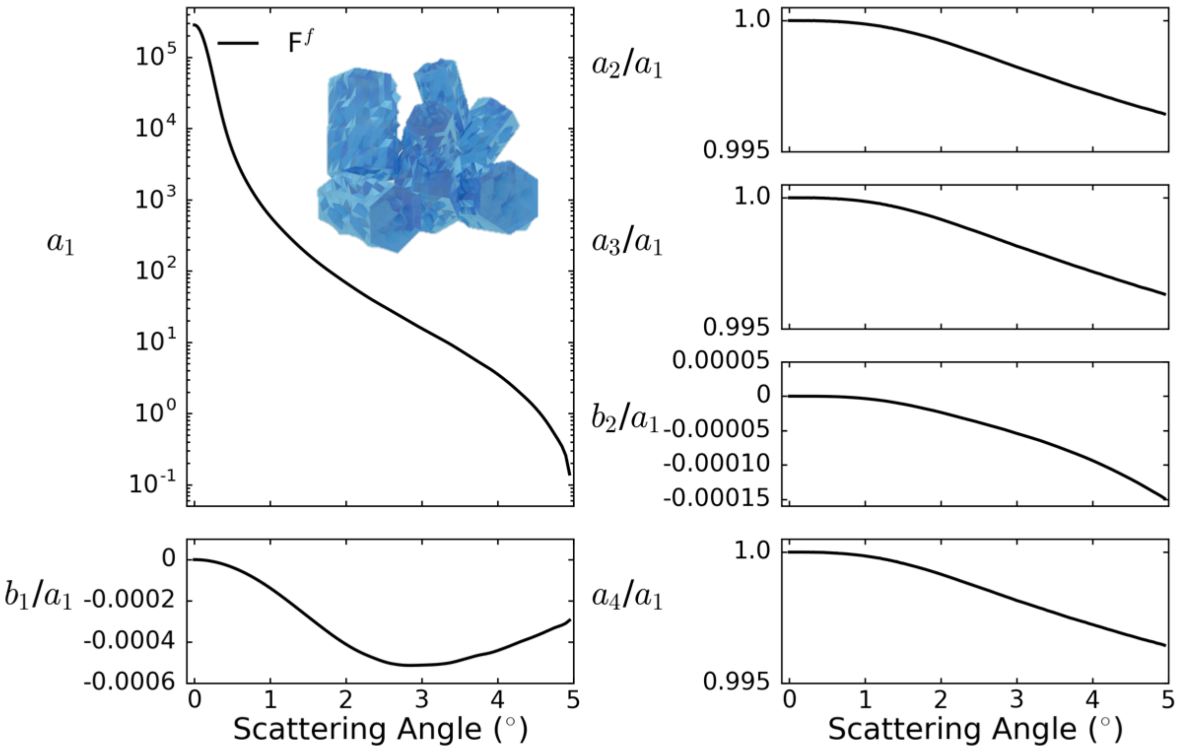

Figure 14 Forward scattering matrix elements of an ice cloud with effective radius 30 μm at wavelength 0.865 μm. The ice particle shape is a roughened 8-hexagonal column aggregate defined in Yang et al. (2013).

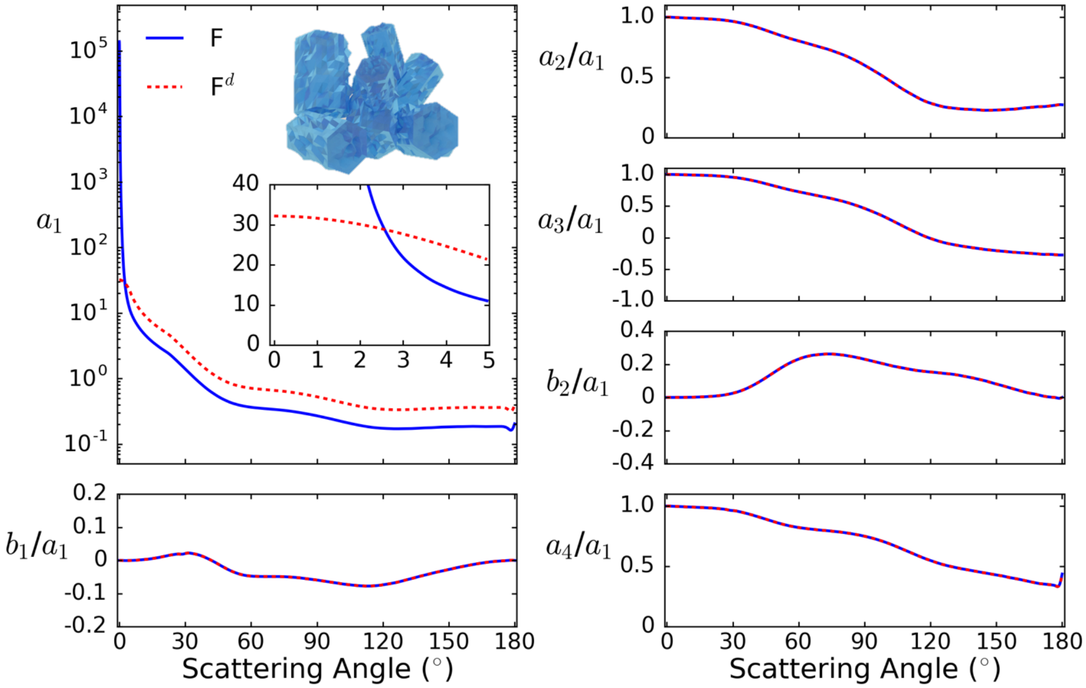

Figure 15 Diffuse scattering matrix elements of an ice cloud with effective radius 30 μm at wavelength 0.865 μm. The inset plot shows the a1 elements of F and Fd at 0 to 5° scattering angles. The ice particle shape is a roughened 8-hexagonal column aggregate defined in Yang et al. (2013).

The forward and diffuse phase matrices can be obtained by Eq. (4.1),

$$\mathbf{P}^f\left(\tau,u,u',\varphi-\varphi'\right)=\mathbf{L}\left(\pi-\eta_2\right)\mathbf{F}^f\left(\tau,\Theta\right)\mathbf{L}\left(-\eta_1\right), \tag{4.12a}$$

$$\mathbf{P}^d\left(\tau,u,u',\varphi-\varphi'\right)=\mathbf{L}\left(\pi-\eta_2\right)\mathbf{F}^d\left(\tau,\Theta\right)\mathbf{L}\left(-\eta_1\right), \tag{4.12b}$$

so that we have

$$\mathbf{P}\left(\tau,u,u',\varphi-\varphi'\right)=f_1\mathbf{P}^f\left(\tau,u,u',\varphi-\varphi'\right)+(1-f_1)\mathbf{P}^d\left(\tau,u,u',\varphi-\varphi'\right). \tag{4.13}$$

The Stokes vector in Eq. (2.1) can be written as the sum of forward and diffuse components,

$$\mathbf{I}\left(\tau,u,\varphi\right)=\mathbf{I}^d\left(\tau,u,\varphi\right)+\mathbf{I}^f\left(\tau,u,\varphi\right). \tag{4.14}$$

Substituting Eqs. (4.13) and (4.14) into Eq. (2.1), we obtain two equations,

$$
\begin{aligned}
u\frac{\partial \mathbf{I}^d\left(\tau,u,\varphi\right)}{\partial\tau} &= \mathbf{I}^d\left(\tau,u,\varphi\right) \\
&-\frac{(1-f_1)\varpi(\tau)}{4\pi}\int_{-1}^{1}du'\int_{0}^{2\pi}d\varphi'\mathbf{P}^d\left(\tau,u,u',\varphi-\varphi'\right)\mathbf{I}^d\left(\tau,u',\varphi'\right) \\
&-\frac{f_1\varpi(\tau)}{4\pi}\int_{-1}^{1}du'\int_{0}^{2\pi}d\varphi'\mathbf{P}^f\left(\tau,u,u',\varphi-\varphi'\right)\mathbf{I}^d\left(\tau,u',\varphi'\right) \\
&-\frac{(1-f_1)\varpi(\tau)}{4\pi}\int_{-1}^{1}du'\int_{0}^{2\pi}d\varphi'\mathbf{P}^d\left(\tau,u,u',\varphi-\varphi'\right)\mathbf{I}^f\left(\tau,u',\varphi'\right) \\
&-\left[1-\varpi(\tau)\right]\mathbf{B}\left[T(\tau)\right],
\end{aligned}
\tag{4.15}
$$

and

$$
\begin{aligned}
u\frac{\partial \mathbf{I}^f\left(\tau,u,\varphi\right)}{\partial\tau} &= \mathbf{I}^f\left(\tau,u,\varphi\right) \\
&-\frac{f_1\varpi(\tau)}{4\pi}\int_{-1}^{1}du'\int_{0}^{2\pi}d\varphi'\mathbf{P}^f\left(\tau,u,u',\varphi-\varphi'\right)\mathbf{I}^f\left(\tau,u',\varphi'\right).
\end{aligned}
\tag{4.16}
$$

Eqs. (4.15) and (4.16) are the diffuse and forward RTEs respectively. The last two terms on the right-hand side of Eq. (4.15) serve as sources of the diffuse RTE. Note that the energy of the forward solution is concentrating on the forward several degrees of scattering angle around the incident direction, and the contribution of the forward solution to reflection is negligible. Thus, for convenience, the non-negative variable μ instead of u is used to denote zenith directions of the forward solution. The source of incident radiation in the forward RTE is solar, so its boundary condition at the TOA is

$$
\mathbf{I}^f\left(0,-\mu,\varphi\right)=\mathbf{I}_{\mathrm{s}}\left(0,-\mu,\varphi\right). \tag{4.17}
$$

The boundary condition of Eq. (4.15) at the TOA is a zero vector. The solution to Eq. (4.16) is one of the source terms in Eq. (4.15). We have to first solve Eq. (4.16) and use the solution to solve Eq. (4.15). Sun et al. (2017a) uses the SAA and SOS methods to solve the coupled forward and diffuse RTEs. In this study, we use SAA to solve Eq. (4.16) and use the AD method to solve Eq. (4.15).

4.2 Forward Component Solution

To simplify the process to solve the forward part using SAA, we consider the scalar version of Eq. (4.16),

$$\begin{aligned} -\mu\frac{\partial I^f\left(\tau,-\mu,\varphi\right)}{\partial\tau} &= I^f\left(\tau,-\mu,\varphi\right) \\ &-\frac{f_1\varpi(\tau)}{4\pi}\int_0^1 d\mu'\int_0^{2\pi} d\varphi' a_1^f\left(\tau,-\mu,\mu',\varphi-\varphi'\right)I^f\left(\tau,\mu',\varphi'\right), \end{aligned} \tag{4.18}$$

where $I^f\left(\tau,-\mu,\varphi\right)$ is forward radiance. The polarizations are approximated by first and second order scatterings, which have exact analytical solutions. Hovenier et al. (2004) shows that polarization calculations converge faster in terms of scattering orders than radiance. In this study, Eq. (4.18) is solved by the SAA method introduced by Sun et al. (2017a). Sun et al. (2017a) only considers a single-layer case. Here we further extend the SAA method to a multi-layer case so that it can be applied to an inhomogeneous atmosphere.

Using the SAA (Sun et al. 2017a), the solution to Eq. (4.18) is approximated by a 2-dimensional Gaussian function,

$$I^f(\tau,-\mu,\varphi)\approx\frac{1}{2\pi}\frac{F}{\sqrt{V_{nx}V_{ny}}}\exp\left(-\frac{n_x^2}{2V_{nx}}-\frac{n_y^2}{2V_{ny}}\right), \tag{4.19}$$

where F, V_{nx}, and V_{ny} are parameters determined by the scattering media properties, and n_x and n_y are defined as

$$n_x = \sin\theta\cos\varphi\cos\theta_b - \cos\theta\sin\theta_b\,, \tag{4.20a}$$

$$n_y = \sin\theta\sin\varphi\,, \tag{4.20b}$$

where θ_b is defined below.

By substituting Eq. (4.19) into Eq. (4.18) and applying a suitable approximation (Sun et al. 2017a), we can obtain the analytical equations of F, V_{nx}, and V_{ny}. In Sun et al. (2017a), the parameters are given for a single layer. In this study, we derive the iterative expressions of the three parameters for multiple layers,

$$V_{ny,n} = \frac{s_n}{P_n}\frac{\frac{P_n}{s_n}V_{ny,n-1} + \tanh(s_n\tau_{eff,n})}{1+\frac{P_n}{s_n}V_{ny,n-1}\tanh(s_n\tau_{eff,n})}\,, \tag{4.21a}$$

$$V_{nx,n} = \frac{s_n}{P_n\cos^2\theta_{b,n}}\sqrt{\begin{aligned}&e^{-2\gamma_n}V^2_{nx,n-1}\cos^4\theta_{b,n-1}P_n^2\\&+s_n^2\left[(1-e^{-2\gamma_n})(1+\sin^2\theta_{b,n}\sin^2\theta_{b,n})-4\gamma_n\sin^2\theta_{b,n}\right]\end{aligned}}\,, \tag{4.21b}$$

$$F_n = \exp[-(1-\varpi_n)\tau_{eff,n}]\tilde{F}_n\,, \tag{4.21c}$$

$$\tilde{F}_n = \frac{\cos\theta_{n-1,b}\tilde{F}_{n-1}}{\cos\theta_{b,n}e^{\gamma_{b,n}/2}\sqrt{V_{ny,n-1}\frac{P_n}{s_n}\sinh(s_n\tau_{eff,n})+\cosh(s_n\tau_{eff,n})}}\,, \tag{4.21d}$$

in which the subscripts 'n' and 'n-1' denote the parameters in layers n and $n-1$, respectively. The incident light (e.g. solar radiation) enters the first (top) layer and exits the last (lower) layer. The parameters in the first layer are,

$$V_{ny,1} = \frac{s_1}{P_1}\tanh(s_1\tau_{eff,1})\,, \tag{4.22a}$$

$$V_{nx,1} = \frac{s_1}{P_1} \frac{\sqrt{(1-e^{-2\gamma_1})(1+\sin^2\theta_0 \sin^2\theta_{b,1}) - 4\gamma_1 \sin^2\theta_{b,1}}}{\cos^2\theta_{b,1}}, \tag{4.22b}$$

$$\tilde{F}_0 = \exp[-(1-\varpi_1)\tau_{eff,1}]F_0, \tag{4.22c}$$

$$\tilde{F}_1 = \frac{\cos\theta_0 \tilde{F}_0}{\cos\theta_b e^{\gamma_b/2} \sqrt{\cosh(s\tau_{eff,1})}}. \tag{4.22d}$$

The variables on the right-hand side of Eqs. (4.21) and (4.22) are defined as,

$$\varpi_n = f_{1,n}\varpi_{0,n}, \tag{4.23a}$$

$$P_n = 1 - \varpi_n, \tag{4.23b}$$

$$s_n = \sqrt{2D_n P_n}, \tag{4.23c}$$

$$D_n = \frac{\varpi_n \Lambda_n}{4}, \tag{4.23d}$$

$$\Lambda_n = \frac{1}{2}\int_0^{\pi} a_{1,n}^f \sin^3\Theta d\Theta, \tag{4.23e}$$

$$\tau_n = \int_0^{\gamma_{b,n}} \frac{\cos\theta_{b,n}}{P_n V_{nx,n}} d\gamma, \tag{4.23f}$$

$$\sin\theta_{b,n} = e^{-\gamma}\sin\theta_{b,n-1}, \theta_{b,1} = \theta_0, \tag{4.23g}$$

$$\tau_{eff,n} = \int_0^{\gamma_{b,n}} \frac{1}{P_n V_{nx,n}} d\gamma, \tag{4.23h}$$

in which $\varpi_{0,n}$ and τ_n are the single-scattering albedo and optical thickness of the scattering media in the *n*th layer. τ in Eq. (4.19) is the sum of τ_n. $a_{1,n}^f$ is the scattering function of the *n*th layer. $f_{1,n}$ is the f_1 parameter for the layer n phase function. θ_0 is the incident zenith angle.

The two-order scattering approximation is used to compute polarization of the forward RTE, Eq. (4.16), and can be expressed as

$$\mathbf{I}^f\left(\tau,-\mu,\varphi\right)\approx\mathbf{I}_1^f\left(\tau,-\mu,\varphi\right)+\mathbf{I}_2^f\left(\tau,-\mu,\varphi\right), \tag{4.24}$$

where subscripts “1” and “2” denote the first and second orders of scattering. The first order scattering is expressed as,

$$\mathbf{I}_1^f\left(\tau,-\mu,\varphi\right)=\frac{F_0}{4}\sum_{l=1}^{L}\left[f_{1,l}\varpi_{0,l}\mathbf{P}_l\left(-\mu,\mu_0,\varphi-\varphi_0\right)c\left(\tau_l,\mu,\mu_0\right)e^{-\left(\frac{\tau_{tl}}{\mu_0}+\frac{\tau_{bl}}{\mu}\right)}\right], \tag{4.25}$$

where τ_{tl} and τ_{bl} are the optical thicknesses above and below the layer l respectively. The function c (Hovenier et al. 2004) is written as,

$$c\left(\tau,\mu,\mu_0\right)=\begin{cases}\dfrac{\mu_0}{\mu_0-\mu}\left(e^{-\frac{\tau}{\mu_0}}-e^{-\frac{\tau}{\mu}}\right), & \mu\neq\mu_0\\ \dfrac{\tau}{\mu_0}e^{-\frac{\tau}{\mu_0}}, & \mu=\mu_0\end{cases}. \tag{4.26}$$

The second order scattering is expressed as

$$\begin{aligned}&\mathbf{I}_2^f\left(\tau,-\mu,\varphi\right)=\frac{F_0}{4}\int_0^1 d\mu'\int_0^{2\pi}d\varphi'\\ &\left\{\mu_0\sum_{l=1}^{L}\left[e^{-\left(\frac{\tau_{tl}}{\mu_0}+\frac{\tau_{bl}}{\mu}\right)}\varpi_{0,l}^2 h\left(\tau_l,\mu,\mu_0,\mu'\right)\mathbf{P}_l\left(-\mu,\mu',\varphi-\varphi'\right)\mathbf{P}_l\left(\mu',\mu_0,\varphi'-\varphi_0\right)\right]\right.\\ &\left.+\sum_{l=1}^{L-1}\sum_{m=l+1}^{L}\left[\begin{array}{l}e^{-\left(\frac{\tau_{tl}}{\mu_0}+\frac{\tau_{lm}}{\mu'}+\frac{\tau_{bm}}{\mu}\right)}\varpi_{0,l}\varpi_{0,m}c\left(\tau_l,\mu',\mu_0\right)c\left(\tau_m,\mu,\mu'\right)\\ \cdot\mathbf{P}_l\left(\mu',\mu_0,\varphi'-\varphi_0\right)\mathbf{P}_m\left(-\mu,\mu',\varphi-\varphi'\right)\end{array}\right]\right\},\end{aligned} \tag{4.27}$$

where τ_{lm} is the optical thickness between layer *l* and *m*. The function *h* is defined as

$$h\left(\tau,\mu,\mu_0,\mu'\right)=$$
$$\begin{cases}
\dfrac{1}{4\left(\mu_0-\mu'\right)}\left[\dfrac{\mu_0}{\mu_0-\mu}\left(e^{-\frac{\tau}{\mu_0}}-e^{-\frac{\tau}{\mu}}\right)-\dfrac{\mu'}{\mu'-\mu}\left(e^{-\frac{\tau}{\mu'}}-e^{-\frac{\tau}{\mu}}\right)\right], & \mu,\mu_0 \text{ and } \mu' \text{ are different} \\
\dfrac{1}{4\left(\mu_0-\mu'\right)}\left[\dfrac{\tau}{\mu_0}e^{-\frac{\tau}{\mu_0}}-\dfrac{\mu'}{\mu'-\mu_0}\left(e^{-\frac{\tau}{\mu'}}-e^{-\frac{\tau}{\mu_0}}\right)\right], & \mu=\mu_0\neq\mu' \\
\dfrac{1}{4\left(\mu_0-\mu\right)}\left[\dfrac{\mu_0}{\mu_0-\mu}\left(e^{-\frac{\tau}{\mu_0}}-e^{-\frac{\tau}{\mu}}\right)-\dfrac{\tau}{\mu}e^{-\frac{\tau}{\mu}}\right], & \mu_0\neq\mu=\mu' \\
\dfrac{1}{4\left(\mu_0-\mu\right)}\left[\dfrac{\tau}{\mu_0}e^{-\frac{\tau}{\mu_0}}-\dfrac{\mu}{\mu_0-\mu}\left(e^{-\frac{\tau}{\mu_0}}-e^{-\frac{\tau}{\mu}}\right)\right], & \mu\neq\mu_0=\mu' \\
\dfrac{\tau^2}{8\mu_0^2}e^{-\frac{\tau}{\mu_0}}, & \mu=\mu_0=\mu'
\end{cases} \qquad (4.28)$$

The first term on the right-hand side of Eq. (4.27) applies when the two orders of scattering occur in the same homogeneous layer. The second term applies when the two orders of scattering occur in two different layers.

Except for polarization, Eqs. (4.25) and (4.27) also contain an accurate radiance solution for the first and second orders of scattering. The SAA solution, Eq. (4.19), as an approximation, is the sum of all orders of scattering. To improve the accuracy of the forward solution, we can replace the first and second orders of scattering components in Eq. (4.19) with the accurate counterparts in Eqs. (4.25) and (4.27) (Sun et al. 2017a).

4.3 Diffuse Component Solution

In the diffuse RTE, Eq. (4.15), the forward phase matrix can be approximated as a Delta function matrix,

$$\mathbf{P}^{f} \approx 4\pi\delta\left(\mu-\mu_{0}\right)\delta\left(\varphi-\varphi_{0}\right)\mathbf{1}, \tag{4.29}$$

where **1** is a 4×4 identity matrix. The validity of Eq. (4.29) can be seen in Fig. 14. The forward scattering matrix is nonzero only when the scattering angle is less than 5°. In this scattering angle range, the off-diagonal scattering matrix elements are close to zero while the diagonal scattering matrix elements are almost the same as a_1.

Eq. (4.19) can be approximated as (Sun et al. 2017a)

$$I^{f} \approx F_{0}e^{-\frac{\tau_{s}}{\mu_{0}}}\delta\left(\mu-\mu_{0}\right)\delta\left(\varphi-\varphi_{0}\right), \tag{4.30}$$

where τ_s is

$$\tau_{s} = \left(1-f_{1}\varpi\right)\tau . \tag{4.31}$$

In the diffuse RTE, Eq. (4.15), applying Eq. (4.30), the forward Stokes vector can be approximated as,

$$\mathbf{I}^{f} \approx F_{0}e^{-\frac{\tau_{s}}{\mu_{0}}}\delta\left(\mu-\mu_{0}\right)\delta\left(\varphi-\varphi_{0}\right)\begin{pmatrix} 1 & 0 & 0 & 0 \end{pmatrix}^{\mathrm{T}}, \tag{4.32}$$

which is equal to the incident solar radiation after attenuation with optical thickness τ_s. Substituting Eqs. (4.29) and (4.32) into Eq. (4.15), we obtain

$$
\begin{aligned}
&u\frac{\partial \mathbf{I}^{d}\left(\tau_{s},u,\varphi\right)}{\partial \tau_{s}}= \\
&\mathbf{I}^{d}-\frac{\varpi_{s}(\tau_{s})}{4\pi}\int_{-1}^{1}du'\int_{0}^{2\pi}d\varphi'\mathbf{P}^{d}\left(\tau_{s},u,u',\varphi-\varphi'\right)\mathbf{I}^{d}\left(\tau_{s},u',\varphi'\right) \\
&-\frac{F_{0}\varpi_{s}(\tau_{s})}{4\pi}\mathbf{P}^{d}\left(\tau_{s},u,\mu_{0},\varphi-\varphi_{0}\right)\begin{pmatrix} 1 & 0 & 0 & 0 \end{pmatrix}^{\mathrm{T}}e^{-\frac{\tau}{\mu_{0}}} \\
&-\left[1-\varpi_{s}(\tau_{s})\right]\mathbf{B}\left[T(\tau_{s})\right],
\end{aligned}
\tag{4.33}
$$

where ϖ_s is

$$\varpi_{s}=\frac{(1-f_{1})\varpi}{1-f_{1}\varpi}. \tag{4.34}$$

From Eqs. (4.31), (4.33) and (4.34), the diffuse RTE is equivalent to a scaled RTE based on the similarity relation (Liou 2002). The scaled diffuse RTE, Eq. (4.33) is now decoupled from the forward RTE, Eq. (4.16). Eq. (4.33) is then solved by the AD method as follows.

In the formulism of the AD method, all quantities relate to the diffused RTE. The superscript "*d*", and subscript "*s*" for τ_s and ϖ_s are omitted. The Stokes vectors at the top ($\mathbf{I}_{tp}$) and the bottom ($\mathbf{I}_{bt}$) of all scattering layers can be computed by

$$\mathbf{I}_{tp}(\mu,\varphi)=\frac{1}{\pi}\int_{0}^{1}\mu'\,d\mu'\int_{0}^{2\varphi}\mathbf{R}\left(\mu,\mu',\varphi-\varphi'\right)\mathbf{I}_{inc}(\mu',\varphi'), \tag{4.35}$$

and

$$\mathbf{I}_{bt}(-\mu,\varphi)=e^{-\frac{\tau_{tot}}{\mu}}\mathbf{I}_{inc}(-\mu,\varphi)+\frac{1}{\pi}\int_{0}^{1}\mu'\,d\mu'\int_{0}^{2\varphi}\mathbf{T}\left(\mu,\mu',\varphi-\varphi'\right)\mathbf{I}_{inc}(\mu',\varphi'), \tag{4.36}$$

where $\mathbf{I}_{inc}$ is the incident Stokes vector.

For incident solar radiation, $\mathbf{I}_{inc}$ is equal to Eq. (2.3). **R** and **T** are reflection and transmission matrices of the scattering medium respectively. Except for **R** and **T**, upward and downward matrices **U** and **D** are also used in the adding-doubling formulism. **R**, **T**, **U** and **D** describe incident radiation from above. If incident radiation is from the bottom, we use an asterisk to denote the equivalent quantities ($\mathbf{R}^*$, $\mathbf{T}^*$, $\mathbf{U}^*$ and $\mathbf{D}^*$). **R**, **T**, **U**, **D**, $\mathbf{R}^*$, $\mathbf{T}^*$, $\mathbf{U}^*$ and $\mathbf{D}^*$ are multiple scattering matrices, which are computed by the adding-doubling process. Once the multiple scattering matrices are computed, the solution to the RTE can be easily obtained from Eqs. (4.35) and (4.36).

For accurate numerical implementation, the multiple scattering matrices and Stokes vector are expanded in Fourier series in terms of $\varphi-\varphi'$. For illustration, **R** can be written as

$$\mathbf{R}\left(\mu,\mu',\varphi-\varphi'\right)=\sum_{j=0}^{\infty}(2-\delta_{j0})\left\{\begin{matrix}\Phi_1(j\varphi)\mathbf{R}_j(\mu,\mu')\Phi_1(j\varphi') \\ +\Phi_2(j\varphi)\mathbf{R}_j(\mu,\mu')\Phi_2(j\varphi')\end{matrix}\right\}, \tag{4.37}$$

where δ_{j0} is the Kronecker delta. The diagonal matrices Φ_1 and Φ_2 are defined as

$$\Phi_1\left(\alpha\right)=diag\left(\cos\alpha,\cos\alpha,\sin\alpha,\sin\alpha\right), \tag{4.38a}$$

$$\Phi_2\left(\alpha\right)=diag\left(-\sin\alpha,-\sin\alpha,\cos\alpha,\cos\alpha\right). \tag{4.38b}$$

The Fourier component in Eq. (4.37) can be computed by

$$\mathbf{R}_j(\mu,\mu')=\frac{1}{2\pi}\int_0^{2\pi}d(\varphi-\varphi')\left\{\begin{matrix}\Phi_1\left[j(\varphi-\varphi')\right] \\ +\Phi_2\left[j(\varphi-\varphi')\right]\end{matrix}\right\}\mathbf{R}\left(\mu,\mu',\varphi-\varphi'\right). \tag{4.39}$$

The adding-doubling calculation is implemented in each independent Fourier expansion term. Although in Eq. (4.37) the Fourier series is infinite, only the first few terms are needed in the calculation to satisfy the specified accuracy requirement. In later descriptions, the multiple scattering matrix notations all imply Fourier components unless specified otherwise. The Fourier order index is omitted in their subscript for brevity.

The following equations are used to compute reflection and transmission matrices of a layer combined with two sublayers,

$$\mathbf{Q}_1 = \mathbf{R}^{*u}\mathbf{R}^{l}, \tag{4.40a}$$

$$\mathbf{Q}_{p+1} = \mathbf{Q}_1\mathbf{Q}_p, \tag{4.40b}$$

$$\mathbf{Q} = \sum_{p=1}^{\infty}\mathbf{Q}_p, \tag{4.40c}$$

$$\mathbf{D} = \mathbf{T}^{u} + \mathbf{Q}\mathbf{E}(\tau^{u}) + \mathbf{Q}\mathbf{T}^{u}, \tag{4.40d}$$

$$\mathbf{U} = \mathbf{R}^{l}\mathbf{E}(\tau^{u}) + \mathbf{R}^{l}\mathbf{D}, \tag{4.40e}$$

$$\mathbf{R} = \mathbf{R}^{u} + \mathbf{E}(\tau^{u})\mathbf{U} + \mathbf{T}^{*u}\mathbf{U}, \tag{4.40f}$$

$$\mathbf{T} = \mathbf{E}(\tau^{l})\mathbf{D} + \mathbf{T}^{l}\mathbf{E}(\tau^{u}) + \mathbf{T}^{l}\mathbf{D}, \tag{4.40g}$$

in which superscripts "*u*" and "*l*" denote upper and lower sublayers respectively. **Q** accounts for repeated reflections at the interface of the two sublayers. **E** is the exponential decay matrix that accounts for direct transmission. **D** and **U** represent downward and upward radiations at the interface of the two layers respectively.

Matrix multiplications and matrix-vector multiplications in Eq. (4.40) and the rest of this dissertation are discretized definite integrals as follows:

$$\mathbf{AK} = 2\int_0^1 \mu' \, d\mu' \mathbf{A}(\mu,\mu')\mathbf{K}(\mu',\mu_0), \tag{4.41a}$$

for two matrices **A** and **K**, and

$$\mathbf{KX} = 2\int_0^1 \mu' \, d\mu' \mathbf{K}(\mu,\mu')\mathbf{X}(\mu'), \tag{4.41b}$$

for matrix **K** and vector **X**.

Eq. (4.40) is the adding computation. If the two sublayers have the same optical thickness and scattering properties, the multiple scattering matrices in the two sublayers are the same. In this case, Eq. (4.40) can be used as the doubling computation.

4.4 Validation

After we obtain the diffuse solution by the AD method and the forward solution by the SAA method, we obtain the solution to the vector RTE by Eq. (4.14). To validate the two-component method, we first compare its computation results with a published dataset by Kokhanovsky et al. (2010). They use several numerically accurate vector RTE solvers to compute the reflected and transmitted Stokes vectors by a liquid cloud and an aerosol layer at wavelength 0.412 μm. The cloud and aerosol single-scattering properties are computed by Lorenz-Mie theory. Two size distributions are used to obtain the size-averaged scattering matrices of the cloud and aerosol models.

Figs. 16-19 show the SAA+AD multiple scattering computations compared with the published results in Kokanovsky et al. (2010). In the computation, the diffuse scattering matrices are expanded by GSF up to 32 orders. Figs. 16 and 17 show the Stokes vector elements of the reflected and transmitted radiation in the case of an aerosol layer. The aerosol layer has optical thickness 0.3262 and is assumed as nonabsorptive. Figs. 18 and 19 show the Stokes vector elements of the reflected and transmitted radiation in a liquid cloud layer. The liquid cloud layer has optical thickness τ=5.

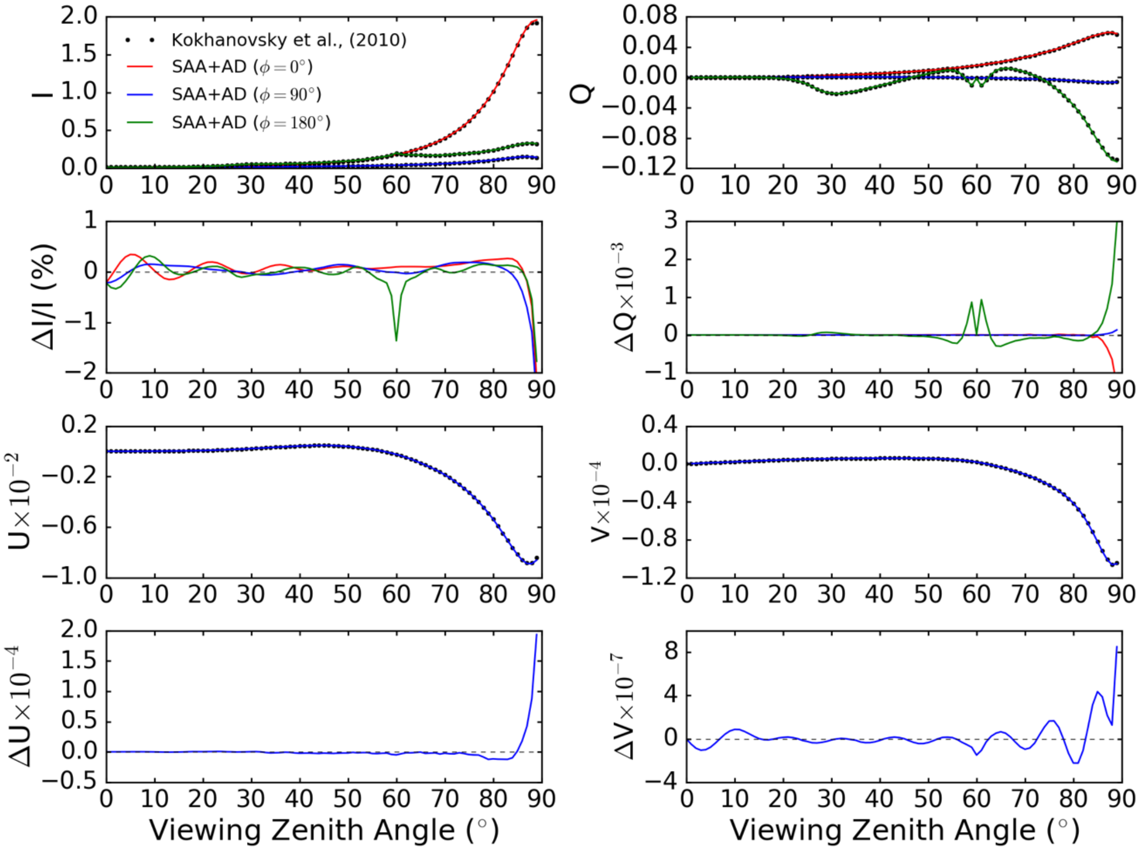

Figure 16 Stokes vector elements of the reflected radiation and the differences in the case of an aerosol layer. The Stokes vector elements are computed by the SAA+AD method and compared with the published results in Kokhanovsky et al. (2010). The solar zenith angle is 60° and the azimuth angles are 0, 90°, and 180°. The aerosol optical thickness is 0.3262. ΔI/I is relative difference in percentage, and ΔQ, ΔU and ΔV are absolute differences. The Stokes vector elements are normalized by the incident radiance so they are dimensionless.

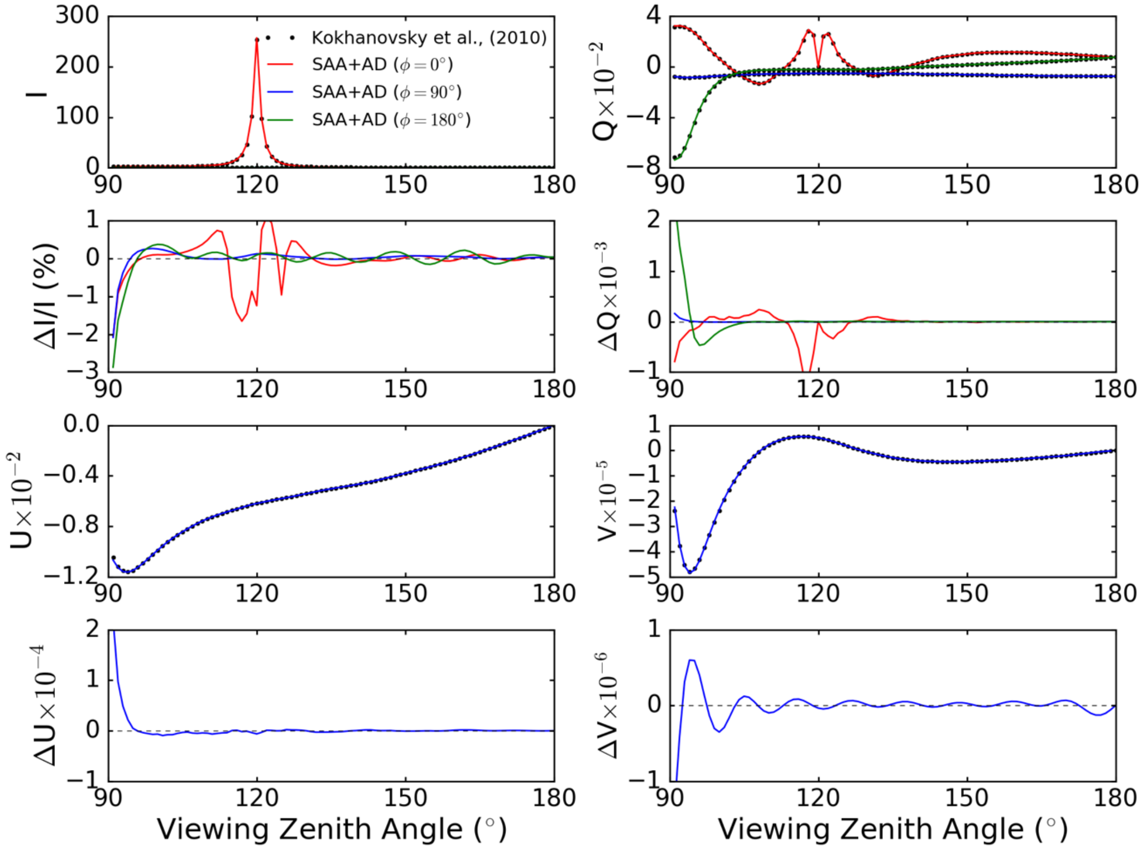

Figure 17 Stokes vector elements of the transmitted radiation and the differences in the case of an aerosol layer. The Stokes vector elements are computed by SAA+AD method and compared with the published results in Kokhanovsky et al. (2010). The solar zenith angle is 60° and the azimuth angles are 0, 90°, and 180°. The aerosol optical thickness is 0.3262. ΔI/I is the relative difference in percentage, and ΔQ, ΔU and ΔV are absolute differences. The Stokes vector elements are normalized by the incident radiance so they are dimensionless.

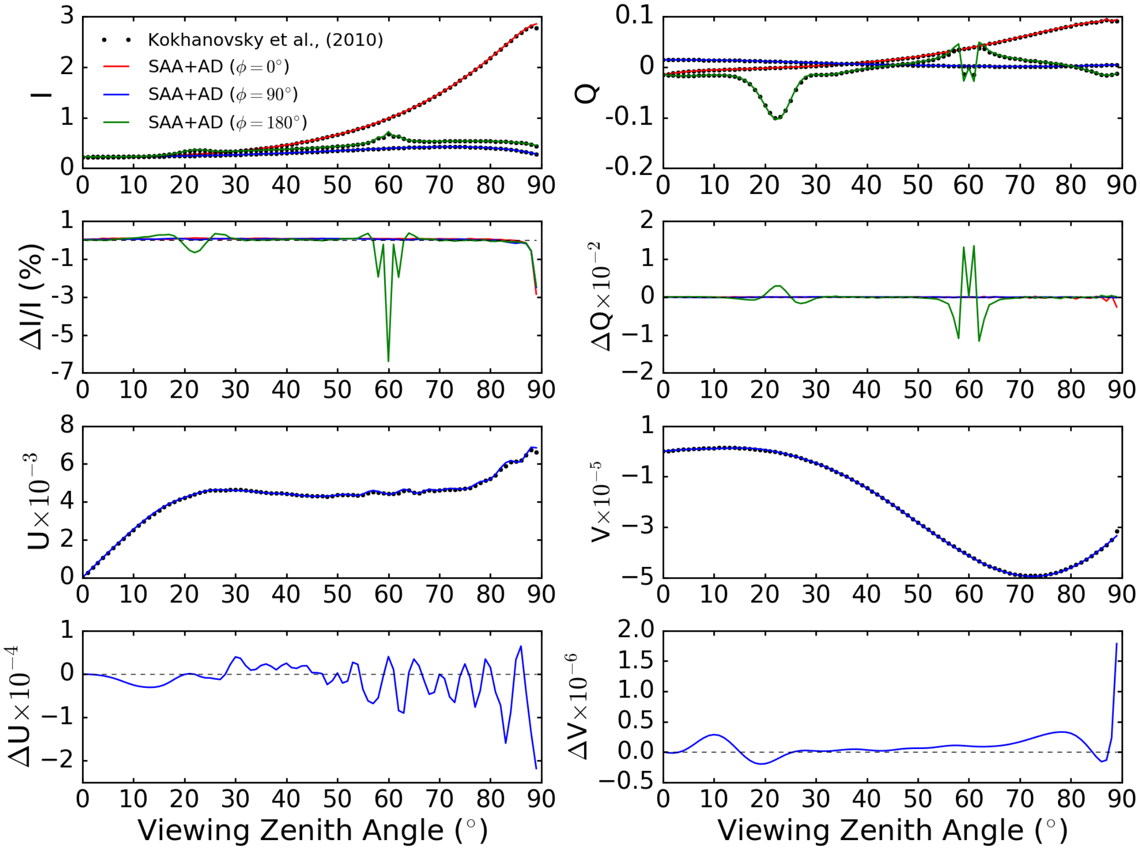

Figure 18 Stokes vector elements of the reflected radiation and the differences in the case of a cloud layer. The Stokes vector elements are computed by the SAA+AD method and compared with the published results in Kokhanovsky et al. (2010). The solar zenith angle is 60° and the azimuth angles are 0, 90°, and 180°. The aerosol optical thickness is 5. $\Delta I/I$ is the relative difference in percentage, and ΔQ, ΔU and ΔV are absolute differences. The Stokes vector elements are normalized by the incident radiance so they are dimensionless.

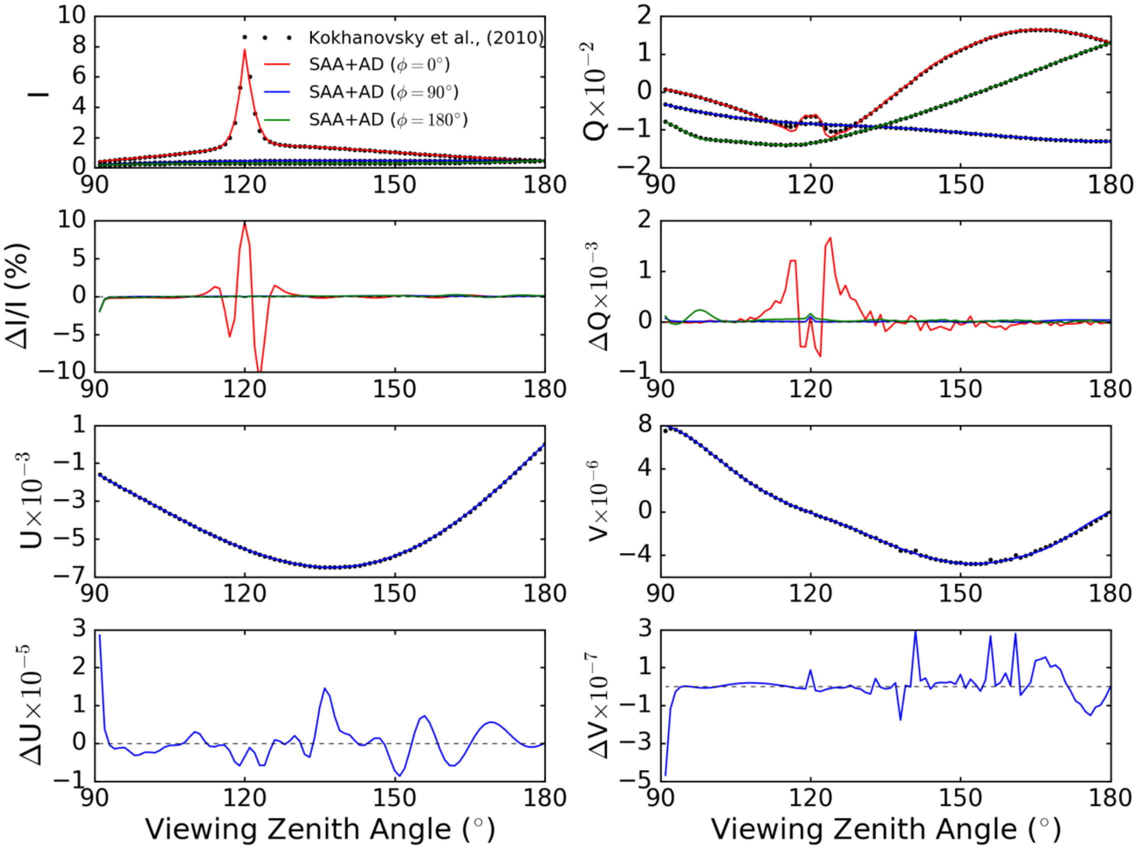

Figure 19 Stokes vector elements of the transmitted radiation and the differences in the case of a cloud layer. The Stokes vector elements are computed by the SAA+AD method and compared with the published results in Kokhanovsky et al. (2010). The solar zenith angle is 60° and the azimuth angles are 0, 90°, and 180°. The aerosol optical thickness is 5. $\Delta I/I$ is the relative difference in percentage, and ΔQ, ΔU and ΔV are absolute differences. The Stokes vector elements are normalized by the incident radiance so they are dimensionless.

For reflected radiation calculation in Figs. 16 and 18, the SAA+AD method is accurate in most directions. At the backscattering direction, which has viewing zenith angle 60° and relative azimuth angle 180°, the error is larger due to enhanced backscattering by aerosol and cloud. As viewing zenith angles approach to 90°, the results become worse since the cosine of the zenith angle becomes very small. Large numerical errors are introduced by the very small value in the denominator.

For transmitted radiation calculations in Figs. 17 and 19, the SAA+AD method is also accurate in most directions. In the forward scattering direction, which has viewing zenith angle 120° and azimuth angle 0, the SAA+AD is accurate for the aerosol layer since its optical thickness is small. The first and second scattering dominates the signal in the forward direction. The percentage error of the I component is smaller than 1% in the forward scattering direction. For a cloud layer, the error in the forward scattering direction is larger but still smaller than 10% due to larger optical thickness so there is more high-order (more than 2) scattering contribution in the forward direction signal.

The forward solution contains all orders of scatterings. In the calculations, the first and second order scatterings are replaced by the accurate solutions as mentioned above. The remaining high order scatterings are less accurate because of SAA. Thus, when the first or second order scatterings dominate the signal, the solution can be accurate. In contrast, when the high order scatterings dominate the signal, the error in the solution is large. Although SAA performs worse with a large optical thickness, there is little effect on a remote sensing application. The transmitted radiation is only utilized in remote sensing when the atmosphere has small optical thickness where the sky is clear or only a thin aerosol layer exists.

Next, we validate the two-component vector RTE solver in the case of multiple scattering layers. The model atmosphere has three layers. From the top to bottom, there are an ice cloud layer, an aerosol layer and a liquid cloud layer. The optical thicknesses are 2, 0.3 and 3 respectively. The effective radii are 5, 1.0 and 10 μm respectively. The surface in the calculation is assumed to be completely absorptive so there is no interaction between the atmosphere and the surface. The wavelength is 0.865 μm. The ice cloud model is the MODIS Collection 6 model (Platnick et al. 2017), which has the particle shape of roughened 8-hexagonal column aggregate defined by Yang et al. (2013). The aerosol layer is assumed to be a dust layer. The dust particle shape is a hexahedron ensemble defined in Yang et al. (2019). The refractive index of dust aerosol is from a compiled dataset by Stegmann and Yang (2017). The dust single-scattering properties are computed by a synergistic combination of the invariant imbedding T-matrix (IITM) (Bi and Yang 2014) and physical-geometric optics method (PGOM) (Sun et al. 2017b).

As a benchmark, the rigorous AD method is used to compute the Stokes vector in reflection and transmission directions. In the calculation, the scattering matrices of the scattering layers are expanded in terms of GSF up to 2000 terms, which is accurate enough to represent the scattering matrices. We also do the computation with the DMM (Wiscombe 1977) and the TMS single-scattering correction (Nakajima and Tanaka 1988), for comparison with the two-component approach. Figs. 17 and 18 show results by the rigorous AD, and the approximate SAA+AD method and DMM + AD with the TMS single-scattering correction (DMM&TMS+AD).

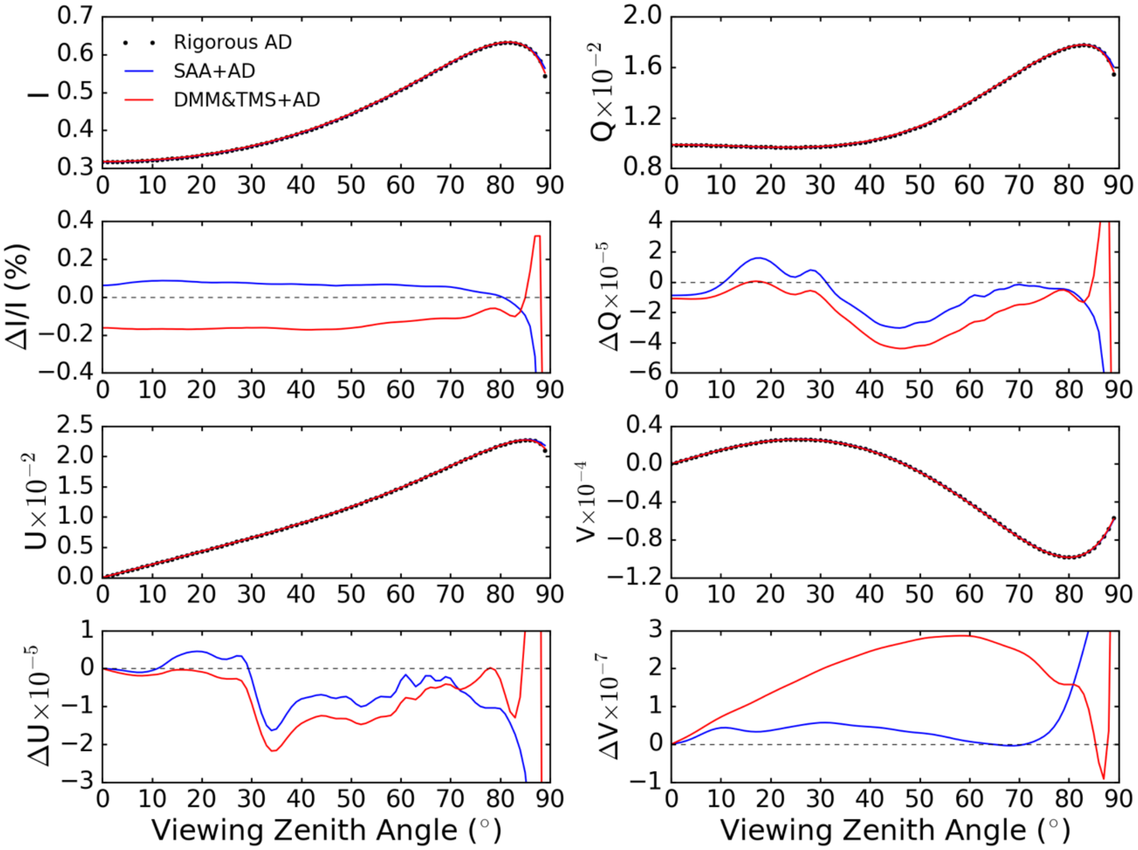

Figure 20 Stokes vectors of reflected radiation computed by the rigorous AD, and the approximate SAA+AD and DMM&TMS+AD methods for a three-layer atmosphere (from top to bottom: ice cloud, aerosol, and liquid cloud with optical thickness at 0.865 μm wavelength 2, 0.3, and 3 respectively; and effective radii 5.0, 1.0, and 10 μm respectively). The solar zenith angle is 60°. The relative azimuth angle is 90°. $\Delta I/I$ is the relative difference in percentage, and ΔQ, ΔU, and ΔV are absolute differences. The Stokes vector elements are normalized by the incident radiance so they are dimensionless.

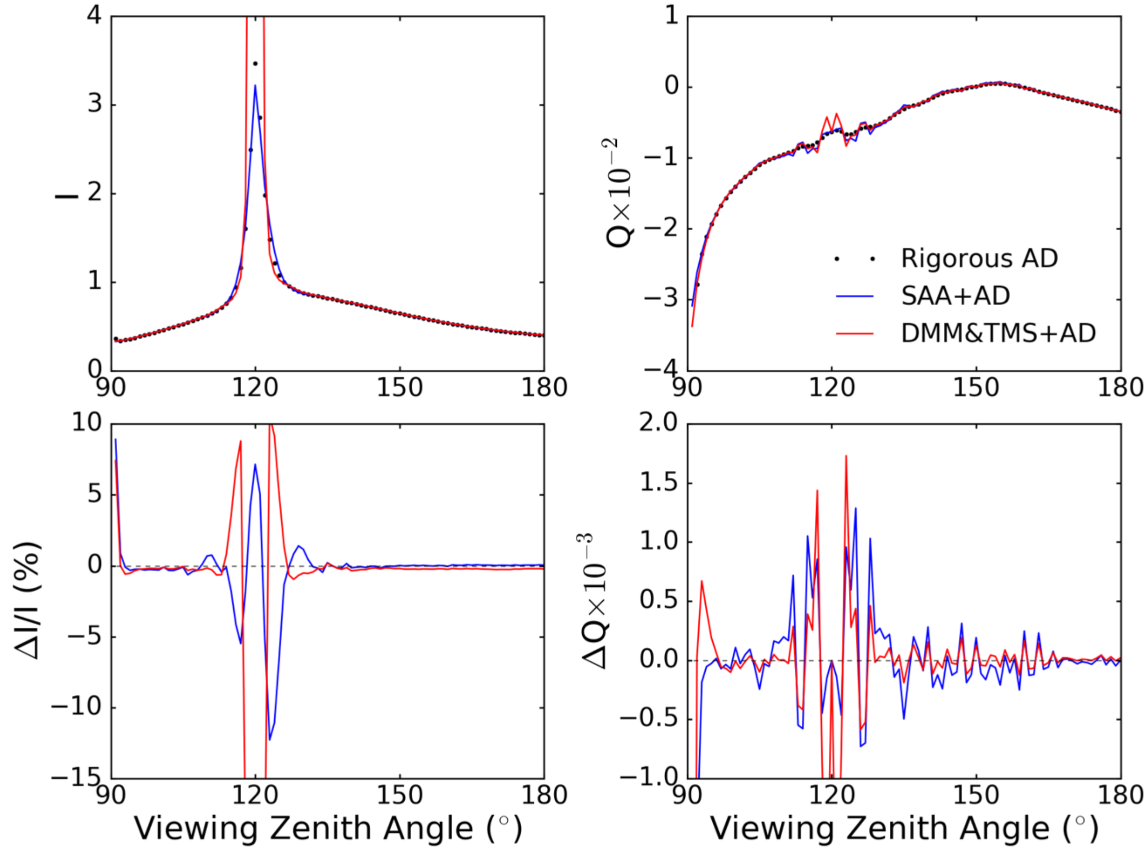

Figure 21 Stokes vectors of transmitted radiation computed by the rigorous AD, and approximate SAA+AD and DMM&TMS+AD methods for a three-layer atmosphere (from top to bottom: ice cloud, aerosol, and liquid cloud with optical thickness at 0.865 μm wavelength 2, 0.3, and 3 respectively; and effective radii 5.0, 1.0, and 10 μm respectively). The solar zenith angle is 60°. The relative azimuth angle is 0. $\Delta I/I$ is the relative difference in percentage, and ΔQ is the absolute difference. The Stokes vector elements are normalized by the incident radiance so they are dimensionless.

In reflection directions as shown in Fig. 20, the SAA+AD and DMM&TMS+AD methods are accurate in most directions compared with the rigorous AD. In transmission directions as shown in Fig. 21, the SAA+AD is much more accurate than DMM&TMS+AD in the forward transmitted direction (i.e. viewing zenith angle 120°). Note that, the total optical thickness of the model atmosphere is 5.3. The percentage error in the forward direction is less than 10%, which is similar to the single-layer cloud case.

This may suggest that the SAA+AD method works for the multi-layer case as well as for the single-layer case. In the calculation, the diffuse scattering matrices in SAA+AD method are expanded using 32 GSF terms. For DMM&TMS+AD, the scattering matrices are truncated at the 32nd expansion term. The SAA+AD is more than 3 orders of magnitude faster than the rigorous AD method, and slightly faster than the DMM&TMS+AD method.

CHAPTER V

THERMAL EMISSION IN ADDING-DOUBLING

5.1 From Adding to Doubling

As in Eq. (2.2), Eq. (4.33) can also be written as two decoupled vector RTEs with solar and thermal sources respectively. The thermal emission is isotropic in a plane-parallel atmosphere, so we only need to consider the azimuth-independent solution, which corresponds to the zero order Fourier expansion term. The azimuth-independent vector RTE is written as

$$u\frac{\partial \mathbf{I}(\tau,u)}{\partial \tau}=\mathbf{I}(\tau,u)-\frac{\varpi(\tau)}{2}\int_{-1}^{1}du'\mathbf{P}(\tau,u,u')\mathbf{I}(\tau,u')-[1-\varpi(\tau)]\mathbf{B}[T(\tau)], \quad (5.1)$$

where $\mathbf{P}(\tau,u,u')$ is the zero order Fourier component of the phase matrix, and is computed by

$$\mathbf{P}(\tau,u,u')=\frac{1}{2\pi}\int_{0}^{2\pi}\mathbf{P}(\tau,u,u',\varphi-\varphi')d\varphi' . \quad (5.2)$$

As shown in the Planck function term in Eq. (5.1), the thermal emission source is dependent on the temperature. In a planetary atmosphere, although the layer scattering property may be homogeneous, the temperature is hardly constant in the vertical direction. A direct idea for solving the vector RTE with thermal emission is to use the adding process. The adding equations of the thermal emission vector are as follows,

$$\mathbf{S}^{D}=\mathbf{S}^{uT}+\mathbf{Q}\mathbf{S}^{uT}+\mathbf{Q}\mathbf{R}^{u}\mathbf{S}^{lR}+\mathbf{R}^{u}\mathbf{S}^{lR}, \quad (5.3a)$$

$$\mathbf{S}^{U}=\mathbf{S}^{lR}+\mathbf{R}^{l}\mathbf{S}^{D}, \quad (5.3b)$$

$$\mathbf{S}^{R}=\mathbf{S}^{uR}+\mathbf{E}(\tau^{u})\mathbf{S}^{U}+\mathbf{T}^{u}\mathbf{S}^{U}, \tag{5.3c}$$

$$\mathbf{S}^{T}=\mathbf{S}^{lT}+\mathbf{E}(\tau^{l})\mathbf{S}^{D}+\mathbf{T}^{l}\mathbf{S}^{D}, \tag{5.3d}$$

where **S** is the thermal emission vector. The superscripts "*R*" and "*T*" represent upward and downward emission at the upper and lower boundaries of a layer respectively. The superscripts "*U*" and "*D*" represent upward and downward emission at the interface of two layers. Due to the symmetry of the multiple scattering matrix in the zero order Fourier component, $\mathbf{R}^*=\mathbf{R}$ and $\mathbf{T}^*=\mathbf{T}$ are considered in the formulation. Eq. (5.3) computes the total thermal emission by the two layers when the thermal emission vectors of the upper and lower layers are known.

If the two scattering layers have identical scattering properties, Eq. (5.3) can be simplified as

$$\mathbf{S}^{D}=\mathbf{S}^{uT}+\mathbf{Q}\mathbf{S}^{uT}+\mathbf{Q}\mathbf{R}^{u}\mathbf{S}^{lR}+\mathbf{R}^{u}\mathbf{S}^{lR}, \tag{5.4a}$$

$$\mathbf{S}^{U}=\mathbf{S}^{lR}+\mathbf{R}^{l}\mathbf{S}^{D}, \tag{5.4b}$$

$$\mathbf{S}^{R}=\mathbf{S}^{uR}+\mathbf{E}\mathbf{S}^{U}+\mathbf{T}^{l}\mathbf{S}^{U}=\mathbf{S}^{uR}+(\mathbf{E}+\mathbf{T}^{u})(\mathbf{1}+\mathbf{Q})(\mathbf{S}^{lR}+\mathbf{R}^{u}\mathbf{S}^{uT}), \tag{5.4c}$$

$$\mathbf{S}^{T}=\mathbf{S}^{lT}+\mathbf{E}\mathbf{S}^{D}+\mathbf{T}^{u}\mathbf{S}^{D}=\mathbf{S}^{lT}+(\mathbf{E}+\mathbf{T}^{u})(\mathbf{1}+\mathbf{Q})(\mathbf{S}^{uT}+\mathbf{R}^{u}\mathbf{S}^{lR}). \tag{5.4d}$$

Even though, as shown in Eq. (5.4), the multiple scattering matrices are identical in the two layers, the thermal emission vectors are still different in the two layers due to different temperatures. Thus, we cannot implement the doubling calculation, which is more computationally efficient than the adding calculation. However, if we make some assumptions, the inhomogeneous thermal source can be decomposed into the sum of homogenous components.

For convenience in the followed discussion, we define the two matrices,

$$\mathbf{t} \equiv \mathbf{E} + \mathbf{T}^{u}, \tag{5.5a}$$

$$\mathbf{q} \equiv \mathbf{1} + \mathbf{Q}, \tag{5.5b}$$

so Eqs. (5.4c-d) can be expressed as

$$\mathbf{S}^{R} = \mathbf{S}'^{R} + \mathbf{tq}(\mathbf{S}''^{R} + \mathbf{R}'\mathbf{S}'^{T}), \tag{5.6a}$$

$$\mathbf{S}^{T} = \mathbf{S}''^{T} + \mathbf{tq}(\mathbf{S}'^{T} + \mathbf{R}'\mathbf{S}''^{R}). \tag{5.6b}$$

We introduce the following notation:

$$\mathbf{S}^{R}_{0,2^{n+1}} = \mathbf{S}^{R}_{0,2^{n}} + \mathbf{t}_{n}\mathbf{q}_{n}(\mathbf{S}^{R}_{2^{n},2^{n+1}} + \mathbf{R}_{n}\mathbf{S}^{T}_{0,2^{n}}), \tag{5.7a}$$

$$\mathbf{S}^{T}_{0,2^{n+1}} = \mathbf{S}^{T}_{2^{n},2^{n+1}} + \mathbf{t}_{n}\mathbf{q}_{n}(\mathbf{S}^{T}_{0,2^{n}} + \mathbf{R}_{n}\mathbf{S}^{R}_{2^{n},2^{n+1}}), \tag{5.7b}$$

in which $\mathbf{t}_n$, $\mathbf{q}_n$, and $\mathbf{R}_n$ are the matrices at optical thickness $2^n\Delta\tau$, and $\Delta\tau$ is the optical thickness where the single-scattering approximation and homogeneous source approximation are applied. In other words, $\Delta\tau$ is small enough so the multiple scattering matrices in the thin layer with optical thickness $\Delta\tau$ can be computed by the first order scattering, and the variation of temperature in the thin layer is ignored. The subscript "$0,2^n$" indicates that the quantity is for the layer with the upper boundary at optical thickness 0 and lower boundary at optical thickness $2^n\Delta\tau$. The subscript "$2^n,2^{n+1}$" indicates that the quantity is for the layer with the upper boundary at optical thickness $2^n\Delta\tau$ and lower boundary at optical thickness $2^{n+1}\Delta\tau$.

We first discuss the general case where the source can be written as the product of two decoupled parts. One is only dependent on the optical thickness, and the other is only dependent on the zenith angle (Wiscombe 1976). Assuming the source vector (e.g. the thermal source and solar source in Eq. (4.33)) can be written as

$$\Pi = \mathbf{N}(\mu)\mathbf{s}(\tau), \tag{5.8}$$

where Π is the source vector, matrix $\mathbf{N}(\mu)$ only depends on the zenith angle, and vector $\mathbf{s}(\tau)$ only depends on optical thickness. The thermal emission vector of a thin layer with optical thickness $\Delta\tau$ can be expressed as

$$\mathbf{S}_{i,i+1}^{R,T} = \Xi_{in}^{R,T}\mathbf{s}_i, \tag{5.9}$$

in which the subscript "*i*,*i*+1" indicates that the quantity is for a layer with the upper boundary at optical thickness $2^i\Delta\tau$ and lower boundary at optical thickness $2^{i+1}\Delta\tau$. The vector $\mathbf{s}_i$ is defined as the average of $\mathbf{s}(\tau)$ in a thin layer with optical thickness $\Delta\tau$,

$$\mathbf{s}_i = \frac{1}{\Delta\tau}\int_{i\Delta\tau}^{(i+1)\Delta\tau}\mathbf{s}(\tau)d\tau. \tag{5.10}$$

The matrix $\Xi_{in}^{R,T}$ can be expressed as

$$\Xi_{in}^{R,T} = A_+\mathbf{N}(\pm\mu) + A_-\mathbf{N}(\mp\mu), \tag{5.11}$$

where A_+ and A_- are constants to be determined, "$+\mu$" and "*R*" indicate the upward direction, and "$-\mu$" and "*T*" indicate the downward direction. Substituting Eqs. (5.9) into Eq. (5.7), we get,

$$\mathbf{S}_{i,i+2}^{R} = \mathbf{S}_{i,i+1}^{R} + \mathbf{t}_0\mathbf{q}_0(\mathbf{S}_{i+1,i+2}^{R} + \mathbf{R}_0\mathbf{S}_{i,i+1}^{T}) = \left(\Xi_{in}^{R} + \mathbf{t}_0\mathbf{q}_0\mathbf{R}_0\Xi_{in}^{T}\right)\mathbf{s}_i + \mathbf{t}_0\mathbf{q}_0\Xi_{in}^{R}\mathbf{s}_{i+1}, \tag{5.12a}$$

$$\mathbf{S}_{i,i+2}^{T} = \mathbf{S}_{i+1,i+2}^{T} + \mathbf{t}_0\mathbf{q}_0(\mathbf{S}_{i,i+1}^{T} + \mathbf{R}_0\mathbf{S}_{i+1,i+2}^{R}) = \mathbf{t}_0\mathbf{q}_0\Xi_{in}^{T}\mathbf{s}_i + \left(\Xi_{in}^{T} + \mathbf{t}_0\mathbf{q}_0\mathbf{R}_0\Xi_{in}^{R}\right)\mathbf{s}_{i+1}. \tag{5.12b}$$

Then, we define

$$\mathbf{V}_{1,1}^{R} = \Xi_{in}^{R} + \mathbf{t}_0\mathbf{q}_0\mathbf{R}_0\Xi_{in}^{T}, \ \mathbf{V}_{2,1}^{R} = \mathbf{t}_0\mathbf{q}_0\Xi_{in}^{R}, \tag{5.13a}$$

$$\mathbf{V}_{1,1}^{T} = \mathbf{t}_0\mathbf{q}_0\Xi_{in}^{T}, \ \mathbf{V}_{2,1}^{T} = \Xi_{in}^{T} + \mathbf{t}_0\mathbf{q}_0\mathbf{R}_0\Xi_{in}^{R}. \tag{5.13b}$$

Thus, Eq. (5.12) can be written as

$$\mathbf{S}_{i,i+2}^{R} = \mathbf{V}_{1,1}^{R}\mathbf{s}_i + \mathbf{V}_{2,1}^{R}\mathbf{s}_{i+1}, \tag{5.14a}$$

$$\mathbf{S}_{i,i+2}^{T} = \mathbf{V}_{1,1}^{T}\mathbf{s}_i + \mathbf{V}_{2,1}^{T}\mathbf{s}_{i+1}. \tag{5.14b}$$

Note that Eq. (5.14) is still an adding process. Carrying out the adding process one step further, we get

$$\mathbf{S}_{i,i+4}^{R} = \mathbf{V}_{1,2}^{R}\mathbf{s}_i + \mathbf{V}_{2,2}^{R}\mathbf{s}_{i+1} + \mathbf{V}_{3,2}^{R}\mathbf{s}_{i+2} + \mathbf{V}_{4,2}^{R}\mathbf{s}_{i+3}, \tag{5.15a}$$

$$\mathbf{S}_{i,i+4}^{T} = \mathbf{V}_{1,2}^{T}\mathbf{s}_i + \mathbf{V}_{2,2}^{T}\mathbf{s}_{i+1} + \mathbf{V}_{3,2}^{T}\mathbf{s}_{i+2} + \mathbf{V}_{4,2}^{T}\mathbf{s}_{i+3}. \tag{5.15b}$$

By observing Eqs. (5.14) and (5.15), we obtain two general equations inductively,

$$\mathbf{S}_{i,i+2^n}^{R} = \sum_{k=1}^{2^n} \mathbf{V}_{k,n}^{R}\mathbf{s}_{i+k-1}, \tag{5.16a}$$

$$\mathbf{S}_{i,i+2^n}^{T} = \sum_{k=1}^{2^n} \mathbf{V}_{k,n}^{T}\mathbf{s}_{i+k-1}. \tag{5.16b}$$

The $\mathbf{V}^{R,T}$ matrices at iteration n are determined by $\mathbf{V}$ at n-1. Assigning i in Eq. (5.16) to be 0 and 2^n, we obtain

$$\mathbf{S}_{0,2^n}^{R} = \sum_{k=1}^{2^n} \mathbf{V}_{k,n}^{R}\mathbf{s}_{k-1}, \ \mathbf{S}_{2^n,2^{n+1}}^{R} = \sum_{k=1}^{2^n} \mathbf{V}_{k,n}^{R}\mathbf{s}_{2^n+k-1}, \tag{5.17a}$$

$$\mathbf{S}_{0,2^n}^{T} = \sum_{k=1}^{2^n} \mathbf{V}_{k,n}^{T}\mathbf{s}_{k-1}, \ \mathbf{S}_{2^n,2^{n+1}}^{T} = \sum_{k=1}^{2^n} \mathbf{V}_{k,n}^{T}\mathbf{s}_{2^n+k-1}, \tag{5.17b}$$

which suggests that $\mathbf{S}_{0,2^n}^{R,T}$ and $\mathbf{S}_{2^n,2^{n+1}}^{R,T}$ have common terms $\mathbf{V}_{k,n}^{R,T}$. This provides the clue to convert Eq. (5.7) into a doubling process.

We have to know the temperatures at all height in the layer to compute thermal emission accurately, which, however, is usually unknown in the real atmosphere. Instead, we assume that layer top and bottom temperatures are known. Assuming that in a scattering layer, the Planck function is linear with optical thickness, we have

$$\Pi = \mathbf{N}(\mu)\mathbf{s}(\tau), \tag{5.18a}$$

$$\mathbf{N}(\mu) = (1-\varpi)\mathbf{1}, \tag{5.18b}$$

$$\mathbf{s}(\tau) = \left(B_0 + B'\tau\right)\begin{pmatrix} 1 & 0 & 0 & 0 \end{pmatrix}^{\mathrm{T}}, 0 \le \tau \le b, \tag{5.18c}$$

where b is the total optical thickness of a homogeneous layer. B_0 and B' are defined as

$$B_0 = B\left[T(0)\right], \tag{5.19a}$$

$$B_N = B\left[T(b)\right], \tag{5.19b}$$

$$B' = \frac{B_N - B_0}{b}. \tag{5.19c}$$

Substituting Eq. (5.18c) into Eq. (5.10), we obtain

$$\begin{aligned} \mathbf{s}_i &= \frac{1}{\Delta\tau}\int_{i\Delta\tau}^{(i+1)\Delta\tau}\left(B_0 + B'\tau\right)d\tau\begin{pmatrix} 1 & 0 & 0 & 0 \end{pmatrix}^{\mathrm{T}} \\ &= \left[B_0 + \frac{1}{2}B'(2i+1)\Delta\tau\right]\begin{pmatrix} 1 & 0 & 0 & 0 \end{pmatrix}^{\mathrm{T}} \end{aligned}. \tag{5.20}$$

For $i=k-1$ and 2^n+k-1 in Eq. (5.20), we have

$$\mathbf{s}_{k-1} = \left\{B_0 + \frac{1}{2}B'\left[2(k-1)+1\right]\Delta\tau\right\}\begin{pmatrix} 1 & 0 & 0 & 0 \end{pmatrix}^{\mathrm{T}}, \tag{5.21a}$$

$$\mathbf{s}_{2^n+k-1} = \left\{ B_0 + \frac{1}{2} B' \left[2(k-1)+1 \right] \Delta\tau + 2^n B' \Delta\tau \right\} \begin{pmatrix} 1 & 0 & 0 & 0 \end{pmatrix}^{\mathrm{T}}. \tag{5.21b}$$

Substituting Eq. (5.21) into Eq. (5.17), we obtain

$$\mathbf{S}^{R,T}_{2^n,2^{n+1}} = \sum_{k=1}^{2^n} \mathbf{V}^{R,T}_{k,n} \mathbf{s}_{2^n+k-1} = \mathbf{S}^{R,T}_{0,2^n} + 2^n B' \Delta\tau \sum_{k=1}^{2^n} \mathbf{V}^{R,T}_{k,n} \begin{pmatrix} 1 & 0 & 0 & 0 \end{pmatrix}^{\mathrm{T}}. \tag{5.22}$$

The relation between $\mathbf{S}^{R,T}_{0,2^n}$ and $\mathbf{S}^{R,T}_{2^n,2^{n+1}}$ is explicitly established by Eq. (5.22). We define the summation on the right-hand side of Eq. (5.22) as

$$\mathbf{Y}^{R,T}_n = \sum_{k=1}^{2^n} \mathbf{V}^{R,T}_{k,n} \begin{pmatrix} 1 & 0 & 0 & 0 \end{pmatrix}^{\mathrm{T}}. \tag{5.23}$$

By comparing with Eq. (5.17), it can be seen that $\mathbf{Y}^{R,T}_n$ is the source vector that is homogeneous in optical thickness, because its ***s*** vector is $\begin{pmatrix} 1 & 0 & 0 & 0 \end{pmatrix}^{\mathrm{T}}$, which is independent of the optical thickness.

Now we can use the doubling rule to compute the **Y** vector as follows:

$$\mathbf{Y}^{R}_{n+1} = \mathbf{Y}^{R}_{n} + \mathbf{t}_n \mathbf{q}_n (\mathbf{Y}^{R}_{n} + \mathbf{R}_n \mathbf{Y}^{T}_{n}), \tag{5.24a}$$

$$\mathbf{Y}^{T}_{n+1} = \mathbf{Y}^{T}_{n} + \mathbf{t}_n \mathbf{q}_n (\mathbf{Y}^{T}_{n} + \mathbf{R}_n \mathbf{Y}^{R}_{n}). \tag{5.24b}$$

According to Eqs. (5.8)-(5.11) and Eq. (5.18), the **Y** vector in a thin layer with optical thickness $\Delta\tau$ is

$$\mathbf{Y}^{R,T}_0 = (1-\varpi)(A_+ + A_-) \begin{pmatrix} 1 & 0 & 0 & 0 \end{pmatrix}^{\mathrm{T}}, \tag{5.25}$$

which implies that **Y** vectors are identical in the upward and downward directions at the iteration order *n*=0. It can be deduced from Eq. (5.24) that upward and downward **Y** vectors are identical at all iteration orders. Thus Eq. (5.24) can be simplified to

$$\mathbf{Y}_{n+1} = \mathbf{Y}_n + \mathbf{t}_n\mathbf{q}_n(\mathbf{Y}_n + \mathbf{R}_n\mathbf{Y}_n) = \left[\mathbf{1} + \mathbf{t}_n\mathbf{q}_n(\mathbf{1} + \mathbf{R}_n)\right]\mathbf{Y}_n, \tag{5.26}$$

which is the doubling rule of the **Y** vector.

Substituting Eq. (5.22) into Eq. (5.7), we obtain

$$\mathbf{S}^R_{0,2^{n+1}} = \mathbf{S}^R_{0,2^n} + \mathbf{t}_n\mathbf{q}_n(\mathbf{S}^R_{0,2^n} + \mathbf{R}_n\mathbf{S}^T_{0,2^n} + 2^n B'\Delta\tau\mathbf{Y}_n), \tag{5.27a}$$

$$\mathbf{S}^T_{0,2^{n+1}} = \mathbf{S}^T_{0,2^n} + 2^n B'\Delta\tau\mathbf{Y}_n + \mathbf{t}_n\mathbf{q}_n(\mathbf{S}^T_{0,2^n} + \mathbf{R}_n\mathbf{S}^R_{0,2^n} + 2^n B'\Delta\tau\mathbf{R}_n\mathbf{Y}_n). \tag{5.27b}$$

Adding Eqs. (5.27a) and (5,27b), we get

$$\mathbf{S}^T_{0,2^{n+1}} + \mathbf{S}^R_{0,2^{n+1}} = \left[\mathbf{1} + \mathbf{t}_n\mathbf{q}_n\left(\mathbf{1} + \mathbf{R}_n\right)\right]\left(\mathbf{S}^T_{0,2^n} + \mathbf{S}^R_{0,2^n} + 2^n B'\Delta\tau\mathbf{Y}_n\right). \tag{5.28}$$

Subtracting Eq. (5.27a) from Eq. (5.27b), we get

$$\begin{aligned} &\mathbf{S}^T{}_{0,2^{n+1}} - \mathbf{S}^R{}_{0,2^{n+1}} = \mathbf{S}^T{}_{0,2^n} - \mathbf{S}^R{}_{0,2^n} \\ &+2^n B'\Delta\tau\mathbf{Y}_n + \mathbf{t}_n\mathbf{q}_n\left(\mathbf{1} - \mathbf{R}_n\right)\left(\mathbf{S}^T{}_{0,2^n} - \mathbf{S}^R{}_{0,2^n} - 2^n B'\Delta\tau\mathbf{Y}_n\right)\end{aligned}. \tag{5.29}$$

Then, we define

$$\mathbf{W}_n = \left(\mathbf{S}^T_{0,2^n} + \mathbf{S}^R_{0,2^n}\right)/2, \tag{5.30}$$

$$\mathbf{Z}_n = \left(\mathbf{S}^T_{0,2^n} - \mathbf{S}^R_{0,2^n}\right)/2B', \tag{5.31}$$

$$g_n = 2^{n-1}\Delta\tau, \tag{5.32}$$

So Eqs. (5.28) and (5.29) can be written as

$$\mathbf{W}_{n+1} = \left[\mathbf{1} + \mathbf{t}_n\mathbf{q}_n\left(\mathbf{1} + \mathbf{R}_n\right)\right]\left(\mathbf{W}_n + B'g_n\mathbf{Y}_n\right), \tag{5.33}$$

$$\mathbf{Z}_{n+1} = \mathbf{Z}_n + g_n\mathbf{Y}_n + \mathbf{t}_n\mathbf{q}_n\left(\mathbf{1} - \mathbf{R}_n\right)\left(\mathbf{Z}_n - g_n\mathbf{Y}_n\right). \tag{5.34}$$

Assume that $\mathbf{W}_n$ is related to the $\mathbf{Y}$ vector by

$$\mathbf{W}_n = \alpha_n\mathbf{Y}_n. \tag{5.35}$$

When n is 0, it is easy to see from Eq. (5.21a) and Eqs. (5.30)-(5.32),

$$\alpha_0 = B_0 + \frac{1}{2}B'\Delta\tau. \tag{5.36}$$

Substituting Eq. (5.35) into Eq. (5.33), we obtain,

$$\mathbf{W}_{n+1} = \left[\mathbf{1} + \mathbf{t}_n\mathbf{q}_n\left(\mathbf{1} + \mathbf{R}_n\right)\right]\mathbf{Y}_n\left(\alpha_n + B'g_n\right) = \left(\alpha_n + B'g_n\right)\mathbf{Y}_{n+1}, \tag{5.37}$$

so the expression of α_n is

$$\alpha_n = B_0 + B'g_n. \tag{5.38}$$

Now, we can directly obtain the $\mathbf{S}$ vector from the $\mathbf{Y}$ and $\mathbf{Z}$ vectors,

$$\mathbf{S}^T_{0,2^n} = \mathbf{W}_n + B'\mathbf{Z}_n = \left(B_0 + B'g_n\right)\mathbf{Y}_n + B'\mathbf{Z}_n = \frac{1}{2}\left(B_0 + B_n\right)\mathbf{Y}_n + B'\mathbf{Z}_n, \tag{5.39a}$$

$$\mathbf{S}^R_{0,2^n} = \mathbf{W}_n - B'\mathbf{Z}_n = \left(B_0 + B'g_n\right)\mathbf{Y}_n - B'\mathbf{Z}_n = \frac{1}{2}\left(B_0 + B_n\right)\mathbf{Y}_n - B'\mathbf{Z}_n. \tag{5.39b}$$

The $\mathbf{Y}$ and $\mathbf{Z}$ vectors are computed by the doubling rules in Eq. (5.26) and Eq. (5.34). Then, the two thermal emission vectors $\mathbf{S}^T$ and $\mathbf{S}^R$ are directly obtained in Eq. (5.39).

From the definition of the $\mathbf{Z}$ vector, Eq. (5.31), we know that $\mathbf{Z}_0$ is zero, since $\mathbf{S}^T{}_{0,1}$ and $\mathbf{S}^R{}_{0,1}$ are the same for the initial layer with optical thickness $\Delta\tau$. The initial $\mathbf{Y}$ vector ($\mathbf{Y}_0$) can be computed by a single-scattering approximation.

From Eq. (5.18b), the source for the **Y** vector is isotropic. The non-scattering contribution to $\mathbf{Y}_0$ is

$$\begin{aligned}\mathbf{I}_0^T\left(\tau,-\mu\right) &= \left(1-\varpi\right)\begin{pmatrix} 1 & 0 & 0 & 0 \end{pmatrix}^{\mathrm{T}} \int_0^{\tau} \frac{d\tau'}{\mu} \exp\left[-(\tau-\tau')/\mu\right] \\ &= \left(1-\varpi\right)\left(1-e^{-\tau/\mu}\right)\begin{pmatrix} 1 & 0 & 0 & 0 \end{pmatrix}^{\mathrm{T}},\end{aligned} \tag{5.40a}$$

$$\begin{aligned}\mathbf{I}_0^R\left(\tau,\mu\right) &= \left(1-\varpi\right)\begin{pmatrix} 1 & 0 & 0 & 0 \end{pmatrix}^{\mathrm{T}} \int_{\tau}^{\Delta\tau} \frac{d\tau'}{\mu} \exp\left[-(\tau'-\tau)/\mu\right] \\ &= \left(1-\varpi\right)\left(1-e^{-(\Delta\tau-\tau)/\mu}\right)\begin{pmatrix} 1 & 0 & 0 & 0 \end{pmatrix}^{\mathrm{T}}.\end{aligned} \tag{5.40b}$$

Using the SOS method (Hovenier et al. 2004), the single-scattering source $\mathbf{J}_1$ is written as

$$\begin{aligned}\mathbf{J}_1 &= \frac{\varpi}{4\pi}\int_0^1 d\mu' \int_0^{2\pi} d\phi' \left[\mathbf{P}(\mu,\mu',\phi-\phi')\mathbf{I}_0^T + \mathbf{P}(\mu,-\mu',\phi-\phi')\mathbf{I}_0^R\right] \\ &= \frac{\varpi(1-\varpi)}{2}\begin{pmatrix} 1 & 0 & 0 & 0 \end{pmatrix}^{\mathrm{T}} \\ &\cdot\left[\int_0^1 d\mu' \mathbf{P}(\mu,\mu')\left(1-e^{-\tau/\mu'}\right) + \int_0^1 d\mu' \mathbf{P}(\mu,-\mu')\left(1-e^{-(b-\tau)/\mu'}\right)\right].\end{aligned} \tag{5.41}$$

The single-scattering term is computed from the single-scattering source, Eq. (5.41),

$$\begin{aligned}\mathbf{I}_1 &= \int_0^{\Delta\tau} \frac{d\tau'}{\mu} \mathbf{J}_1 \exp\left[-\frac{\tau-\tau'}{\mu}\right] \\ &= \frac{\varpi(1-\varpi)}{2}\begin{pmatrix} 1 & 0 & 0 & 0 \end{pmatrix}^{\mathrm{T}} \\ &\cdot\left\{\int_0^1 \mathbf{P}\left(\mu,\mu'\right)\left[1-e^{-\frac{\Delta\tau}{\mu}} + \frac{\mu'}{\mu-\mu'}\left(e^{-\frac{\Delta\tau}{\mu'}} - e^{-\frac{\Delta\tau}{\mu}}\right)\right] d\mu' \right. \\ &\left. + \int_0^1 \mathbf{P}\left(\mu,-\mu'\right)\left[1-e^{-\frac{\Delta\tau}{\mu}} - \frac{\mu'}{\mu+\mu'}\left(1-e^{-\Delta\tau(\frac{1}{\mu}+\frac{1}{\mu'})}\right)\right] d\mu' \right\},\end{aligned} \tag{5.42}$$

With some manipulation, Eq. (5.42) can be written as

$$\begin{aligned}\mathbf{I}_1 = \begin{pmatrix} 1 & 0 & 0 & 0 \end{pmatrix}^{\mathrm{T}} \Bigg\{ & \varpi(1-\varpi)\left(1-e^{-\frac{\Delta\tau}{\mu}}\right)\int_0^1 \left[\mathbf{P}(\mu,-\mu')+\mathbf{P}(\mu,\mu')\right] d\mu' \\ & -2(1-\varpi)\int_0^1 \mu'\left[\mathbf{T}_1(\mu,\mu')+\mathbf{R}_1(\mu,\mu')\right] d\mu' \Bigg\},\end{aligned} \tag{5.43}$$

in which $\mathbf{R}_1$ and $\mathbf{T}_1$ are the first order reflection transmission matrices defined as

$$\mathbf{R}_1(\mu,\mu') = \frac{\varpi}{4(\mu'+\mu)}\left[1-e^{-\Delta\tau\left(\frac{1}{\mu'}+\frac{1}{\mu}\right)}\right]\mathbf{P}(-\mu,\mu'), \tag{5.44a}$$

$$\mathbf{T}_1(\mu,\mu') = \frac{\varpi}{4(\mu'-\mu)}\left(e^{-\frac{\Delta\tau}{\mu'}} - e^{-\frac{\Delta\tau}{\mu}}\right)\mathbf{P}(\mu,\mu'). \tag{5.44b}$$

The initial **Y** vector is equal to Eq. (5.43).

5.2 Adding with Surface Emission

In a radiative transfer calculation involving thermal emission, emission from the surface is usually non-negligible. Here we consider the interaction of thermal emissions between the atmosphere and surface.

The general multiple scattering matrices of the atmosphere-surface system are

$$\mathbf{Q}_1 = \mathbf{R}_a^*\mathbf{R}_s, \tag{5.45a}$$

$$\mathbf{Q}_{p+1} = \mathbf{Q}_1\mathbf{Q}_p, \tag{5.45b}$$

$$\mathbf{Q} = \sum_{p=1}^{\infty}\mathbf{Q}_p, \tag{5.45c}$$

$$\mathbf{D} = \mathbf{Q}\mathbf{T}_a + \mathbf{Q}\mathbf{E} + \mathbf{T}_a, \tag{5.45d}$$

$$\mathbf{U} = \mathbf{R}_s\mathbf{D} + \mathbf{R}_s\mathbf{E}, \tag{5.45e}$$

$$\mathbf{R} = \mathbf{R}_a + \mathbf{T}_a^*\mathbf{U} + \mathbf{E}\mathbf{U}, \tag{5.45f}$$

where subscript "*s*" denotes the quantities for the surface, and subscript "*a*" denotes the quantities for the atmosphere. For example, $\mathbf{T}_a$ is the transmission matrix of the atmosphere, and $\mathbf{R}_s$ is the reflection matrix of the surface. For a Lambertian surface with albedo *r*, $\mathbf{R}_s$ is expressed as,

$$\mathbf{R}_s\left(\mu,\mu_0,\varphi-\varphi_0\right) = \begin{pmatrix} r & 0 & 0 & 0 \\ 0 & 0 & 0 & 0 \\ 0 & 0 & 0 & 0 \\ 0 & 0 & 0 & 0 \end{pmatrix}. \tag{5.46}$$

Based on the multiple scattering matrices, Eq. (5.45), the thermal emission vectors are derived as follows:

$$\mathbf{S}^D = \left(\mathbf{1} + \mathbf{Q}\right)\left(\mathbf{S}_a^T + \mathbf{R}_a^*\mathbf{S}_s\right), \tag{5.47a}$$

$$\mathbf{S}^U = \mathbf{S}_s + \mathbf{R}_s\mathbf{S}^D, \tag{5.47b}$$

$$\mathbf{S}_R = \mathbf{S}_a^R + \left(\mathbf{E} + \mathbf{T}_a^*\right)\mathbf{S}^U, \tag{5.47c}$$

where $\mathbf{S}^U$ and $\mathbf{S}^D$ are the upward and downward thermal emissions at the surface-atmosphere interface, $\mathbf{S}_R$ is the thermal emission by the surface-atmosphere system, and $\mathbf{S}_s$ is the thermal emission vector by the surface. If the surface emits radiation isotropically, $\mathbf{S}_s$ is expressed as,

$$\mathbf{S}_s(\mu) = \begin{pmatrix} \varepsilon_s B(T_s) \\ 0 \\ 0 \\ 0 \end{pmatrix}, \tag{5.48}$$

where T_s is the surface temperature, and ε_s is the surface emissivity.

5.3 Adding with a Non-scattering Layer

In a practical application, the thermal emission calculation usually involves only gas absorption in one of the two layers. In this case, there is no repeated reflection between the two layers, and thus the adding calculation can be simplified.

In a calculation of adding thermal emissions from two layers, the upper layer only has gas absorption, and the lower layer has multiple scattering. Thermal emission by the atmospheric gas layer has been computed by Eq. (3.1). The thermal emission by the lower scattering layer has been computed by the doubling approach. We need to know the total thermal emission by the two layers. The adding equations are as follows:

$$\mathbf{S}^D = \mathbf{S}^{uT}, \tag{5.49a}$$

$$\mathbf{S}^U = \mathbf{S}^{lR} + \mathbf{R}^l \mathbf{S}^D, \tag{5.49b}$$

$$\mathbf{S}^R = \mathbf{S}^{uR} + \mathbf{E}(\tau^u)\mathbf{S}^U = \mathbf{S}^{uR} + \mathbf{E}(\tau^u)\left(\mathbf{S}^{lR} + \mathbf{R}^l \mathbf{S}^{uT}\right), \tag{5.49c}$$

$$\mathbf{S}^T = \mathbf{S}^{lT} + \mathbf{E}(\tau^l)\mathbf{S}^D + \mathbf{T}^l \mathbf{S}^D = \mathbf{S}^{lT} + \left(\mathbf{E}(\tau^l) + \mathbf{T}^l\right)\mathbf{S}^{uT}. \tag{5.49d}$$

If the upper layer has multiple scattering, and the lower layer only has gas absorption, the adding equations are as follow:

$$\mathbf{S}^D = \mathbf{S}^{uT} + \mathbf{R}^u \mathbf{S}^{lR}, \tag{5.50a}$$

$$\mathbf{S}^{U}=\mathbf{S}^{lR}, \tag{5.50b}$$

$$\mathbf{S}^{R}=\mathbf{S}^{uR}+\mathbf{E}(\tau^{u})\mathbf{S}^{U}+\mathbf{T}^{u}\mathbf{S}^{U}=\mathbf{S}^{uR}+\left(\mathbf{E}(\tau^{u})+\mathbf{T}^{u}\right)\mathbf{S}^{lR}, \tag{5.50c}$$

$$\mathbf{S}^{T}=\mathbf{S}^{lT}+\mathbf{E}(\tau^{l})\mathbf{S}^{D}=\mathbf{S}^{lT}+\mathbf{E}(\tau^{l})\left(\mathbf{S}^{uT}+\mathbf{R}^{u}\mathbf{S}^{lR}\right). \tag{5.50d}$$

5.4 Validation

We use the Discrete Ordinate Radiative Transfer (DISORT) model developed by Stamnes et al. (1988) to validate the adding-doubling thermal emission calculation approach. In the validation, the model atmosphere has an ice cloud layer above a Lambertian surface with albedo 0.3. The surface temperature is set to 288 K. The cloud top and bottom temperatures are 255 K and 260 K respectively. The ice cloud has effective radius 30 μm. The MODIS Collection 6 model is used as the ice cloud model. The wavelength is 3.8 μm in the simulation. Figs. 22 and 23 show the upward TOA thermal emission and downward thermal emission at the surface simulated by the adding-doubling approach and DISORT. The radiance is converted to brightness temperature in Figs. 22 and 23.

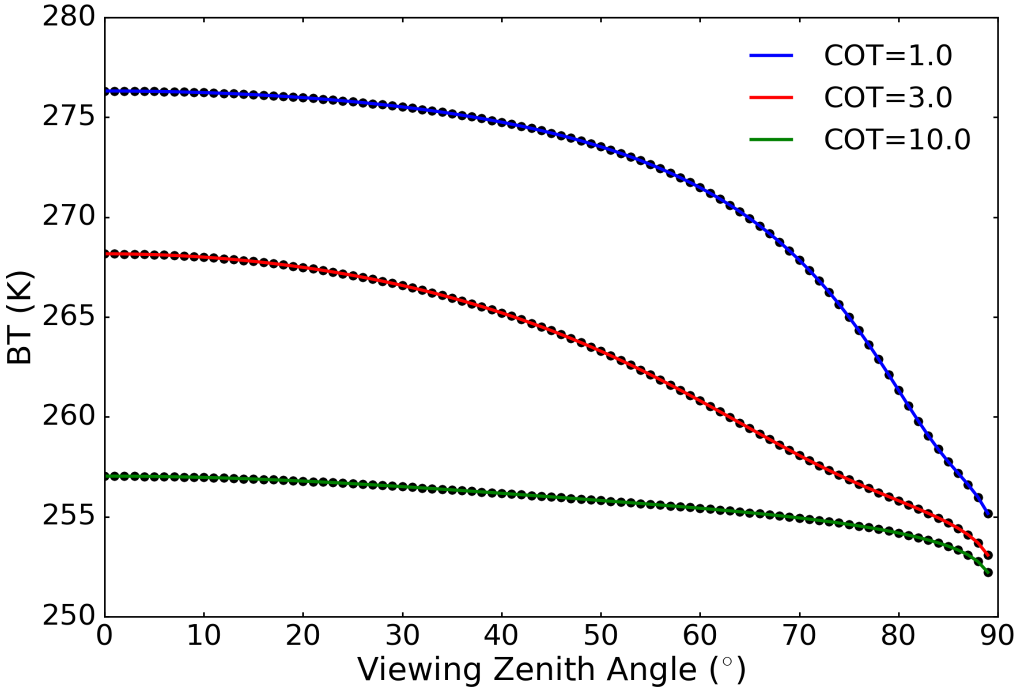

Figure 22 TOA thermal emission at 3.8 μm simulated by adding-doubling and DISORT. The model atmosphere has an ice cloud layer with varied cloud optical thicknesses (COT=1.0, 3.0, or 10.0) and effective radius 30 μm. Cloud top and bottom temperatures are 255 K and 260 K respectively. A Lambertian surface with temperature 288 K and emissivity 0.3 is assumed in the simulation. **Solid lines:** adding-doubling; **Dots:** DISORT.

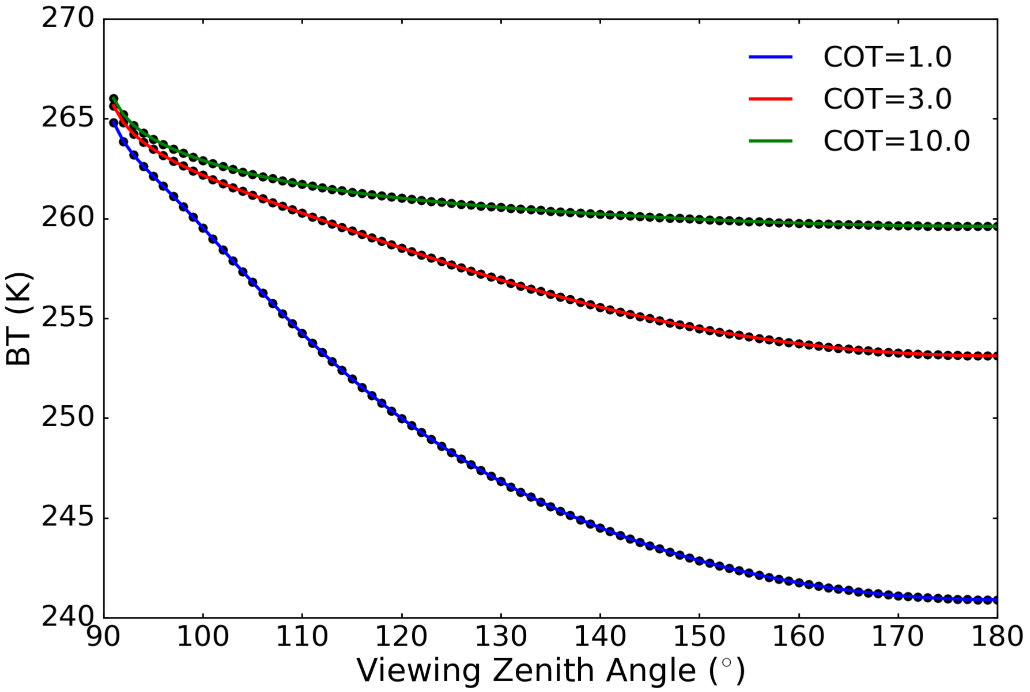

Figure 23 Surface downward thermal emission at 3.8 μm simulated by adding-doubling and DISORT. The model atmosphere has an ice cloud layer with varied cloud optical thicknesses (COT=1.0, 3.0, or 10.0) and effective radius 30 μm. Cloud top and bottom temperatures are 255 K and 260 K respectively. A Lambert surface with temperature 288 K and emissivity 0.3 is assumed in the simulation**. Solid lines:** adding-doubling; **Dots:** DISORT.

Three different cloud optical thicknesses (COTs) are assumed in the simulation. The adding-doubling and DISORT results are consistent in all cases to at least four decimal places. As shown in Fig. 22, for larger COT, the TOA emission is smaller, which suggests a cloud radiative cooling effect at the TOA. In contrast, as shown in Fig. 23, a larger COT makes the downward surface emission increase, which suggests a cloud radiative warming effect at the surface. Because DISORT is a scalar RTM, polarization is not considered in the validation, although the adding-doubling approach is able to consider polarization of thermal emission.

CHAPTER VI

AIR-SEA INTERFACE AND OCEAN MODEL

6.1 Air-Sea Interface

Because the atmosphere and ocean have different refractive indices, radiation traveling through the air-sea interface will experience refraction and reflection. The optical properties of the ocean are determined by the morphology of the ocean surface and the properties of the ocean water. We first consider the general case where the optical properties of the interface are expressed by a reflection matrix and a transmission matrix in the adding-doubling scheme.

In the adding-doubling scheme, the multiple scattering matrices of an atmosphere-ocean system are computed as follows:

$$\mathbf{Q}_1 = \mathbf{R}_a^* \left(\mathbf{T}_{\text{int}}^* \mathbf{R}_o \mathbf{T}_{\text{int}} + \mathbf{R}_{\text{int}} \right), \tag{6.1a}$$

$$\mathbf{Q}_{p+1} = \mathbf{Q}_1 \mathbf{Q}_p, \tag{6.1b}$$

$$\mathbf{Q} = \sum_{p=1}^{\infty} \mathbf{Q}_p, \tag{6.1c}$$

$$\mathbf{D}_{ai} = \mathbf{T}_a + \mathbf{Q}\left(\mathbf{E}(\tau_a) + \mathbf{T}_a \right), \tag{6.1d}$$

$$\mathbf{U}_{ai} = \left(\mathbf{R}_{\text{int}} + \mathbf{T}_{\text{int}}^* \mathbf{R}_o \mathbf{T}_{\text{int}} \right)\left(\mathbf{D}_{ai} + \mathbf{E}(\tau_a) \right), \tag{6.1e}$$

$$\mathbf{D}_{oi} = \left(\mathbf{T}_{\text{int}} + \mathbf{R}_{\text{int}}^* \mathbf{R}_o \mathbf{T}_{\text{int}} \right)\left(\mathbf{D}_{ai} + \mathbf{E}(\tau_a) \right), \tag{6.1f}$$

$$\mathbf{U}_{oi} = \mathbf{R}_o \mathbf{T}_{\text{int}} \mathbf{E}(\tau_a) + \mathbf{R}_o \mathbf{D}_{oi}, \tag{6.1g}$$

$$\mathbf{R}_{ao} = \mathbf{R}_a + \left(\mathbf{E}(\tau_a) + \mathbf{T}_a^*\right)\mathbf{U}_{ai}, \tag{6.1h}$$

$$\mathbf{T}_{ao} = \mathbf{E}(\tau_o)\mathbf{D}_{oi} + \mathbf{T}_o\left(\mathbf{D}_{oi} + \mathbf{T}_{\text{int}}\mathbf{E}(\tau_a)\right), \tag{6.1i}$$

where subscripts "*a*" and "*o*" denote atmosphere and ocean respectively, and subscript "int" denotes the interface. $\mathbf{R}_{\text{int}}$ and $\mathbf{T}_{\text{int}}$ are reflection and transmission matrices of the interface when the radiation is incident from air to water (air-incident case). $\mathbf{R}_{\text{int}}^*$ and $\mathbf{T}_{\text{int}}^*$ are reflection and transmission matrices of the interface when the radiation is incident from water to air (water-incident case). $\mathbf{U}_{ai}$ and $\mathbf{D}_{ai}$ are upward and downward matrices just above the interface at the bottom of the atmosphere. $\mathbf{U}_{oi}$ and $\mathbf{D}_{oi}$ are upward and downward matrices just below the interface at the top of the ocean. $\mathbf{R}_{ao}$ is the reflection matrix of the atmosphere-ocean system at the TOA. $\mathbf{T}_{ao}$ is the transmission matrix of the atmosphere-ocean system at the ocean bottom. τ_o is the optical thickness of the ocean.

In the formulation Eq. (6.1), the ocean bottom is assumed to be completely absorptive so there is no reflection by the ocean bottom. Unlike a scattering layer, there is no repeated reflection between the interface and atmosphere or ocean layers. Note that all the matrices in Eq. (6.1) are Fourier components of the corresponding matrices.

6.1.1 Rough Surface Model

The explicit expressions of the reflection and transmission matrices of the interface are given below. Here we assume the ocean surface is a wind-ruffled rough surface. The surface model is a collection of tilted facets whose normal directions are randomly oriented. The distribution of the facets' normal directions follows the Cox-Munk model (Cox and Munk 1954).

If the wind direction is assumed isotropic, the probability density of a facet's orientation is expressed as

$$\frac{dS}{S} = p(s_x, s_y) ds_x ds_y , \tag{6.2}$$

where s_x and s_y are the slope vector components of the facet. $p(s_x, s_y)$ is the probability density function of the slope distribution. *dS* is the horizontal projection area of the facets that have the slope vector (ds_x, ds_y). *S* is the horizontal projection area of all facets. $p(s_x, s_y)$ is defined as

$$p(s_x, s_y) = \frac{1}{\pi\sigma^2} \exp\left(-\frac{s_x^2 + s_y^2}{\sigma^2} \right), \tag{6.3}$$

in which the variance σ^2 is a function of the wind speed at 41 feet above sea level (Cox and Munk 1954),

$$\sigma^2 = 0.003 + 0.00512W , \tag{6.4}$$

where *W* is the wind speed with unit m/s.

The slope vector components s_x and s_y are defined as

$$s_x = \frac{\partial z}{\partial x} = \tan\theta_f \cos\varphi_f , \tag{6.5a}$$

$$s_y = \frac{\partial z}{\partial y} = \tan\theta_f \sin\varphi_f , \tag{6.5b}$$

where θ_f and φ_f are facet tilting zenith and azimuth angles. The geometry of the tilted facet and angles in Eq. (6.5) are shown in Fig. 24.

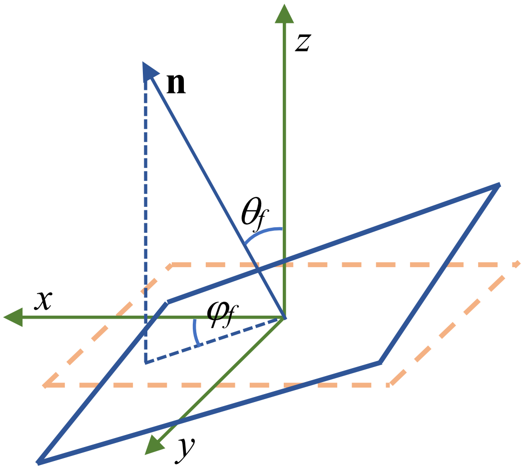

Figure 24 The geometry of a tilted facet of the ocean surface model. *x*, *y* and *z* are relative coordinate axes, where the *x*-*y* plane is horizontal and z is vertical. θ_f and φ_f are facet tilting zenith and azimuth angles respectively. **n** is the normal direction of the tilted facet.

Substituting Eq. (6.3) and Eq. (6.5) into Eq. (6.2), we obtain

$$\frac{dS}{S} = \frac{1}{\pi\sigma^2\mu_f^3}\exp\left(-\frac{1-\mu_f^2}{\sigma^2\mu_f^2}\right)\sin\theta_f d\theta_f d\varphi_f\,, \tag{6.6}$$

where $\mu_f = \cos\theta_f$. Eq. (6.6) is consistent with the description of the Cox-Munk model for a rough ocean surface in Lenoble et al. (2007) and Zhai et al. (2010). Note that Eq. (6.6) is only a function of tilting zenith angle θ_f. The right-most three terms in Eq. (6.6) constitute a differential solid angle term $d\Omega_f \equiv \sin\theta_f d\theta_f d\varphi_f$ around the facet's normal direction.

6.1.2 Reflection Matrix

Fig. 25 illustrates the reflection geometry by the rough sea surface in the air-incident case. Since the orientation distribution of the facets is uniform in the azimuthal direction, only a 2D plot is shown in Fig. 25. On a real ocean surface, the reflection direction is determined by the incidence direction and the local normal direction of the incident location. In our ocean surface model, incidence and reflection directions determine the local normal direction.

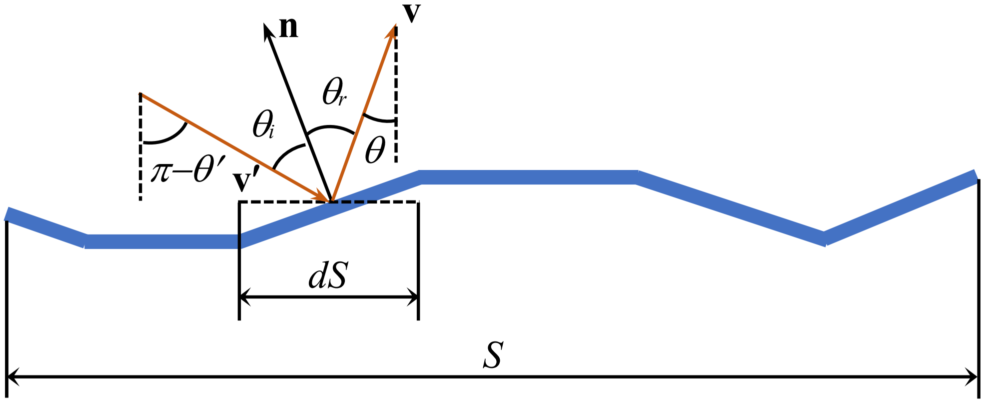

Figure 25 An illustration of reflection by the rough sea surface in the air-incident case. **n** is the local normal direction. **v**′ and **v** are direction vectors of incident and reflected radiation, respectively. θ' and θ are incident and outgoing zenith angles. θ_i and θ_r are local incidence and reflection angles. *dS* is the area of a facet's horizontal projection. *S* is the area of all facets' horizontal projection.

The incidence (**v**′) and reflection (**v**) direction vectors are

$$\mathbf{v}' = \left(\sin\theta'\cos\varphi', \quad \sin\theta'\sin\varphi', \quad \cos\theta' \right), \tag{6.7a}$$

$$\mathbf{v} = \left(\sin\theta\cos\varphi, \quad \sin\theta\sin\varphi, \quad \cos\theta \right). \tag{6.7b}$$

where θ' and φ' are incident zenith angle and azimuth angles, and θ and φ are outgoing zenith angle and azimuth angles.

Based on Snell's law, the local normal vector **n** can be expressed by

$$\mathbf{n} = \frac{\mathbf{v} - \mathbf{v}'}{\left|\mathbf{v} - \mathbf{v}'\right|}. \tag{6.8}$$

The angle between the local normal and incident direction is the local incident angle θ_i, and the angle between the local normal and reflection direction is the local reflection angle θ_r. θ_i and θ_r are obtained by

$$\theta_i = \arccos\left(-\mathbf{n} \cdot \mathbf{v}'\right) = \frac{\pi - \Theta}{2}, \tag{6.9a}$$

$$\theta_r = \arccos\left(\mathbf{n} \cdot \mathbf{v}\right) = \frac{\pi - \Theta}{2}, \tag{6.9b}$$

where Θ is the scattering angle, $\arccos(\mathbf{v} \cdot \mathbf{v}')$, which is consistent with the definition in Eq. (4.4). Using Eqs. (6.7) and (6.8), μ_f in Eq. (6.6) can be obtained by

$$\mu_f = \frac{\cos\theta - \cos\theta'}{\sqrt{2 - 2\cos\Theta}}. \tag{6.10}$$

Using the local incidence, reflection and tilting angles obtained above, we can derive the reflection matrix of the rough ocean surface with specified incident and outgoing directions in the air-incident case as follows.

First, let us consider the scalar case where polarization is ignored. If the incident flux immediately above the ocean surface is F_0, the incident radiation (with the unit of power here) on the facet with area dS is

$$\psi_i = F_o \cos\theta_i \frac{dS}{\mu_f}. \tag{6.11}$$

The radiation reflected from the facet is

$$\psi_r = F_o \cos\theta_i \frac{dS}{\mu_f} \tilde{r}(\theta_i) \xi\left(\mu, \mu', \sigma\right), \tag{6.12}$$

where $\tilde{r}(\theta_i)$ is the power reflection coefficient at incident angle θ_i. $\xi\left(\mu, \mu'\right)$ is the shadowing function (Smith 1967; Sancer 1969) that considers the incident and reflected radiation to be partially blocked by the rough surface. The shadowing function term in Eq. (6.12) computes the reflected radiation ψ_r a statistically averaged quantity. If the surface normal direction distribution is described by Eq. (6.6), $\xi\left(\mu, \mu'\right)$ can be explicitly expressed as (Sancer 1969)

$$\xi\left(\mu, \mu'\right) = \frac{1}{1 + \Lambda(\mu) + \Lambda(\mu')}, \tag{6.13}$$

where $\Lambda(\mu)$ is

$$\Lambda(\mu) = \frac{1}{2} \left\{ \sqrt{\frac{\sigma^2 (1-\mu^2)}{\pi \mu^2}} \exp\left[-\frac{\mu^2}{\sigma^2 (1-\mu^2)} \right] - \operatorname{erfc}\left(\frac{\mu}{\sigma \sqrt{1-\mu^2}} \right) \right\}, \tag{6.14}$$

in which erfc is the complementary error function.

If the ocean surface with area *S* is viewed as a whole, the reflected radiation in the **v** direction is expressed as

$$\psi_r' = \mu I\left(\tau_a, \mu, \varphi\right) S d\Omega, \tag{6.15}$$

where $I(\tau_a,\mu,\varphi)$ is the radiance along the **v** direction at the bottom of atmosphere (i.e. immediately above the ocean surface). $d\Omega = \sin\theta d\theta d\varphi$ is the differential solid angle around the reflection direction.

Statistically, Eqs. (6.12) and (6.15) are equal, so we have

$$\begin{aligned} I(\tau_a,\mu,\varphi) &= F_\mathrm{o}\cos\theta_i \frac{dS}{S\mu\mu_f d\Omega}\tilde{r}(\theta_i)\xi(\mu,\mu',\sigma) \\ &= F_\mathrm{o}\cos\theta_i \frac{r(\theta_i)\xi(\mu,\mu',\sigma)}{\pi\sigma^2\mu\mu_f^4}\exp\left(-\frac{1-\mu_f^2}{\sigma^2\mu_f^2}\right)\frac{d\Omega_f}{d\Omega}, \end{aligned} \tag{6.16}$$

where Eq. (6.6) is used. The two differential solid angle terms in Eq. (6.16) can be simplified using the relation between them. The differential terms are unchanged in different Cartesian coordinates. In a Cartesian coordinate with **v**′, and two directions perpendicular to **v**′ and each other as axes, (θ_f,φ_f) and (θ,φ) are

$$\theta_f = \theta_i, \tag{6.17a}$$

$$\varphi_f = \varphi_i, \tag{6.17b}$$

$$\theta = 2\theta_i, \tag{6.17c}$$

$$\varphi = \varphi_i. \tag{6.17d}$$

Thus, $d\Omega_f$ and $d\Omega$ in Eq. (6.16) can be written as

$$d\Omega_f = \sin(\theta_i)\det\frac{\partial(\theta_f,\varphi_f)}{\partial(\theta_i,\varphi_i)} = \sin\theta_i d\theta_i d\varphi_i, \tag{6.18a}$$

$$d\Omega = \sin(2\theta_i)\det\frac{\partial(\theta,\varphi)}{\partial(\theta_i,\varphi_i)} = 4\sin\theta_i\cos\theta_i d\theta_i d\varphi_i, \tag{6.18b}$$

where the ‘det’ terms are the determinants of Jacobian matrices. Substituting Eq. (6.18) into Eq. (6.16), we obtain

$$I\left(\tau_a,\mu,\varphi\right)=F_{\text{o}}\frac{\tilde{r}(\theta_i)\xi\left(\mu,\mu',\sigma\right)}{4\pi\sigma^2\mu\mu_f^4}\exp\left(-\frac{1-\mu_f^2}{\sigma^2\mu_f^2}\right). \tag{6.19}$$

According to the definition of reflectance, Eq. (1.7), the bidirectional reflectance distribution function (BRDF) at the air-sea interface is expressed as

$$R_{\text{int}}\left(\mu,\mu',\varphi-\varphi'\right)\equiv\frac{\pi I\left(\tau_a,-\mu,\varphi\right)}{\mu' F_{\text{o}}}=\frac{\tilde{r}(\theta_i)\xi\left(\mu,\mu',\sigma\right)}{4\sigma^2\mu'\mu\mu_f^4}\exp\left(-\frac{1-\mu_f^2}{\sigma^2\mu_f^2}\right). \tag{6.20}$$

The reflection matrix is obtained by generalizing Eq. (6.20) to consider polarization:

$$\mathbf{R}_{\text{int}}\left(\mu,\mu',\varphi-\varphi'\right)=\frac{\xi\left(\mu,\mu',\sigma\right)}{4\sigma^2\mu'\mu\mu_f^4}\exp\left(-\frac{1-\mu_f^2}{\sigma^2\mu_f^2}\right)\mathbf{L}(\pi-\eta_2)\mathbf{r}_a(\theta_i)\mathbf{L}(-\eta_1), \tag{6.21}$$

in which $\mathbf{r}_a(\theta_i)$ is the Fresnel reflection matrix in the air-incident case. The rotation matrix $\mathbf{L}(-\eta_1)$ rotates the reference plane of the incident Stokes vector from the incident plane to the local reflection plane. $\mathbf{L}(\pi-\eta_2)$ rotates the reference plane of the reflected Stokes vector from the local reflection plane to reflection plane. The incident and zenith directions define the incident plane. The local normal and incident directions define the local reflection plane. The reflection and zenith directions define the reflection plane.

6.1.3 Transmission Matrix

The transmission geometry by the rough sea surface in the air-incident case is illustrated in Fig. 26. The radiation transmitting through the interface experiences refraction. The local refraction angle θ_t is defined as the angle between refraction direction and the local normal direction.

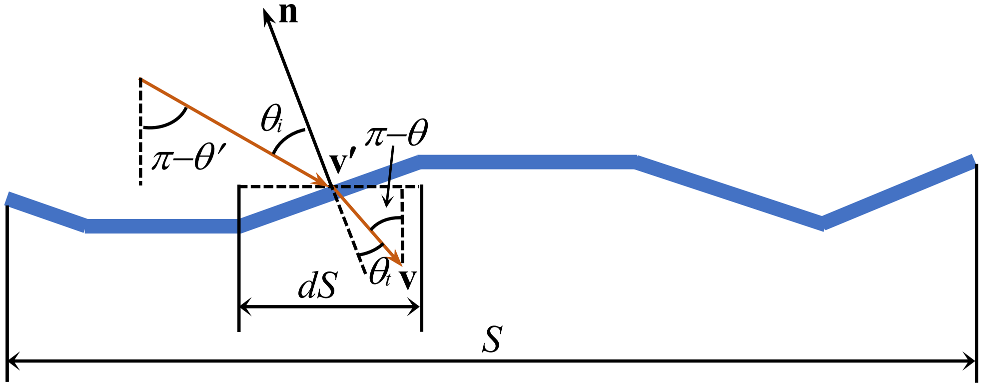

Figure 26 An illustration of transmission through the rough sea surface in the air-incident case. **n** is the local normal direction. **v**′ and **v** are direction vectors of incident and transmitted radiation, respectively. θ' and θ are incident and outgoing zenith angles. θ_i and θ_t are local incidence and refraction angles. *dS* is the area of a facet's horizontal projection. *S* is the area of all facets' horizontal projection.

As in the reflection case, the local normal direction **n** is determined by the incidence direction **v**′ and the refraction direction **v**:

$$\mathbf{n} = \frac{1}{\sin\Theta}\left(\sin\theta_t \mathbf{v}' - \sin\theta_i \mathbf{v}\right), \tag{6.22}$$

where the scattering angle $\Theta = \theta_i - \theta_t$ is equal to $\arccos(\mathbf{v}\cdot\mathbf{v}')$. Using Snell's law $n_a \sin\theta_i = n_o \sin\theta_t$, in which n_a and n_o are real parts of refractive indices in the atmosphere and ocean respectively, θ_i and θ_t are obtained by

$$\theta_i = \arccos\left(\frac{n_o \cos\Theta - n_a}{\sqrt{n_o^2 + n_a^2 - 2n_a n_o \cos\Theta}}\right), \tag{6.23a}$$

$$\theta_t = \arccos\left(\frac{n_o - n_a\cos\Theta}{\sqrt{n_o^2 + n_a^2 - 2n_a n_o \cos\Theta}}\right). \tag{6.23b}$$

μ_f is determined by

$$\mu_f = \frac{\sin\theta_t\mu' - \sin\theta_i\mu}{\sin\Theta}. \tag{6.24}$$

The transmission and reflection matrices are derived in an analogous way. The incident radiation is given in Eq. (6.11). The transmitted radiation through the facet is

$$\psi_t = F_o\cos\theta_i \frac{dS}{\mu_f}\tilde{t}(\theta_i)\xi\left(\mu,\mu',\sigma\right), \tag{6.25}$$

where $\tilde{t}(\theta_i)$ is the power transmission coefficient at incident angle θ_i. Similar to Eq. (6.15), the transmitted radiation can also be expressed as

$$\psi_t' = \mu I\left(\tau_a + \tau_{\text{int}}, -\mu, \varphi\right) S d\Omega, \tag{6.26}$$

where $I\left(\tau_a + \tau_{\text{int}}, -\mu, \varphi\right)$ is the radiance along **v** direction at the top of the ocean. τ_{int} is the optical thickness of the interface, which is infinitesimal. In the model, τ_{int} is assumed to be zero. $d\Omega$ here is the differential solid angle around the transmission direction.

Because Eqs. (6.25) and (6.26) are equal, we have

$$I\left(\tau_a + \tau_{\text{int}}, -\mu, \varphi\right) = F_o\cos\theta_i \frac{\tilde{t}(\theta_i)\xi\left(\mu,\mu',\sigma\right)}{\pi\sigma^2\mu\mu_f^4}\exp\left(-\frac{1-\mu_f^2}{\sigma^2\mu_f^2}\right)\frac{d\Omega_f}{d\Omega}. \tag{6.27}$$

In a Cartesian coordinate system with **v**′, and two directions perpendicular to **v**′ and each other as axes, (θ, φ) are

$$\theta = \theta_i - \theta_t, \tag{6.28a}$$

$$\varphi = \varphi_i . \tag{6.28b}$$

Using Snell's law, $d\Omega$ in Eq. (6.27) is

$$d\Omega = \sin(\theta_i - \theta_t)\det\frac{\partial(\theta,\varphi)}{\partial(\theta_i,\varphi_i)} = \sin(\theta_i - \theta_t)\left(1 - \frac{n_a\cos\theta_i}{n_{\text{o}}\cos\theta_t}\right)d\theta_i d\varphi_i . \tag{6.29}$$

Combining Eqs. (6.18a), (6.27) and (6.29), analogous to deriving BRDF, we obtain the bidirectional transmission distribution function (BTDF) at the air-sea interface:

$$T_{\text{int}}\left(\mu,\mu',\varphi-\varphi'\right) = \frac{\tilde{t}(\theta_i)\xi\left(\mu,\mu',\sigma\right)}{\sigma^2\mu'\mu\mu_f^4}\exp\left(-\frac{1-\mu_f^2}{\sigma^2\mu_f^2}\right)\frac{n_{\text{o}}^2\cos\theta_i\cos\theta_t}{\left(n_{\text{o}}\cos\theta_t - n_a\cos\theta_i\right)^2} . \tag{6.30}$$

The transmission matrix is obtained by generalizing Eq. (6.30) to consider polarization:

$$\begin{aligned}\mathbf{T}_{\text{int}}\left(\mu,\mu',\varphi-\varphi'\right) &= \frac{\xi\left(\mu,\mu',\sigma\right)}{\sigma^2\mu'\mu\mu_f^4}\exp\left(-\frac{1-\mu_f^2}{\sigma^2\mu_f^2}\right)\frac{n_{\text{o}}^2\cos\theta_i\cos\theta_t}{\left(n_{\text{o}}\cos\theta_t - n_a\cos\theta_i\right)^2} \\ &\cdot\mathbf{L}(\pi-\eta_2)\mathbf{t}_a(\theta_i)\mathbf{L}(-\eta_1),\end{aligned} \tag{6.31}$$

in which $\mathbf{t}_a(\theta_i)$ is the Fresnel transmission matrix.

Eqs. (6.21) and (6.31) are reflection and transmission matrices in the air-incident case. The counterparts in the water-incident case are obtained in the same way,

$$\mathbf{R}_{\text{int}}^*\left(\mu,\mu',\varphi-\varphi'\right) = \frac{\xi\left(\mu,\mu',\sigma\right)}{4\sigma^2\mu'\mu\mu_f^4}\exp\left(-\frac{1-\mu_f^2}{\sigma^2\mu_f^2}\right)\mathbf{L}(\pi-\eta_2)\mathbf{r}_{\text{o}}(\theta_i)\mathbf{L}(-\eta_1) , \tag{6.32}$$

and

$$\begin{aligned}\mathbf{T}_{\text{int}}^*\left(\mu,\mu',\varphi-\varphi'\right) &= \frac{\xi\left(\mu,\mu',\sigma\right)}{\sigma^2\mu'\mu\mu_f^4}\exp\left(-\frac{1-\mu_f^2}{\sigma^2\mu_f^2}\right)\frac{n_a^2\cos\theta_i\cos\theta_t}{\left(n_a\cos\theta_t - n_{\text{o}}\cos\theta_i\right)^2} \\ &\cdot\mathbf{L}(\pi-\eta_2)\mathbf{t}_{\text{o}}(\theta_i)\mathbf{L}(-\eta_1),\end{aligned} \tag{6.33}$$

where $\mathbf{r}_{\mathrm{o}}(\theta_i)$ and $\mathbf{t}_{\mathrm{o}}(\theta_i)$ are Fresnel reflection and transmission matrices in the water-incident case.

The Fresnel reflection and transmission matrices mentioned above are defined as (Zhai et al. 2010)

$$\mathbf{r}_a(\theta_i)=\frac{1}{2}\begin{pmatrix} r_{a,\parallel}^2+r_{a,\perp}^2 & r_{a,\parallel}^2-r_{a,\perp}^2 & 0 & 0 \\ r_{a,\parallel}^2-r_{a,\perp}^2 & r_{a,\parallel}^2+r_{a,\perp}^2 & 0 & 0 \\ 0 & 0 & 2\operatorname{Re}\left(r_{a,\perp}r_{a,\parallel}^*\right) & 2\operatorname{Im}\left(r_{a,\parallel}r_{a,\perp}^*\right) \\ 0 & 0 & 2\operatorname{Im}\left(r_{a,\perp}r_{a,\parallel}^*\right) & 2\operatorname{Re}\left(r_{a,\perp}r_{a,\parallel}^*\right) \end{pmatrix}, \tag{6.34a}$$

$$\mathbf{r}_{\mathrm{o}}(\theta_i)=\frac{1}{2}\begin{pmatrix} r_{\mathrm{o},\parallel}^2+r_{\mathrm{o},\perp}^2 & r_{\mathrm{o},\parallel}^2-r_{\mathrm{o},\perp}^2 & 0 & 0 \\ r_{\mathrm{o},\parallel}^2-r_{\mathrm{o},\perp}^2 & r_{\mathrm{o},\parallel}^2+r_{\mathrm{o},\perp}^2 & 0 & 0 \\ 0 & 0 & 2\operatorname{Re}\left(r_{\mathrm{o},\perp}r_{\mathrm{o},\parallel}^*\right) & 2\operatorname{Im}\left(r_{\mathrm{o},\parallel}r_{\mathrm{o},\perp}^*\right) \\ 0 & 0 & 2\operatorname{Im}\left(r_{\mathrm{o},\perp}r_{\mathrm{o},\parallel}^*\right) & 2\operatorname{Re}\left(r_{\mathrm{o},\perp}r_{\mathrm{o},\parallel}^*\right) \end{pmatrix}, \tag{6.34b}$$

$$\mathbf{t}_a(\theta_i)=\frac{1}{2}\frac{n_{\mathrm{o}}\cos\theta_t}{n_a\cos\theta_i}\begin{pmatrix} t_{a,\parallel}^2+t_{a,\perp}^2 & t_{a,\parallel}^2-t_{a,\perp}^2 & 0 & 0 \\ t_{a,\parallel}^2-t_{a,\perp}^2 & t_{a,\parallel}^2+t_{a,\perp}^2 & 0 & 0 \\ 0 & 0 & 2\operatorname{Re}\left(t_{a,\perp}t_{a,\parallel}^*\right) & 2\operatorname{Im}\left(t_{a,\parallel}t_{a,\perp}^*\right) \\ 0 & 0 & 2\operatorname{Im}\left(t_{a,\perp}t_{a,\parallel}^*\right) & 2\operatorname{Re}\left(t_{a,\perp}t_{a,\parallel}^*\right) \end{pmatrix}, \tag{6.34c}$$

$$\mathbf{t}_{\mathrm{o}}(\theta_i)=\frac{1}{2}\frac{n_a\cos\theta_t}{n_{\mathrm{o}}\cos\theta_i}\begin{pmatrix} t_{\mathrm{o},\parallel}^2+t_{\mathrm{o},\perp}^2 & t_{\mathrm{o},\parallel}^2-t_{\mathrm{o},\perp}^2 & 0 & 0 \\ t_{\mathrm{o},\parallel}^2-t_{\mathrm{o},\perp}^2 & t_{\mathrm{o},\parallel}^2+t_{\mathrm{o},\perp}^2 & 0 & 0 \\ 0 & 0 & 2\operatorname{Re}\left(t_{\mathrm{o},\perp}t_{\mathrm{o},\parallel}^*\right) & 2\operatorname{Im}\left(t_{\mathrm{o},\parallel}t_{\mathrm{o},\perp}^*\right) \\ 0 & 0 & 2\operatorname{Im}\left(t_{\mathrm{o},\perp}t_{\mathrm{o},\parallel}^*\right) & 2\operatorname{Re}\left(t_{\mathrm{o},\perp}t_{\mathrm{o},\parallel}^*\right) \end{pmatrix}, \tag{6.34d}$$

where the subscripts || and ⊥ denote the polarization directions parallel and perpendicular to the incident plane respectively. The power reflection coefficient $\tilde{r}(\theta_i)$ in Eq. (6.20) is the 1, 1-element in Eq. (6.34a), and the power transmission coefficient $\tilde{t}(\theta_i)$ in Eq. (6.30) is the 1, 1-element in Eq. (6.34c).

The Fresnel coefficients in Eq. (6.34) are

$$r_{a,\|} = \frac{n_o^2 \cos\theta_i - n_a \sqrt{n_o^2 - n_a^2 \sin\theta_i}}{n_o^2 \cos\theta_i + n_a \sqrt{n_o^2 - n_a^2 \sin\theta_i}}\,, \tag{6.35a}$$

$$r_{a,\perp} = \frac{n_a \cos\theta_i - \sqrt{n_o^2 - n_a^2 \sin\theta_i}}{n_a \cos\theta_i + \sqrt{n_o^2 - n_a^2 \sin\theta_i}}\,, \tag{6.35b}$$

$$r_{o,\|} = \frac{n_a^2 \cos\theta_i - n_o \sqrt{n_a^2 - n_o^2 \sin\theta_i}}{n_a^2 \cos\theta_i + n_o \sqrt{n_a^2 - n_o^2 \sin\theta_i}}\,, \tag{6.35c}$$

$$r_{o,\perp} = \frac{n_o \cos\theta_i - \sqrt{n_a^2 - n_o^2 \sin\theta_i}}{n_o \cos\theta_i + \sqrt{n_a^2 - n_o^2 \sin\theta_i}}\,, \tag{6.35d}$$

$$t_{a,\|} = \frac{2 n_a n_o \cos\theta_i}{n_o^2 \cos\theta_i + n_a \sqrt{n_o^2 - n_a^2 \sin\theta_i}}\,, \tag{6.35e}$$

$$t_{a,\perp} = \frac{2 n_a \cos\theta_i}{n_a \cos\theta_i + \sqrt{n_o^2 - n_a^2 \sin\theta_i}}\,, \tag{6.35f}$$

$$t_{o,\|} = \frac{2 n_a n_o \cos\theta_i}{n_a^2 \cos\theta_i + n_o \sqrt{n_a^2 - n_o^2 \sin\theta_i}}\,, \tag{6.35g}$$

$$t_{o,\perp} = \frac{2 n_o \cos\theta_i}{n_o \cos\theta_i + \sqrt{n_a^2 - n_o^2 \sin\theta_i}}\,. \tag{6.35h}$$

The adding-doubling calculations Eq. (6.1) involve the reflection and transmission matrix Fourier components at the interface. The Fourier components are computed by Eq. (4.39). Gaussian quadrature is utilized to evaluate the integral in Eq. (4.39).

Note that the local incidence (θ_i), reflection (θ_r) and refraction (θ_t) angles are related to the scattering angle Θ by

$$\theta_i = \theta_r = \frac{\pi - \Theta}{2}, \tag{6.36a}$$

$$\left|\theta_i - \theta_r\right| = \Theta . \tag{6.36b}$$

Because θ_i, θ_r and θ_t are in the angle range (0, $\pi/2$), the range of Θ is limited to (0, π) in computing reflection matrix, and limited to (0, arccos(n_a/n_o)) in computing transmission matrix. The scattering angle Θ is determined by the incident and outgoing directions, and varies from 0 to π. Thus, if Θ is out of the range (0, arccos(n_a/n_o)), transmission is impossible to happen, and the transmission matrix is set to zero matrix. The transmission matrix as a function of zenith and azimuth angles may be discontinuous. Also, in the water-incident case, total internal reflection may occur. The Fresnel coefficients change abruptly around the total internal reflection angle, which introduces derivative discontinuity to both reflection and transmission matrices.

These discontinuities from different reasons increase the number of Gaussian quadrature orders needed to compute angular integrations involving the interface reflection and transmission matrices to attain certain numerical accuracy.

6.2 Ocean Model

Because the ocean floor is assumed to be fully absorptive, we only consider the radiative properties of ocean water in developing the ocean model. In nature, the composition of ocean water is very complicated and varies spatially and temporally. In the ocean model, the ocean water contains pure water, phytoplankton pigments, CDOM and NAP. The IOPs that are significant in ocean optics and remote sensing include spectral scattering and absorption coefficients, and the Mueller matrix. In our RT calculation, the needed input parameters are optical thickness, single-scattering albedo and scattering matrix. The IOPs can be easily converted to the RTM input parameters using proper assumptions.

We assume that the IOPs of ocean water are the sums of each composition's corresponding properties. For Case I water defined in Morel and Prieur (1977), the total absorption coefficient a_{tot} is

$$a_{\mathrm{tot}} = a_{\mathrm{w}} + a_{\mathrm{c}} + a_{\mathrm{p}}, \tag{6.37}$$

where the subscripts "w", "c", and "p" represent water, CDOM, and phytoplankton with associated NAPs respectively. Similarly, the total scattering coefficient b_{tot} is

$$b_{\mathrm{tot}} = b_{\mathrm{w}} + b_{\mathrm{p}}, \tag{6.38}$$

in which the scattering by CDOM is ignored.

The optical thickness of the ocean water is

$$\tau_{\mathrm{o}} = \left(a_{\mathrm{tot}} + b_{\mathrm{tot}}\right) l_{\mathrm{o}}, \tag{6.39}$$

in which l_o is the geometric depth of the ocean. In Eq. (6.39), the absorption and scattering coefficients are assumed to be constant with depth in the vertical direction. The single-scattering albedo of the ocean water is

$$\varpi_\mathrm{o} = \frac{b_\mathrm{tot}}{a_\mathrm{tot} + b_\mathrm{tot}}. \tag{6.40}$$

The scattering matrix of the ocean water is

$$\mathbf{F}_\mathrm{o} = \frac{b_\mathrm{w}\mathbf{F}_\mathrm{w} + b_\mathrm{p}\mathbf{F}_\mathrm{p}}{b_\mathrm{tot}}. \tag{6.41}$$

The absorption and scattering coefficients of the ocean water compositions are functions of the compound concentrations as well as wavelength. Previous studies (e.g. Bricaud et al. 1981, 1995, 1998; Loisel and Morel 1998; Morel and Maritorena 2001; Huot et al. 2008) measure and analyze the relation between the IOPs and phytoplankton concentration. Here the bio-optical models in previous studies are adopted in the ocean water model.

For the CDOM absorption coefficient, the wavelength dependence relation of the absorption coefficient proposed by Bricaud et al. (1981) is used:

$$a_\mathrm{c}(\lambda) = a_\mathrm{c}(\lambda_0)\exp\left[-S\left(\lambda - \lambda_0\right)\right], \tag{6.42}$$

where S is a parameter independent of wavelength. The mean value of S estimated from measurements is 0.014 nm^{-1} (Bricaud et al. 1981). $a_\mathrm{c}(\lambda_0)$ is the absorption coefficient at a reference wavelength λ_0 that has unit nm. The unit of absorption coefficient is m^{-1}. Here the reference wavelength λ_0 is chosen at 440 nm so the relation (Bricaud et al. 1998)

$$a_{\mathrm{c}}(440) = \kappa[a_{\mathrm{w}}(440) + a_{\mathrm{p}}(440)], \tag{6.43}$$

can be used. κ is often chosen as 0, 0.1 or 0.2 to produce a different increase rate (Bricaud et al. 1998).

The spectral pure water absorption coefficient $a_{\mathrm{w}}(\lambda)$ is from the measurement by Pope and Fry (1997). The spectral phytoplankton and associated NAPs absorption coefficients $a_{\mathrm{p}}(\lambda)$ are parameterized by Bricaud et al. (1998) as

$$a_{\mathrm{p}}(\lambda) = A_{\mathrm{p}}(\lambda)\left\langle \mathrm{Chl} \right\rangle^{E_{\mathrm{p}}(\lambda)}, \tag{6.44}$$

where the wavelength-dependent parameters $A_{\mathrm{p}}(\lambda)$ and $E_{\mathrm{p}}(\lambda)$ are kindly provided by Dr. Annick Bricaud. $\left\langle \mathrm{Chl} \right\rangle$ is the chlorophyll concentration with the unit mg/m^3.

The water scattering coefficient b_{w} (Mobley 1994) is computed by

$$b_{\mathrm{w}}(\lambda) = 0.00193\left(\frac{550}{\lambda}\right)^{4.32}. \tag{6.45}$$

The scattering coefficient of phytoplankton and associated NAPs b_{p} is given by the bio-optical model proposed by Huot et al. (2008):

$$b_{\mathrm{p}}(\lambda) = b_{\mathrm{p}}(660)\left(\frac{\lambda}{660}\right)^{\rho}, \tag{6.46}$$

in which ρ is a parameter dependent on $\left\langle \mathrm{Chl} \right\rangle$:

$$\begin{aligned} &\rho = 0.5\left(\log_{10}\left\langle \mathrm{Chl} \right\rangle - 0.3\right), && 0.02 < \left\langle \mathrm{Chl} \right\rangle < 2\ \mathrm{mg/m^3} \\ &\rho = 0, && \left\langle \mathrm{Chl} \right\rangle > 2\ \mathrm{mg/m^3} \end{aligned}. \tag{6.47}$$

$b_\mathrm{p}(660)$ is the scattering coefficient at 660 nm wavelength. It is parameterized with respect to $\langle \mathrm{Chl} \rangle$ as (Huot et al., 2008)

$$b_\mathrm{p}(660) = 0.347 \langle \mathrm{Chl} \rangle^{0.766} . \tag{6.48}$$

The scattering properties of pure water can be described by Rayleigh scattering theory. The scattering function (the 1, 1-element of the scattering matrix) of pure water is (Mobley 1994)

$$a_1^\mathrm{w} = 4\pi \cdot 0.06225 \left(1 + 0.835 \cos^2 \Theta \right), \tag{6.49}$$

in which multiplication by 4π normalizes it to be dimensionless. If the depolarization effect is considered, the scattering matrix elements of Rayleigh scattering can be expressed as (Hovenier et al. 2004)

$$a_1(\Theta) = 0.75 \bar{c} \cos^2 \Theta + 1 - 0.25 \bar{c} , \tag{6.50a}$$

$$a_2(\Theta) = 0.75 \bar{c} \left(1 + \cos^2 \Theta \right), \tag{6.50b}$$

$$a_3(\Theta) = 1.5 \bar{c} \cos \Theta , \tag{6.50c}$$

$$a_4(\Theta) = 1.5 \bar{d} \cos \Theta , \tag{6.50d}$$

$$b_1(\Theta) = 0.75 \bar{c} \left(\cos^2 \Theta - 1 \right), \tag{6.50e}$$

$$b_2(\Theta) = 0 , \tag{6.50f}$$

where $\bar{c}$ and $\bar{d}$ are parameters related to the depolarization effect, and $\bar{c}$ and $\bar{d}$ are related by

$$\bar{d} = \frac{5\bar{c} - 2}{3}. \tag{6.51}$$

Comparing Eqs. (6.50a) and (6.49), we find that when $\bar{c}$ is equal to 0.87097, Eqs. (6.49) and (6.50a) are equivalent. Thus, the scattering matrix of pure water is obtained.

For the scattering matrix of phytoplankton and associated NAPs, we use the distorted hexahedron ensemble model proposed by Xu et al. (2017). The single-scattering properties of the model are computed by a synergistic combination of the IITM method and the PGOM method. The relative refractive indices used in the model development cover the range of aquatic particles (Chowdhary et al. 2012; Zhang and Gray 2015).

In Case II water as defined by Morel and Prieur (1977), the inorganic particles have higher concentration than organic particles such as phytoplankton so inorganic particles dominates the IOP of the ocean water (Zhang et al. 2017). The organic particles have smaller relative refractive indices than inorganic particles (Zhang and Gray 2015). In Case II water, the bio-optical model introduced above may not be valid.

6.3 Illustrative Results

Currently, there is no published benchmark radiative transfer calculation results involving an air-sea interface. The main characteristic of the atmosphere-ocean coupled RTM is that it includes both the reflection and transmission matrices of the interface. Fig. 27 shows the simulated Stokes vectors of upward radiation immediately above the air-sea interface when the atmosphere is ignored.

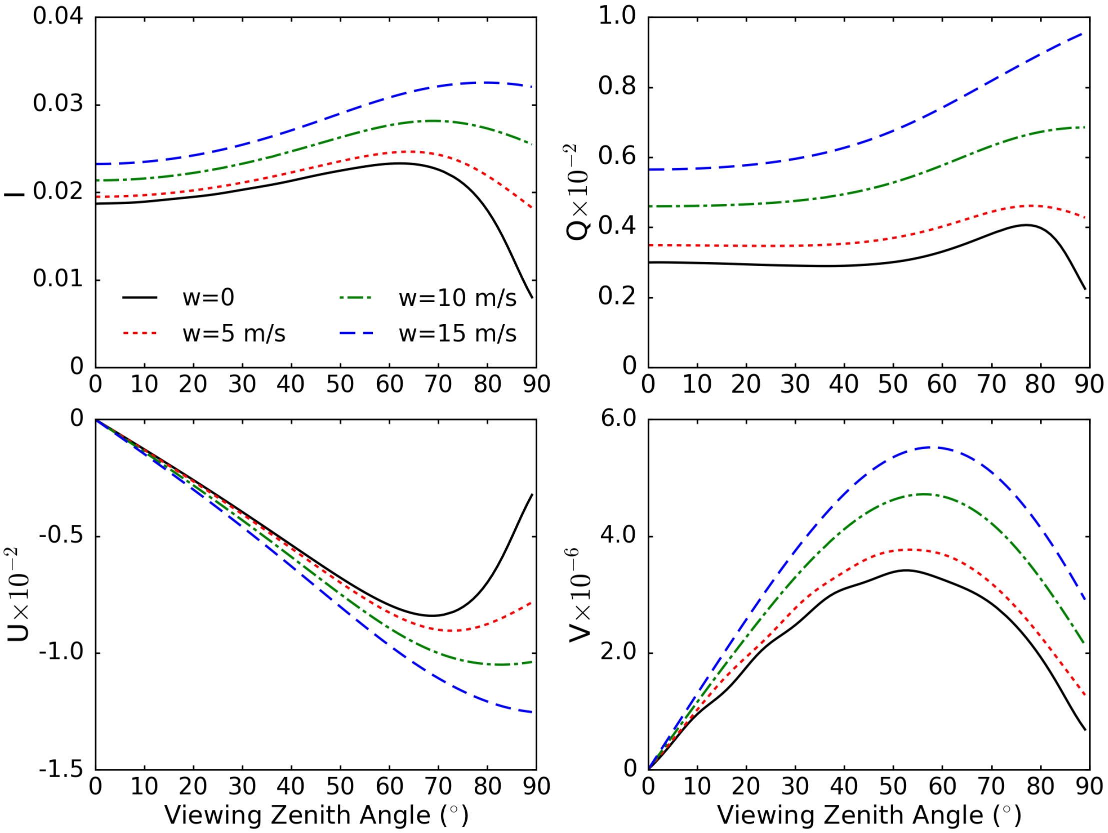

Figure 27 The Stokes vectors of upward radiation computed immediately above the air-sea interface with four different surface wind speeds (w). The solar zenith angle is 60°, and the azimuth angle is 90°. The ocean is assumed to have chlorophyll concentration 1.2 mg/m^3, and has optical thickness 10. The complex refractive index of the phytoplankton and associated NAPs is set to 1.06+i0.005. The atmosphere optical thickness is zero. The Stokes vectors are normalized by the incident radiation so they are dimensionless.

Four surface wind speeds are considered in the calculations. The upward radiation comes from reflected radiation by the interface, and the radiation transmitted out of the interface. With larger surface wind speed, the upward radiance (Stokes vector element *I*) is larger. The absolute values of the Stokes vector elements *Q*, *U* and *V* are also larger for larger surface wind speed. Obviously, the intensity and polarization of the upward radiation are sensitive to the surface wind speed.

The angular distribution of the upward radiance tends to be more isotropic when the wind speed increases. In the rough surface model introduced above, when the wind speed increases, the variance σ^2 of the probability density function of the surface orientation becomes larger so the rough surface orientation distribution is less anisotropic. The radiation coming from different directions have more uniform chances to be reflected and refracted so the radiance angular distribution is more isotropic.

Using the bio-optical models and Eqs. (6.39) and (6.40), the ocean optical thickness (τ_o) and single-scattering albedo (ϖ_o) are computed. Fig. 28 shows the examples of simulated spectral τ_o and ϖ_o. As the chlorophyll concentration increases, τ_o and ϖ_o increase since the scattering effect is more strongly enhanced than the absorption effect. With the same chlorophyll concentration, τ_o and ϖ_o do not vary much at wavelengths less than 550 nm. At wavelengths larger than 550 nm, τ_o increases but ϖ_o decreases, because water absorption substantially strengthens in this wavelength range.

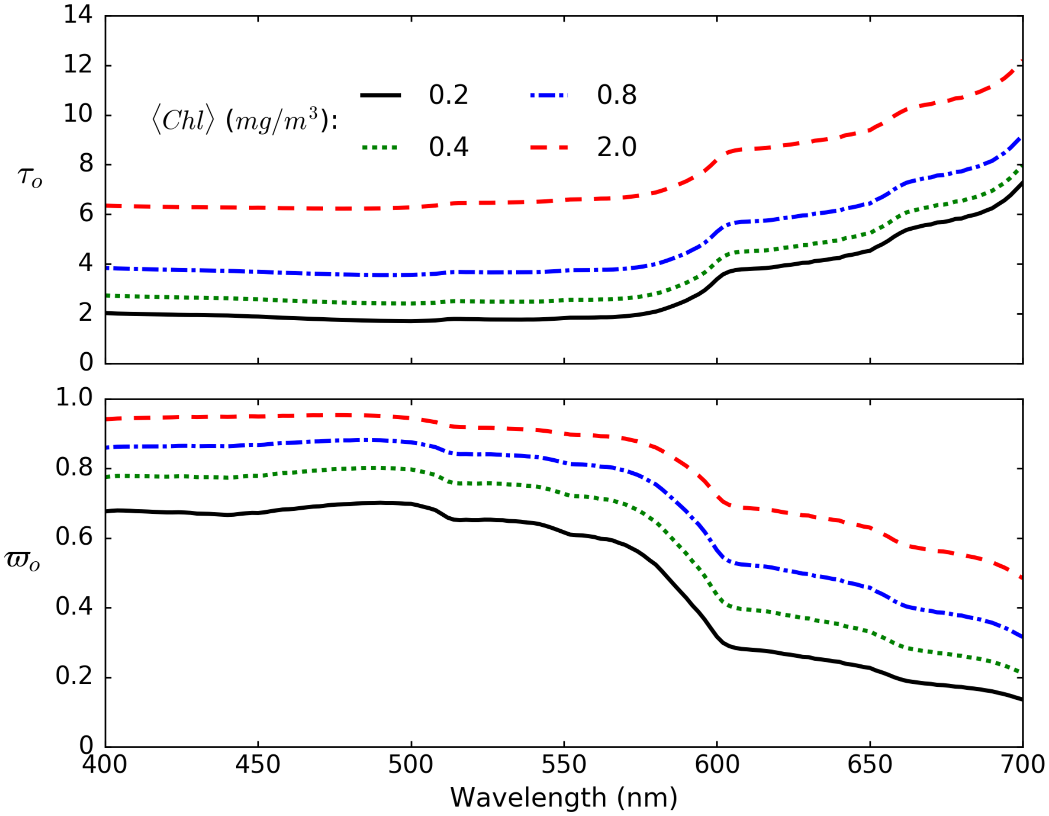

Figure 28 Simulated ocean optical thickness and single-scattering albedo in the wavelength range 400 to 700 nm for various chlorophyll concentrations. The ocean depth is set to 10 m. The κ factor in Eq. (6.43) is chosen to be 0.2.

Using the spectral τ_o and ϖ_o in Fig. 28, we compute the spectral Stokes vectors of the upward radiation immediately above the air-sea interface in a specific viewing direction, as shown in Fig. 29. At the same wavelength, the radiance is larger for higher chlorophyll concentration, and the absolute values of Stokes elements Q, U and V are also larger, since the scattering ability of the ocean water inceases. With the same chlorophyll concentration, the radiance and the absolute values of other Stokes elements decrease almost monotonically from 400 nm to 700 nm wavelengths, since the ocean water absorption ability increases. Fig. 29 shows that the upward radiation is sensitive to ocean chlorophyll concentration in terms of both intensity and polarization. The sensitivities of the upward radiation to the ocean surface wind and water properties are the physical bases of ocean remote sensing.

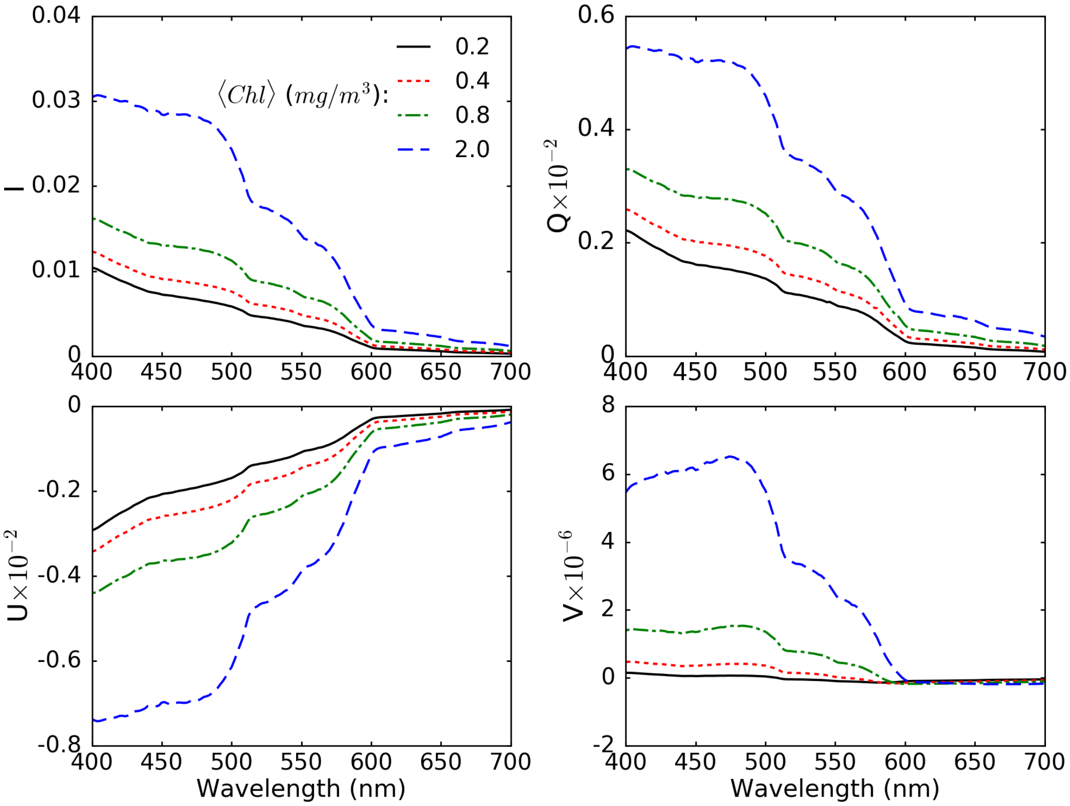

Figure 29 The Stokes vectors of upward radiation computed immediately above the air-sea interface with the spectral ocean optical thickness and single-scattering albedo data shown in Fig. 28. The surface wind speed is set to be 7 m/s. The solar zenith angle is 60°, viewing zenith angle is 40°, and the azimuth angle is 90°. The atmosphere optical thickness is zero. The Stokes vectors are normalized by the incident radiation so they are dimensionless.

CHAPTER VII

COMPARISON WITH SATELLITE OBSERVATIONS

All vector RTM modules introduced in previous chapters are integrated into a simulator of satellite instruments. In this chapter, the simulation results are compared with POLDER and MODIS observations. For POLDER observations, the reflectance and polarized reflectance at 0.865 μm band are simulated. For MODIS observations, the radiance at band 31 (10.78~11.28 μm) is simulated.

7.1 Simulation Region and Input Data

The simulation region is shown in Fig. 30. Fig. 30 is an RGB image plotted using reflectance data in 0.490 μm (blue), 0.565 μm (green) and 0.670 μm (red) bands obtained from the Polarization & Anisotropy of Reflectances for Atmospheric Sciences Coupled with Observations from a Lidar (PARASOL) Level-1B product (Fougnie et al. 2007), which was derived from the observations of POLDER instrument on board the PARASOL satellite. The region is over the Indian Ocean southwest of Sri Lanka, so no land surface pixels are analyzed in this study. The observation time is July 1st, 2008 around 0845 UTC.

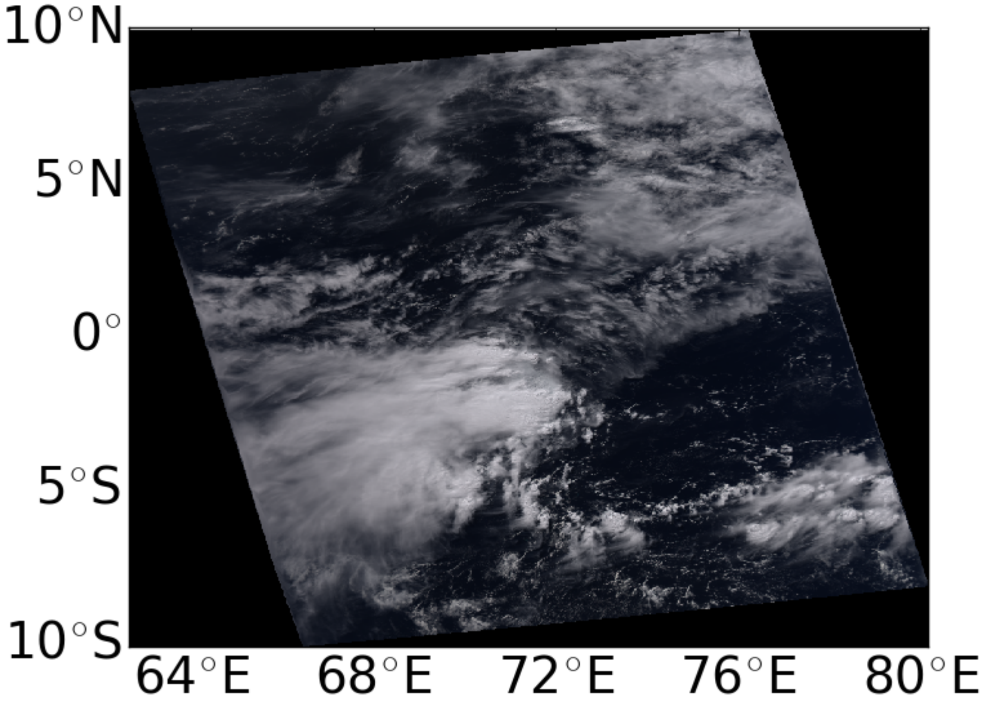

Figure 30 RGB image plotted using the data from PARASOL Level-1B product. The location is over the Indian Ocean southwest of Sri Lanka. The observation time is July 1st, 2008 around 0845 UTC.

We collocate the PARASOL pixels in Fig. 30 with the Aqua MODIS Level-2 Collection 6 cloud product (Platnick et al. 2017). The collocated cloud phase information is shown in Fig. 31. Many pixels have ice clouds. Other pixels have liquid clouds, clear sky, or mixed phase or unknown clouds.

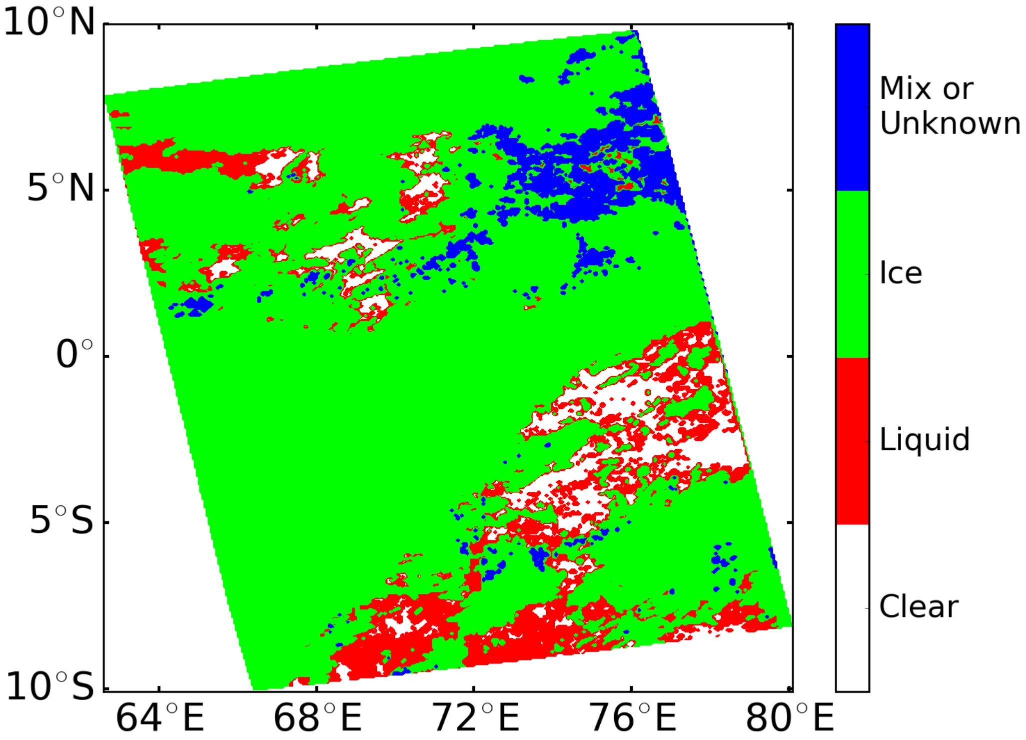

Figure 31 Cloud phase information collocated with the pixels in Fig. 30. The cloud phase data are from Aqua MODIS Level-2 Collection 6 cloud product.

For the pixels in Fig. 30, we only consider cloudy and clear-sky cases in the simulation and ignore aerosol since aerosol loading is low in this area during the observation period. The cloud phase, cloud optical thickness, cloud effective radius, cloud top height, cloud top pressure, and cloud top temperature are from the collocated Aqua MODIS Level-2 Collection 6 cloud product.

The atmospheric profile data are obtained from collocated Modern-Era Retrospective Analysis for Research and Application, Version 2 (MERRA-2) (Gelaro et al. 2017) instantaneous 3h 3-dimensional assimilated meteorological fields, and CO and CO_2 mixing ratios. The ice and liquid cloud models utilized in the simulations are consistent with those used in the MODIS Collection 6 cloud product retrieval algorithm.

7.2 Simulation Procedure

A flowchart in Fig. 32 shows the data flow in the simulations.

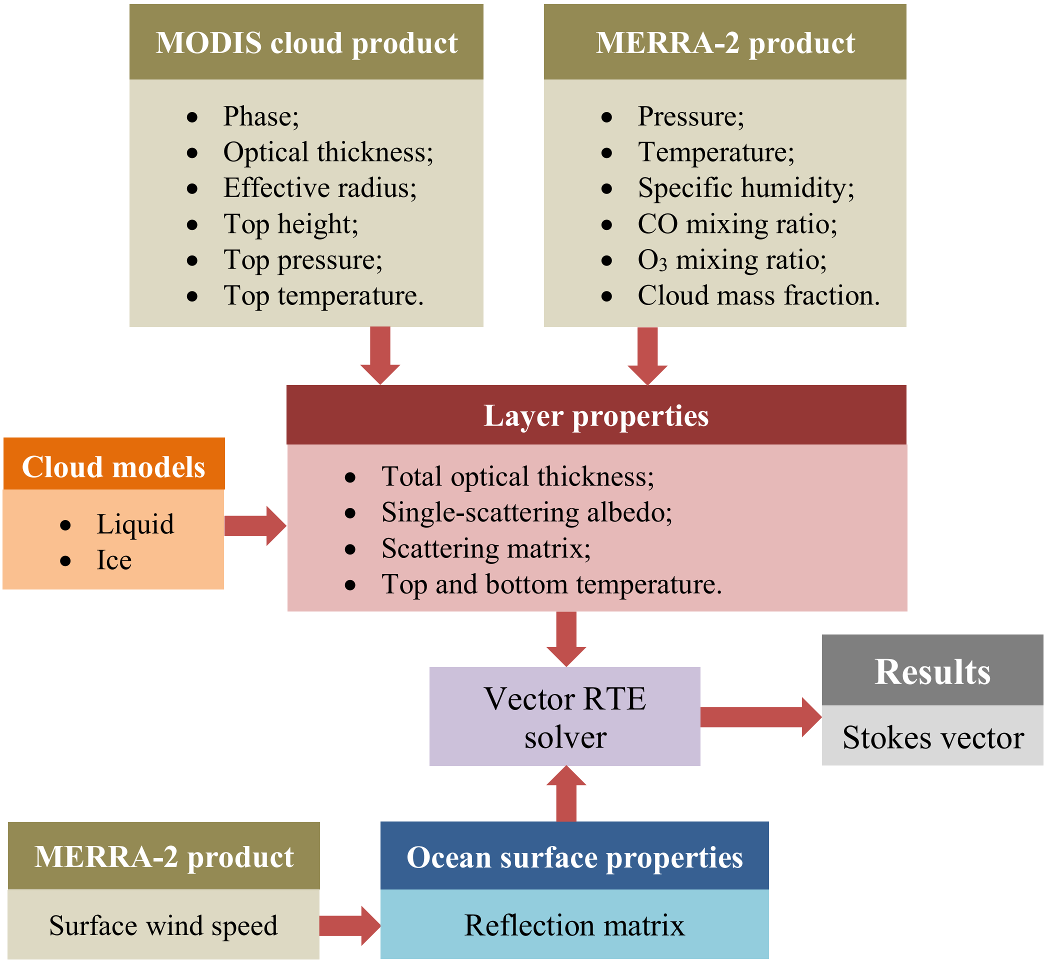

Figure 32 Flowchart to show the data flow of the simulation process using the developed radiative transfer model.

Cloud phase data determines the type of cloud model (liquid or ice) to be used in radiative transfer calculations. For a mixed phase or unknown phase, the liquid cloud is assumed in the calculation. The cloud optical thickness is computed at the 0.55 μm wavelength in MODIS data. It can be converted to the optical thickness at another wavelength λ by

$$\tau_{\mathrm{cld}}(\lambda)=\frac{Q_{ext}(\lambda)}{Q_{ext}(0.55)}\tau_{\mathrm{cld}}(0.55), \tag{7.1}$$

where subscript "cld" denotes cloud. Q_{ext} is the extinction efficiency of the cloud. Because the cloud model single-scattering properties are pre-computed at discrete effective radii, linear interpolations are applied to obtain the cloud scattering matrices at specific effective radii provided by the MODIS cloud effective radius data.

The MODIS cloud top height, pressure and temperature, and MERRA-2 atmospheric profile data are used to determine the above-cloud atmospheric gas absorption and Rayleigh scattering. There is no cloud base data available in either dataset. We use the cloud mass fraction information in the MERRA-2 product to estimate the cloud base height, pressure and temperature, which are used to compute the below-cloud atmospheric gas absorption and Rayleigh scattering. The cloud top and base temperatures are also utilized in cloud thermal emission calculations. The sea surface temperature data in the MERRA-2 product is used to compute ocean surface thermal emission. The sea surface emissivity is set to 0.98 in TIR bands (Wang et al. 2015).

The gas absorption module computes the air absorption optical thickness using MERRA-2 atmospheric profile data. For wavelengths ranging from UV to NIR, the Rayleigh scattering optical thickness by atmospheric gases is comparable to the typical aerosol and thin cirrus cloud optical thickness, and thus should not be ignored in radiative transfer calculations. The Rayleigh optical thickness calculation method and related data in Bodhaine et al. (1999) are used to compute air scattering optical thickness. The Rayleigh scattering matrix is given by Eq. (6.50). The parameter $\overline{c}$ is related to the air depolarization ratio ρ_n (Hovenier et al. 2004) by

$$\overline{c} = \frac{2\left(1-\rho_n\right)}{2+\rho_n}, \tag{7.2}$$

where ρ_n is wavelength-dependent and obtained from Bodhaine et al. (1999). The total optical thickness and single-scattering albedo in a model atmospheric layer is

$$\tau_a = \tau_{\mathrm{cld}} + \tau_{\mathrm{air}}^{\mathrm{abs}} + \tau_{\mathrm{air}}^{\mathrm{sca}}, \tag{7.3a}$$

$$\varpi_a = \frac{\tau_{\mathrm{cld}}\varpi_{\mathrm{cld}} + \tau_{\mathrm{air}}^{\mathrm{sca}}}{\tau_a}, \tag{7.3b}$$

where $\tau_{\mathrm{air}}^{\mathrm{abs}}$ and $\tau_{\mathrm{air}}^{\mathrm{sca}}$ are air absorption and scattering optical thicknesses. The total scattering matrix is

$$\mathbf{F}_a(\Theta) = \frac{\tau_{\mathrm{cld}}\varpi_{\mathrm{cld}}\mathbf{F}_{\mathrm{cld}}(\Theta) + \tau_{\mathrm{air}}^{\mathrm{sca}}\mathbf{F}_{\mathrm{air}}(\Theta)}{\tau_{\mathrm{cld}}\varpi_{\mathrm{cld}} + \tau_{\mathrm{air}}^{\mathrm{sca}}}. \tag{7.4}$$

The surface wind speed data in the MERRA-2 product are utilized to compute the ocean surface reflection matrix, Eq. (6.21). The wavelengths involved in the simulations are in IR bands, where the contribution of water-leaving radiance is very small due to strong absorption by ocean water. Thus, only the reflection by the ocean surface is considered in the simulations. The layer properties and surface reflection matrix are input to the vector RTE solver that outputs the Stokes vectors at specified positions and directions.

7.3 Simulated Satellite Observations

7.3.1 Simulated POLDER Observations

The comparison between the observed and simulated POLDER reflectance is shown in Fig. 33 for the region illustrated in Fig. 30. The simulation looks very similar to the observation, especially in the pixels that have large reflectance. In the pixels that have small reflectance, the difference between the observation and simulation is significant.

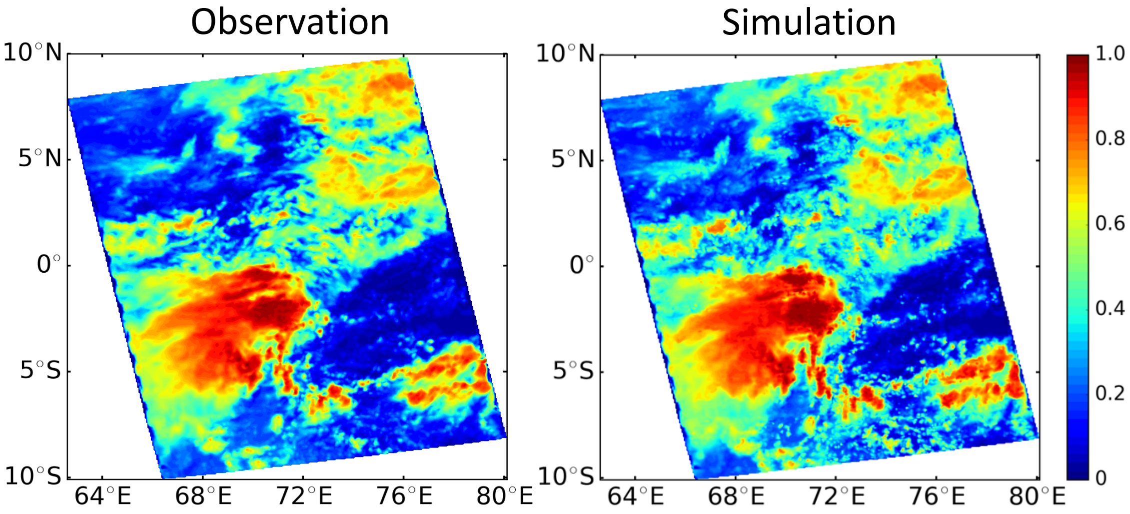

Figure 33 Comparison between the observed (left) and simulated (right) POLDER reflectance at 0.865 μm band for the region in Fig. 30.

To show the difference more clearly, the observed and simulated pixels are compared, as shown in Fig. 34. The data points show almost no systematic bias. When the observed reflectance is smaller than 0.5, the data point distribution is wider around the one-to-one line than for a larger reflectance. A larger reflectance usually corresponds to a larger optical thickness. The data point distribution in Fig. 34 implies that the uncertainty in the simulation is large for optically thin clouds.

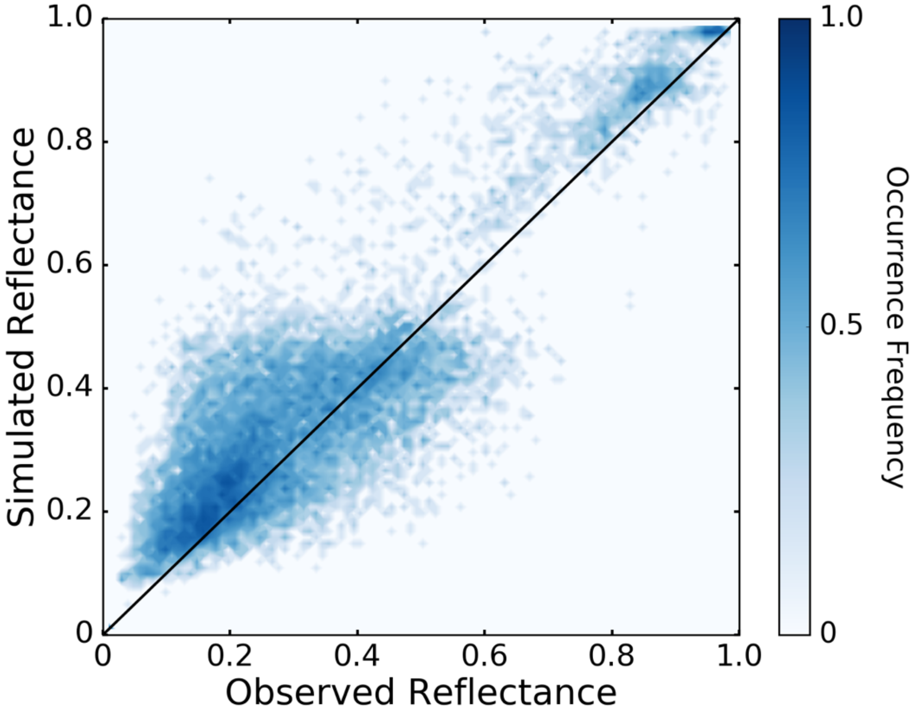

Figure 34 The pixel-by-pixel comparison of the observed and simulated reflectance shown in Fig. 33. The black diagonal line is the one-to-one line.

Fig. 35 shows the observed and simulated POLDER polarized reflectance images. In the left lower part of the images, the polarized reflectance signal is very strong since this part is close to the sun glint area and the clouds are optically thin. In other parts of the two images, it is hardly possible to see the difference.

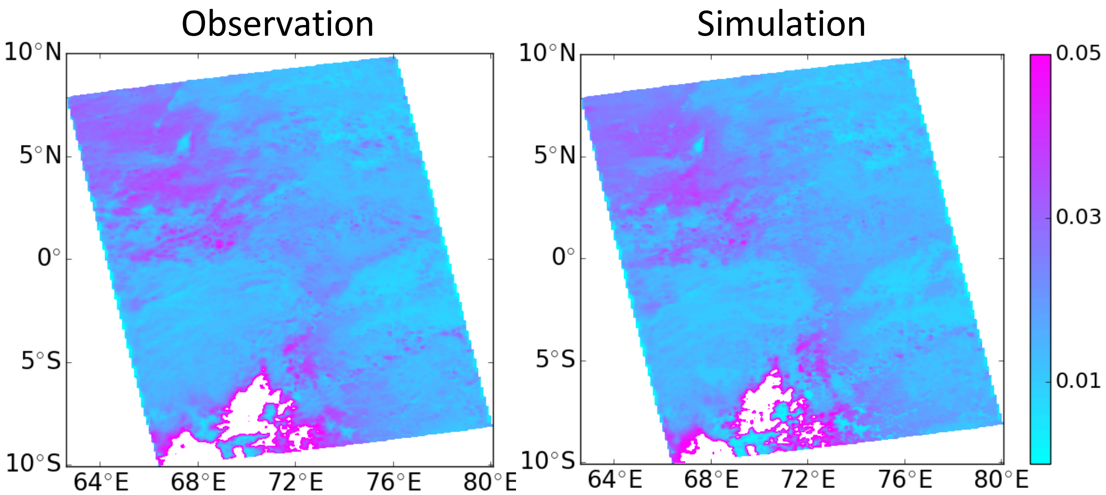

Figure 35 Comparison between the observed (left) and simulated (right) POLDER polarized reflectance in the 0.865 μm band for the region in Fig. 30.

The pixel-by-pixel comparison is shown in Fig. 36. Most of the polarized reflectance values are between 0.01 and 0.04. The data points are distributed almost symmetrically on the two sides of the one-to-one diagonal line. Note that the MODIS cloud product retrieval algorithm is only based on MODIS reflectance observations. The similarity between the observed and simulated polarized reflectance to some extent shows the accuracy of the developed RTM as well as the polarization consistency of the cloud models used in MODIS retrieval algorithms.

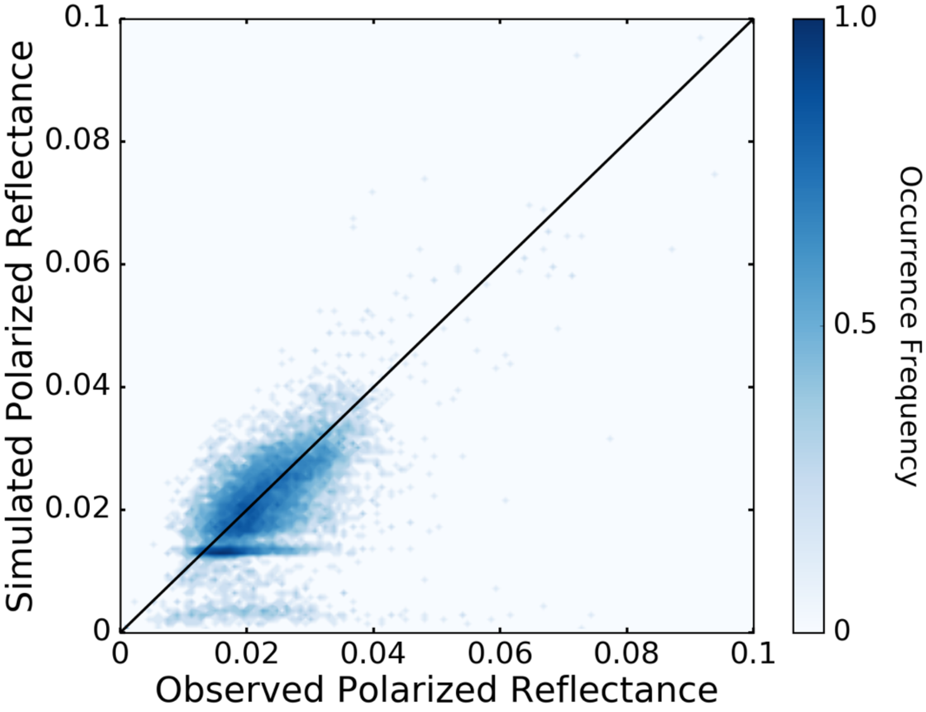

Figure 36 The pixel-by-pixel comparison of the observed and simulated polarized reflectance in Fig. 35. The black diagonal line is the one-to-one line.

7.3.2 Simulated MODIS Observations

The radiance in MODIS band 31 is the sum of thermal emission by the atmosphere and reflected solar radiation. The solar irradiance F_0 data are obtained from the AER solar irradiance dataset (Clough et al. 2005). The Planck function in the simulation is spectrally averaged within the band:

$$\overline{B}(T) = \frac{1}{\tilde{\nu}_2 - \tilde{\nu}_1} \int_{\tilde{\nu}_1}^{\tilde{\nu}_2} B(\tilde{\nu}, T)\, d\tilde{\nu} \ , \tag{7.5}$$

where wavenumbers $\tilde{\nu}_1$ and $\tilde{\nu}_2$ are the end points of the band interval.

The radiance can be converted to BT by inverting the Planck function at the band central wavenumber. Fig. 34 shows the observed and simulated MODIS band 31 radiance in terms of BT. The observation and simulation are similar.

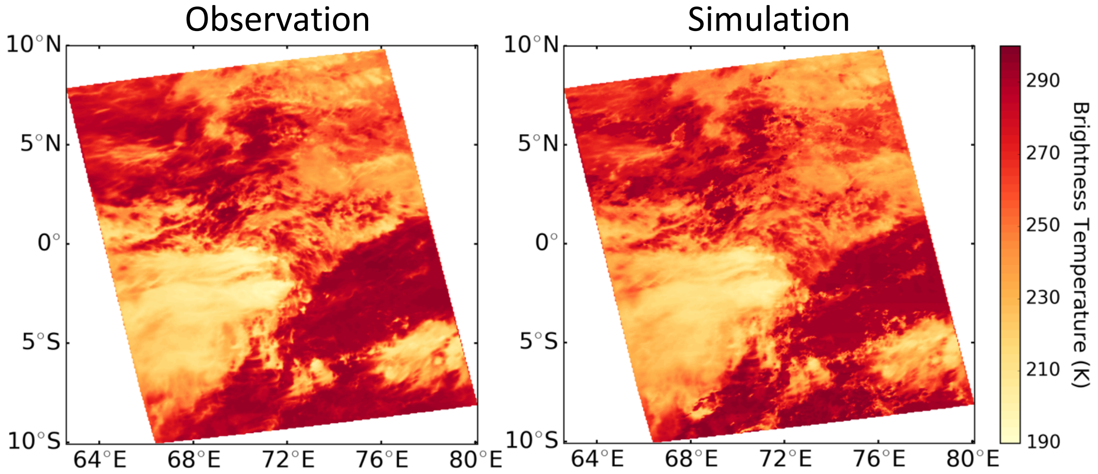

Figure 37 Comparison between the observed (left) and simulated (right) MODIS radiance at band 31 (10.78~11.28 μm) for the region in Fig. 30. The radiance is shown in terms of BT.

The gas absorption in MODIS band 31 is weak. The thermal emission from the surface and lower atmosphere can penetrate through the atmosphere and be received by the instrument. If there are clouds, the clouds block the transmission of part of the thermal emission from lower layers, and emit radiation with a colder temperature, which is received by the instrument. Thus, the BT values of cloudy pixels are generally colder than the clear-sky pixels.

Fig. 38 shows the pixel-by-pixel comparison of the observed and simulated MODIS band 31 radiance. For BT smaller than 270 K, the simulation overestimates the radiance. For BT larger than 270 K, the data points are almost unbiased.

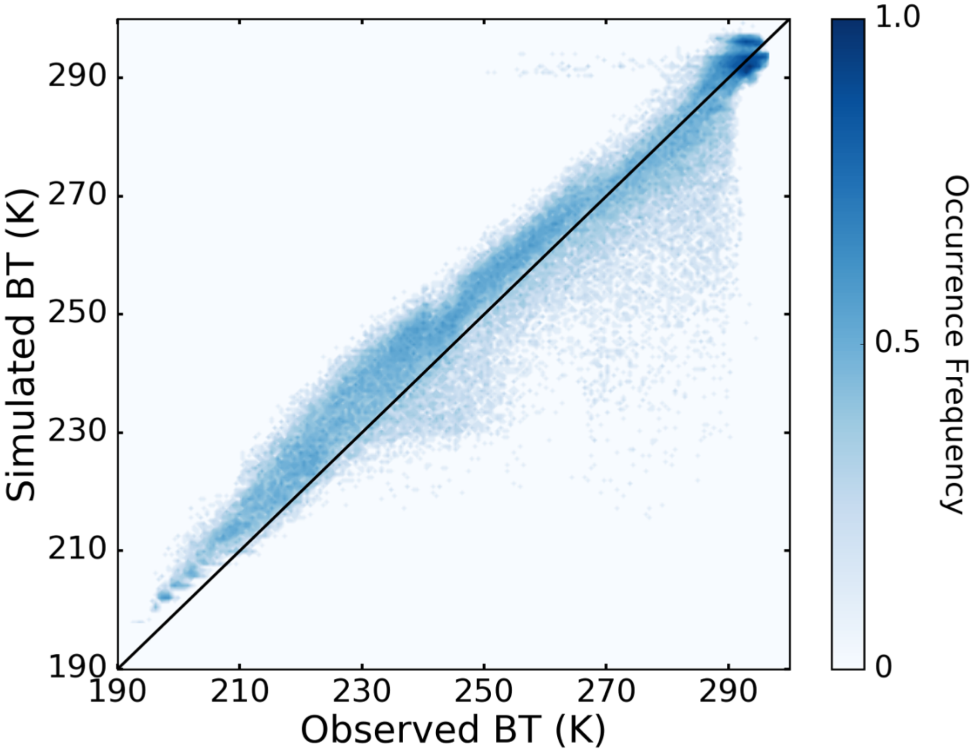

Figure 38 The pixel-by-pixel comparison of the observed and simulated radiance shown in Fig. 37. The black diagonal line is the one-to-one line.

We also compute the simulated horizontal minus vertical polarization brightness temperature difference (BTD) as shown in Fig. 39, with the simulation results in MODIS band 31. MODIS does not have polarization capability, so there is no observed MODIS polarization data. Except for the cloud properties, the BTD is also strongly dependent on the viewing zenith angle. Along the satellite track, the viewing zenith angles are close to zero, and the corresponding BTD values are almost zero. For pixels with large viewing zenith angles, the positive BTD values are close to 1 K. The BTD values of optically thick clouds are negative, whereas the BTD values of optically thin clouds are positive. The value of BTD tends to be inversely related to the cloud optical thickness, which is consistent with the POLDER polarized reflectance observations in the 0.865 μm band as shown in Fig. 35.

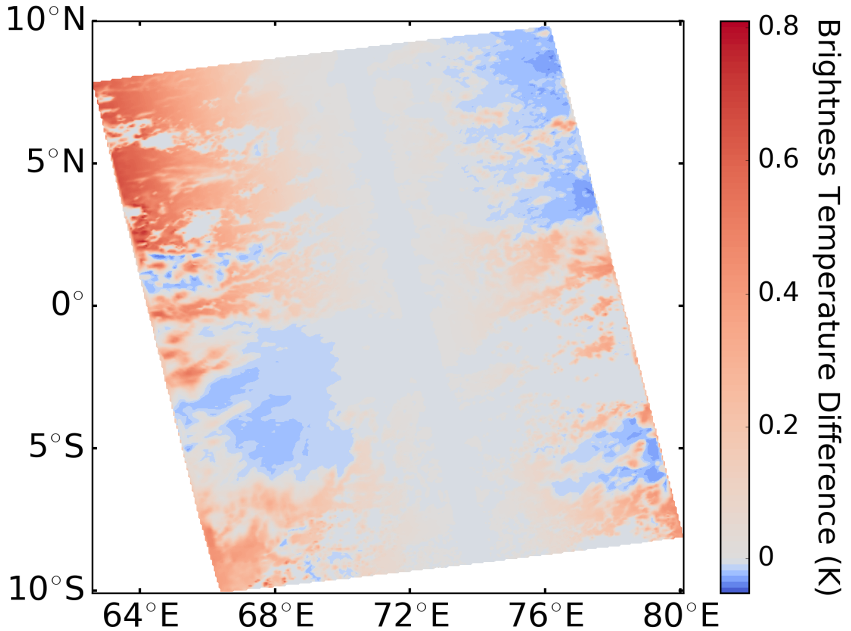

Figure 39 Simulated MODIS band 31 (10.78~11.28 μm) brightness temperature difference (BTD) for the region in Fig. 30.

7.4 Discussions

The differences between the observation and simulation are attributed to errors in calculation and uncertainties of the input data. The developed RTM is based on the plane-parallel assumption so earth curvature and cloud 3D effects are ignored in the calculation. Also, all calculations are channel-averaged. Even though the spectral bands considered in the simulation are narrow, the channel-averaged RT calculation still introduces some errors compared with the monochromatic counterpart. These assumptions and approximations affect the accuracy of all computational modules of the model. Each module also has additional local error factors.

In the gas absorption calculation, the regression method has regression error. The atmosphere is divided into a finite number of homogeneous layers. The discretization may introduce some errors. The pressure levels are fixed in the model, and the input atmospheric profiles are interpolated onto the model pressure levels, which adds interpolation errors in the calculation.

In the multiple scattering calculation, the two-component (SAA+AD) method is an approximation so it has errors compared with numerically accurate RTE solvers. Errors also exist in the ocean surface reflectance calculation, because the air-sea interface model is a simple approximation of the complicated real interface.

In the thermal emission calculation, the assumption that the Planck function changes linearly from the cloud base to top may introduce errors, especially for an optically thick cloud. As shown in Figs. 37 and 38, the simulated thermal emissions by optically thick clouds have larger biases than optically thin clouds. The errors in the absorption calculation also propagate into the air thermal emission calculation. All thermal emission calculations assume local thermal equilibrium (LTE) in the atmosphere. The LTE assumption is valid if the density of the atmospheric gases is large. However, in the upper atmosphere, the gas density may not be large enough to make the LTE assumption valid (Lópeze-Puertas and Taylor 2001). The invalid LTE assumption also introduces errors in thermal emission calculations in the upper atmosphere.

The input cloud properties and atmospheric profiles in the simulations are all obtained from retrievals and data assimilation. The input data have uncertainties compared with exact atmospheric properties. The atmospheric profile data have lower spatial and temporal resolution than the MODIS and POLDER data. Interpolation is used to obtain atmospheric profiles at each specific pixel location and time. The interpolation error increases the uncertainties of input data.

The comparison between observation and simulation using a single satellite scene may not be enough to prove the global accuracy of the developed RTM. It can only show that the RTM can work as a simulator in a retrieval algorithm. The efficiency of implementation is another big concern. The number of pixels in the calculation is over 50,000. The reflectance and polarized reflectance calculations take less than one hour with one core on the TAMU Ada supercomputer. The thermal emission calculation is even faster.

CHAPTER VIII

SUMMARY

In this dissertation, a fast vector RTM is developed in support of polarimetric remote sensing of atmospheric and oceanic properties. The RTM can serve as an in-line forward model in a retrieval algorithm to fulfill the accuracy and efficiency requirements of the algorithm implementation. The RTM has three main components: a gas absorption calculation module, a vector RTE solver, and an ocean module.

The gas absorption module computes the channel-averaged atmospheric gas transmittance. The gas transmittance is the input to the vector RTE solver. A regression-based method is applied to parameterize the CAOT versus atmospheric variables such as pressure, temperature and gas concentration, and zenith angle. Compared with traditional regression-based methods that carry out regression in each homogeneous layer, the current method takes multiple homogeneous layers as one and only employs one parameterization, which significantly reduces the computational time. The CAOT is found to be a smooth and monotonic function of the weighted sum of gas concentration in different layers. The weights are functions of pressure and temperature. Because a gas absorption property depends on gas types and wavelengths, the CAOTs of various gases are parameterized separately in each channel and then added up. The regression equation is constructed as a polynomial function of the weighted sum of the gas concentrations. An LBLRTM is used to compute the CAOTs for each gas in each channel for an atmospheric profile dataset. Then, a numerically stable SVD is applied to solve the regression equations to obtain the regression coefficients. The regression method is implemented in 36 MODIS bands and a hyperspectral spectrum from UV to NIR bands. The RMSE of the transmittance compared with LBLRTM results is as small as 0.005 for most channels. The developed regression method is over 4 orders of magnitude faster than LBLRTM.

The vector RTE solver assumes both an incident solar source and an atmospheric thermal emission source. A two-component (SAA+AD) method is utilized to solve the vector RTE. The anisotropic scattering matrix of atmospheric and oceanic particles is decomposed into forward and diffuse components. The forward component is nonzero only in a small range of angles. The diffuse component is much more isotropic. The Stokes vector of the RTE solution is also expressed as a sum of forward and diffuse components. After some approximations, we obtain decoupled forward and diffuse RTEs. The forward RTE is solved by the SAA method, in which the forward solution is approximated as a two-dimensional Gaussian function. The SAA method in this study is generalized to multi-layer cases so it can be applied to the calculation involving an inhomogeneous medium. The diffuse RTE is solved by the AD method. The forward Stokes vector computation with SAA is quite fast because the solution is an approximate analytical equation. The AD computation is substantially accelerated due to the fact that the diffuse scattering matrix can be expanded with a much lower order of the GSF. The two-component (SAA+AD) method is more than 3 orders of magnitude faster than the rigorous AD method.

In thermal infrared and microwave bands, thermal emission from the atmosphere and terrestrial surface has a nontrivial contribution to the observed radiation. The thermal emission by the air can be computed if we know the gas transmittances and temperature profiles. Thermal emission by clouds and aerosols experiences multiple scattering. An efficient thermal emission calculation method with multiple scattering is developed based on the AD method. In the RTE with only a thermal emission source, the source function is the Planck function, which is dependent on temperature. In the atmosphere, layer optical properties may be homogeneous, but the vertical temperature varies. The adding process can be used to compute thermal emission by a scattering medium. For a scattering layer with homogeneous optical properties, it is preferable to use the doubling process since it is more efficient than the adding process. In this study, the source function in the RTE is approximated by a linear profile with respect to altitude in a homogenous cloud. The layer top and bottom temperatures are the boundary conditions. Based on this approximation, a doubling process can be utilized to compute the thermal emission by the homogeneous layer, which is much faster than directly adding the inhomogeneous thermal emission from each thin layer.

The ocean module includes an air-sea interface model and an ocean IOP model. A beam incident on the interface experiences reflection and transmission. The reflection and transmission properties of the ocean are determined by the interface morphology and the ocean optical properties. The interface is assumed to be a wind-ruffled rough surface composed of infinite hypothetic small facets. The orientation slopes of the facets follow a 2-dimensional Gaussian distribution whose variance is determined by wind speed, which is consistent with the Cox and Munk model. The reflection and transmission matrices are computed based on the rough interface assumption, and these matrices are directly incorporated into the RTE solver as boundary conditions. The ocean is assumed to be a homogeneous layer in the model. The ocean IOPs include scattering and absorption properties of pure water, phytoplankton, NAP and CDOM. The scattering and absorption coefficients are obtained from measurements and bio-optical models in published studies. The Rayleigh scattering matrix is adopted as the pure water scattering matrix. An ensemble-averaged irregular hexahedron model is assumed to represent phytoplankton and associated NAP shapes to compute a scattering matrix.

As illustrations, the developed RTM is used to simulate the reflectance and polarized reflectance from POLDER observations, and radiance from MODIS observations. In general, the simulation results are comparable to the observations. The errors in the approximations of the RTM and the uncertainties of the input data can explain the differences between the simulations and observations.

Further development is needed to improve the RTM in both accuracy and efficiency aspects. Although the RTM is based on a plane-parallel assumption, the gas absorption calculation could be modified to consider earth curvature without reducing computational speed. For thermal emission calculations in the upper atmosphere, non-LTE radiative transfer can be applied to reduce the error of the current LTE assumption in the upper atmosphere. The two-component (SAA+AD) vector RTE solver is the most time-consuming part of the model. More approximations may be introduced to improve the efficiency of the vector RTE solver such as using the discretization scheme of the 4π solid angle in evaluating the solid angle integration (Wang et al. 2013). In addition, the RTM only considers an ice-free ocean as the lower boundary. The RTM should incorporate a land reflection matrix model to be able to do calculations over a land surface with various conditions.

REFERENCES

Aumann, H. H. and Coauthors, 2003: AIRS/AMSU/HSB on the Aqua mission: Design, science objectives, data products, and processing systems. *IEEE Trans. Geosci. Remote Sens.*, **41**, 253–264, doi:10.1109/TGRS.2002.808356. http://ieeexplore.ieee.org/document/1196043/.

Bernstein, L. S., A. Berk, P. K. Acharya, D. C. Robertson, G. P. Anderson, J. H. Chetwynd, and L. M. Kimball, 1996: Very narrow band model calculations of atmospheric fluxes and cooling rates. *J. Atmos. Sci.*, **53**, 2887–2904, doi:10.1175/1520-0469(1996)053<2887:VNBMCO>2.0.CO;2. http://journals.ametsoc.org/doi/abs/10.1175/1520-0469%281996%29053%3C2887%3AVNBMCO%3E2.0.CO%3B2.

Bi, L. and P. Yang, 2014: Accurate simulation of the optical properties of atmospheric ice crystals with the invariant imbedding T-matrix method. *J. Quant. Spectrosc. Radiat. Transf.*, **138**, 17–35, doi:10.1016/j.jqsrt.2014.01.013. http://dx.doi.org/10.1016/j.jqsrt.2014.01.013.

Bodhaine, B. A., N. B. Wood, E. G. Dutton, and J. R. Slusser, 1999: On Rayleigh optical depth calculations. *J. Atmos. Ocean. Technol.*, **16**, 1854–1861, doi:10.1175/1520-0426(1999)016<1854:ORODC>2.0.CO;2. http://journals.ametsoc.org/doi/abs/10.1175/1520-0426%281999%29016%3C1854%3AORODC%3E2.0.CO%3B2.

Borbas, E. E., S. W. Seemann, H.-L. Huang, J. Li, and W. P. Menzel, 2005: Global profile training database for satellite regression retrievals with estimates of skin temperature and emissivity. *Proc. XIV. Int. ATOVS Study Conf.*, 763–770. http://library.ssec.wisc.edu/publications/pdfs/ITSC14/borbas02_ITSC14_2005.pdf.

Bricaud, A., M. Babin, A. Morel, and H. Claustre, 1995: Variability in the chlorophyll-specific absorption coefficients of natural phytoplankton: Analysis and parameterization. *J. Geophys. Res.*, **100**, 13321, doi:10.1029/95JC00463. http://doi.wiley.com/10.1029/95JC00463.

Bricaud, A., A. Morel, M. Babin, K. Allali, and H. Claustre, 1998: Variations of light absorption by suspended particles with chlorophyll a concentration in oceanic (case 1) waters: Analysis and implications for bio-optical models. *J. Geophys. Res. Ocean.*, **103**, 31033–31044, doi:10.1029/98JC02712. http://doi.wiley.com/10.1029/98JC02712.

Bricaud, A., A. Morel, and L. Prieur, 1981: Absorption by dissolved organic matter of the sea (yellow substance) in the UV and visible domains. *Limnol. Oceanogr.*, **26**, 43–53, doi:10.4319/lo.1981.26.1.0043. http://doi.wiley.com/10.4319/lo.1981.26.1.0043.

Cao, C., F. J. De Luccia, X. Xiong, R. Wolfe, and F. Weng, 2014: Early on-orbit performance of the visible infrared imaging radiometer suite onboard the Suomi National Polar-Orbiting Partnership (S-NPP) satellite. *IEEE Trans. Geosci. Remote Sens.*, **52**, 1142–1156, doi:10.1109/TGRS.2013.2247768. http://ieeexplore.ieee.org/document/6522157/.

Chami, M., B. Lafrance, B. Fougnie, J. Chowdhary, T. Harmel, and F. Waquet, 2015: OSOAA: A vector radiative transfer model of coupled atmosphere-ocean system for a rough sea surface application to the estimates of the directional variations of the water leaving reflectance to better process multi-angular satellite sensors data over the ocean. *Opt. Express*, **23**, 27829, doi:10.1364/OE.23.027829. https://www.osapublishing.org/abstract.cfm?URI=oe-23-21-27829.

Chandrasekhar, S., 1960: *Radiative transfer*. Dover Publication, Inc., New York.

Chou, M.-D. and A. Arking, 1980: Computation of infrared cooling rates in the water vapor bands. *J. Atmos. Sci.*, **37**, 855–867, doi:10.1175/1520-0469(1980)037<0855:COICRI>2.0.CO;2. http://journals.ametsoc.org/doi/abs/10.1175/1520-0469%281980%29037%3C0855%3ACOICRI%3E2.0.CO%3B2.

Chowdhary, J., B. Cairns, and L. D. Travis, 2006: Contribution of water-leaving radiances to multiangle, multispectral polarimetric observations over the open ocean: Bio-optical model results for case 1 waters. *Appl. Opt.*, **45**, 5542, doi:10.1364/AO.45.005542. https://www.osapublishing.org/abstract.cfm?URI=ao-45-22-5542.

Chowdhary, J., B. Cairns, F. Waquet, K. Knobelspiesse, M. Ottaviani, J. Redemann, L. Travis, and M. Mishchenko, 2012: Sensitivity of multiangle, multispectral polarimetric remote sensing over open oceans to water-leaving radiance: Analyses of RSP data acquired during the MILAGRO campaign. *Remote Sens. Environ.*, **118**, 284–308, doi:10.1016/j.rse.2011.11.003. http://dx.doi.org/10.1016/j.rse.2011.11.003.

Clough, S. A., M. W. Shephard, E. J. Mlawer, J. S. Delamere, M. J. Iacono, K. Cady-Pereira, S. Boukabara, and P. D. Brown, 2005: Atmospheric radiative transfer modeling: A summary of the AER codes. *J. Quant. Spectrosc. Radiat. Transf.*, **91**, 233–244, doi:10.1016/j.jqsrt.2004.05.058. https://linkinghub.elsevier.com/retrieve/pii/S0022407304002158.

Cox, C. and W. Munk, 1954: Measurement of the roughness of the sea surface from photographs of the sun's glitter. *J. Opt. Soc. Am.*, **44**, 838, doi:10.1364/JOSA.44.000838. https://www.osapublishing.org/abstract.cfm?URI=josa-44-11-838.

Cureton, G. P., 2015: Retrieval of higher order ocean spectral information from sunglint. *IEEE Trans. Geosci. Remote Sens.*, **53**, 36–50, doi:10.1109/TGRS.2014.2317477. http://ieeexplore.ieee.org/document/6866877/.

Curtis, A. R., 1952: Discussion of a statistical model for water-vapour absorption. *Q. J. R. Meteorol. Soc.*, **78**, 165–169, doi:10.1002/qj.49707833604. http://doi.wiley.com/10.1002/qj.49707833820.

da Silva, A. and Coauthors, 2016: *ACE 2011-2015 progress report and future outlook.* https://acemission.gsfc.nasa.gov/documents/ACE_5YWP-FINAL_Redacted.pdf

de Haan, J. F., P. B. Bosma, and J. W. Hovenier, 1987: The adding method for multiple scattering calculations of polarized light. *Astron. Astrophys.*, **183**, 371–391. http://adsabs.harvard.edu/full/1987A%26A...183..371D

Deschamps, P. Y., J. C. Buriez, F. M. Bréon, M. Leroy, A. Podaire, A. Bricaud, and G. Sèze, 1994: The POLDER mission: Instrument characteristics and scientific objectives. *IEEE Trans. Geosci. Remote Sens.*, **32**, 598–615, doi:10.1109/36.297978. http://ieeexplore.ieee.org/document/297978/.

Diner, D. J. and Coauthors, 2013: The Airborne Multiangle SpectroPolarimetric Imager (AirMSPI): A new tool for aerosol and cloud remote sensing. *Atmos. Meas. Tech.*, **6**, 2007–2025, doi:10.5194/amt-6-2007-2013. https://www.atmos-meas-tech.net/6/2007/2013/.

Draper, D. W., D. A. Newell, F. J. Wentz, S. Krimchansky, and G. M. Skofronick-Jackson, 2015: The Global Precipitation Measurement (GPM) Microwave Imager (GMI): Instrument overview and early on-orbit performance. *IEEE J. Sel. Top. Appl. Earth Obs. Remote Sens.*, **8**, 3452–3462, doi:10.1109/JSTARS.2015.2403303. http://ieeexplore.ieee.org/document/7052302/.

Dubovik, O., and Coauthors, 2011: Statistically optimized inversion algorithm for enhanced retrieval of aerosol properties from spectral multi-angle polarimetric satellite observations. *Atmos. Meas. Tech.*, **4**, 975–1018, doi:10.5194/amt-4-975-2011. http://www.atmos-meas-tech.net/4/975/2011/.

Edwards, D. P. and G. L. Francis, 2000: Improvements to the correlated- k radiative transfer method: Application to satellite infrared sounding. *J. Geophys. Res. Atmos.*, **105**, 18135–18156, doi:10.1029/2000JD900131. http://doi.wiley.com/10.1029/2000JD900131.

Emde, C., R. Buras, and B. Mayer, 2011: ALIS: An efficient method to compute high spectral resolution polarized solar radiances using the Monte Carlo approach. *J. Quant. Spectrosc. Radiat. Transf.*, **112**, 1622–1631, doi:10.1016/j.jqsrt.2011.03.018. http://dx.doi.org/10.1016/j.jqsrt.2011.03.018.

Evans, K. F., J. R. Wang, P. E. Racette, G. Heymsfield, and L. Li, 2005: Ice cloud retrievals and analysis with the Compact Scanning Submillimeter Imaging Radiometer and the Cloud Radar System during CRYSTAL FACE. *J. Appl. Meteorol.*, **44**, 839–859, doi:10.1175/JAM2250.1. http://journals.ametsoc.org/doi/abs/10.1175/JAM2250.1.

Evans, K. F. and G. L. Stephens, 1991: A new polarized atmospheric radiative transfer model. *J. Quant. Spectrosc. Radiat. Transf.*, **46**, 413–423, doi:10.1016/0022-4073(91)90043-P. http://linkinghub.elsevier.com/retrieve/pii/002240739190043P.

Fougnie, B., G. Bracco, B. Lafrance, C. Ruffel, O. Hagolle, and C. Tinel, 2007: PARASOL in-flight calibration and performance. *Appl. Opt.*, **46**, 5435, doi:10.1364/AO.46.005435. https://www.osapublishing.org/abstract.cfm?URI=ao-46-22-5435.

Fu, Q. and K. N. Liou, 1992a: A three-parameter approximation for radiative transfer in nonhomogeneous atmospheres: Application to the O3 9.6-µm band. *J. Geophys. Res.*, **97**, 13051, doi:10.1029/92JD00999. http://doi.wiley.com/10.1029/92JD00999.

Fu, Q. and K. N. Liou, 1992b: On the correlated k -distribution method for radiative transfer in nonhomogeneous atmospheres. *J. Atmos. Sci.*, **49**, 2139–2156, doi:10.1175/1520-0469(1992)049<2139:OTCDMF>2.0.CO;2. http://journals.ametsoc.org/doi/abs/10.1175/1520-0469%281992%29049%3C2139%3AOTCDMF%3E2.0.CO%3B2.

Gelaro, R. and Coauthors, 2017: The Modern-Era Retrospective Analysis for Research and Applications, Version 2 (MERRA-2). *J. Clim.*, **30**, 5419–5454, doi:10.1175/JCLI-D-16-0758.1. http://journals.ametsoc.org/doi/10.1175/JCLI-D-16-0758.1.

Godson, W. L., 1953: The evaluation of infra-red radiative fluxes due to atmospheric water vapour. *Q. J. R. Meteorol. Soc.*, **79**, 367–379, doi:10.1002/qj.49707934104. http://doi.wiley.com/10.1002/qj.49707934104.

Gong, J. and D. L. Wu, 2017: Microphysical properties of frozen particles inferred from Global Precipitation Measurement (GPM) Microwave Imager (GMI) polarimetric measurements. *Atmos. Chem. Phys.*, **17**, 2741–2757, doi:10.5194/acp-17-2741-2017. https://www.atmos-chem-phys.net/17/2741/2017/.

Gong, J., X. Zeng, D. L. Wu, and X. Li, 2018: Diurnal variation of tropical ice cloud microphysics: Evidence from Global Precipitation Measurement Microwave Imager polarimetric measurements. *Geophys. Res. Lett.*, **45**, 1185–1193, doi:10.1002/2017GL075519. http://doi.wiley.com/10.1002/2017GL075519.

Goody, R. M., 1952: A statistical model for water-vapour absorption. *Q. J. R. Meteorol. Soc.*, **78**, 165–169, doi:10.1002/qj.49707833604. http://doi.wiley.com/10.1002/qj.49707833604.

Goody, R., R. West, L. Chen, and D. Crisp, 1989: The correlated-k method for radiation calculations in nonhomogeneous atmospheres. *J. Quant. Spectrosc. Radiat. Transf.*, **42**, 539–550, doi:10.1016/0022-4073(89)90044-7. http://linkinghub.elsevier.com/retrieve/pii/0022407389900447.

Han, Y., P. van Delst, Q. Liu, F. Weng, B. Yan, R. Treadon, and J. Derber 2006: JCSDA community radiative transfer model (CRTM)—version 1, *NOAA Tech. Rep.*, 122 pp., NOAA, Washington, D. C. https://repository.library.noaa.gov/view/noaa/1157.

He, X., Y. Bai, Q. Zhu, and F. Gong, 2010: A vector radiative transfer model of coupled ocean-atmosphere system using matrix-operator method for rough sea-surface. *J. Quant. Spectrosc. Radiat. Transf.*, **111**, 1426–1448, doi:10.1016/j.jqsrt.2010.02.014. http://dx.doi.org/10.1016/j.jqsrt.2010.02.014.

Heidinger, A. K., C. O'Dell, R. Bennartz, and T. Greenwald, 2006: The successive-order-of-interaction radiative transfer model. Part I: Model development. *J. Appl. Meteorol. Climatol.*, **45**, 1388–1402, doi:10.1175/JAM2387.1. http://journals.ametsoc.org/doi/abs/10.1175/JAM2387.1.

Hioki, S., P. Yang, G. W. Kattawar, and Y. Hu, 2016: Truncation of the scattering phase matrix for vector radiative transfer simulation. *J. Quant. Spectrosc. Radiat. Transf.*, **183**, 70–77, doi:10.1016/j.jqsrt.2016.06.011. http://dx.doi.org/10.1016/j.jqsrt.2016.06.011.

Hovenier, J. W., C. Van Der Mee, and H. Domke, 2004: *Transfer of polarized light in planetary atmospheres: Basic concepts and practical methods*. Kluwer Academic Publishers, Dordrecht, Netherlands.

Hu, Y.-X., B. Wielicki, B. Lin, G. Gibson, S.-C. Tsay, K. Stamnes, and T. Wong, 2000: δ-Fit: A fast and accurate treatment of particle scattering phase functions with weighted singular-value decomposition least-squares fitting. *J. Quant. Spectrosc. Radiat. Transf.*, **65**, 681–690, doi:10.1016/S0022-4073(99)00147-8. http://linkinghub.elsevier.com/retrieve/pii/S0022407399001478.

Huang, X., P. Yang, G. Kattawar, and K.-N. Liou, 2015: Effect of mineral dust aerosol aspect ratio on polarized reflectance. *J. Quant. Spectrosc. Radiat. Transf.*, **151**, 97–109, doi:10.1016/j.jqsrt.2014.09.014. http://dx.doi.org/10.1016/j.jqsrt.2014.09.014.

Huot, Y., A. Morel, M. S. Twardowski, D. Stramski, and R. A. Reynolds, 2008: Particle optical backscattering along a chlorophyll gradient in the upper layer of the eastern South Pacific Ocean. *Biogeosciences*, **5**, 495–507, doi:10.5194/bg-5-495-2008. http://www.biogeosciences.net/5/495/2008/.

Iwabuchi, H., 2006: Efficient Monte Carlo methods for radiative transfer modeling. *J. Atmos. Sci.*, **63**, 2324–2339, doi:10.1175/JAS3755.1. http://journals.ametsoc.org/doi/abs/10.1175/JAS3755.1.

Kattawar, G. W., G. N. Plass, and S. J. Hitzfelder, 1976: Multiple scattered radiation emerging from Rayleigh and continental haze layers 1: Radiance, polarization, and neutral points. *Appl. Opt.*, **15**, 632, doi:10.1364/AO.15.000632. https://www.osapublishing.org/abstract.cfm?URI=ao-15-3-632.

Kattawar, G. W. and C. N. Adams, 1989: Stokes vector calculations of the submarine light field in an atmosphere-ocean with scattering according to a Rayleigh phase matrix: Effect of interface refractive index on radiance and polarization. *Limnol. Oceanogr.*, **34**, 1453–1472, doi:10.4319/lo.1989.34.8.1453. http://doi.wiley.com/10.4319/lo.1989.34.8.1453.

Kaufman, Y. J., J. V. Martins, L. A. Remer, M. R. Schoeberl, and M. A. Yamasoe, 2002: Satellite retrieval of aerosol absorption over the oceans using sunglint. *Geophys. Res. Lett.*, **29**, 34-1-34–4, doi:10.1029/2002GL015403. http://doi.wiley.com/10.1029/2002GL015403.

Kawanishi, T. and Coauthors, 2003: The Advanced Microwave Scanning Radiometer for the Earth Observing System (AMSR-E), NASDA's contribution to the EOS for global energy and water cycle studies. *IEEE Trans. Geosci. Remote Sens.*, **41**, 184–194, doi:10.1109/TGRS.2002.808331. http://ieeexplore.ieee.org/document/1196037/.

King, M. D., Y. J. Kaufman, W. P. Menzel, and D. Tanre, 1992: Remote sensing of cloud, aerosol, and water vapor properties from the Moderate Resolution Imaging Spectrometer (MODIS). *IEEE Trans. Geosci. Remote Sens.*, **30**, 2–27, doi:10.1109/36.124212. http://ieeexplore.ieee.org/document/124212/.

Kokhanovsky, A. A. and Coauthors, 2010: Benchmark results in vector atmospheric radiative transfer. *J. Quant. Spectrosc. Radiat. Transf.*, **111**, 1931–1946, doi:10.1016/j.jqsrt.2010.03.005. http://dx.doi.org/10.1016/j.jqsrt.2010.03.005.

Lacis, A. A., J. Chowdhary, M. I. Mishchenko, and B. Cairns, 1998: Modeling errors in diffuse-sky radiation: Vector vs scalar treatment. *Geophys. Res. Lett.*, **25**, 135–138, doi:10.1029/97GL03613. http://doi.wiley.com/10.1029/97GL03613.

Lacis, A. A., W. Wang, and J. E. Hansen, 1979: Correlated k-distribution method for radiative transfer in climate models: Application to effect of cirrus clouds on climate. *NASA. Goddard Space Flight Center 4th NASA Weather and Climate Program Sci. Rev*, 309–314. https://ntrs.nasa.gov/archive/nasa/casi.ntrs.nasa.gov/19790012513.pdf.

Lenoble, J., M. Herman, J. L. Deuzé, B. Lafrance, R. Santer, and D. Tanré, 2007: A successive order of scattering code for solving the vector equation of transfer in the earth's atmosphere with aerosols. *J. Quant. Spectrosc. Radiat. Transf.*, **107**, 479–507, doi:10.1016/j.jqsrt.2007.03.010. https://linkinghub.elsevier.com/retrieve/pii/S0022407307001306.

Liou, K.-N., 2002: *An introduction to atmospheric radiation*. Academic Press, San Diego, CA.

Liu, C., P. Yang, S. L. Nasiri, S. Platnick, K. G. Meyer, C. Wang, and S. Ding, 2015: A fast Visible Infrared Imaging Radiometer Suite simulator for cloudy atmospheres. *J. Geophys. Res. Atmos.*, **120**, 240–255, doi:10.1002/2014JD022443. http://doi.wiley.com/10.1002/2014JD022443.

Liu, Q., and F. Weng, 2006: Advanced Doubling–Adding method for radiative transfer in planetary atmospheres. *J. Atmos. Sci.*, **63**, 3459–3465, doi:10.1175/JAS3808.1. http://journals.ametsoc.org/doi/abs/10.1175/JAS3808.1.

Liu, X., W. L. Smith, D. K. Zhou, and A. Larar, 2006: Principal component-based radiative transfer model for hyperspectral sensors: theoretical concept. *Appl. Opt.*, **45**, 201, doi:10.1364/AO.45.000201. https://www.osapublishing.org/abstract.cfm?URI=ao-45-1-201.

Liu, X., Q. Yang, H. Li, Z. Jin, W. Wu, S. Kizer, D. K. Zhou, and P. Yang, 2016: Development of a fast and accurate PCRTM radiative transfer model in the solar spectral region. *Appl. Opt.*, **55**, 8236, doi:10.1364/AO.55.008236. https://www.osapublishing.org/abstract.cfm?URI=ao-55-29-8236.

Liu, Y. and D. J. Diner, 2017: Multi-Angle Imager for Aerosols. *Public Health Rep.*, **132**, 14–17, doi:10.1177/0033354916679983. http://journals.sagepub.com/doi/10.1177/0033354916679983.

Loisel, H. and A. Morel, 1998: Light scattering and chlorophyll concentration in case 1 waters: A reexamination. *Limnol. Oceanogr.*, **43**, 847–858, doi:10.4319/lo.1998.43.5.0847. http://doi.wiley.com/10.4319/lo.1998.43.5.0847.

López-Puertas, M. and F. W. Taylor, 2001: *Non-LTE radiative transfer in the atmosphere*. World Scientific Publishing, Singapore.

Lu, Y. and Coauthors, 2017: Using remote sensing to detect the polarized sunglint reflected from oil slicks beyond the critical angle. *J. Geophys. Res. Ocean.*, **122**, 6342–6354, doi:10.1002/2017JC012793. http://doi.wiley.com/10.1002/2017JC012793.

Malkmus, W., 1967: Random Lorentz band model with exponential-tailed S\^-1 line-intensity distribution function. *J. Opt. Soc. Am.*, **57**, 323–329, doi:10.1364/JOSA.57.000323. http://www.opticsinfobase.org/abstract.cfm?URI=josa-57-3-323.

Marbach, T., J. Riedi, A. Lacan, and P. Schlüssel, 2015: The 3MI mission: Multi-viewing-channel-polarisation imager of the EUMETSAT polar system: Second generation (EPS-SG) dedicated to aerosol and cloud monitoring. Proc. SPIE 9613, *Polarization Science and Remote Sensing VII*, 1-8, doi: 10.1117/12.2186978. http://proceedings.spiedigitallibrary.org/proceeding.aspx?doi=10.1117/12.2186978.

Matricardi, M. and R. Saunders, 1999: Fast radiative transfer model for simulation of infrared atmospheric sounding interferometer radiances. *Appl. Opt.*, **38**, 5679, doi:10.1364/AO.38.005679. https://www.osapublishing.org/abstract.cfm?URI=ao-38-27-5679.

McMillin, L. M., L. J. Crone, and T. J. Kleespies, 1995: Atmospheric transmittance of an absorbing gas 5 Improvements to the OPTRAN approach. *Appl. Opt.*, **34**, 8396, doi:10.1364/AO.34.008396. https://www.osapublishing.org/abstract.cfm?URI=ao-34-36-8396.

Min, Q. and M. Duan, 2004: A successive order of scattering model for solving vector radiative transfer in the atmosphere. *J. Quant. Spectrosc. Radiat. Transf.*, **87**, 243–259, doi:10.1016/j.jqsrt.2003.12.019. https://linkinghub.elsevier.com/retrieve/pii/S0022407303003911.

Mishchenko, M. I. and L. D. Travis, 1997: Satellite retrieval of aerosol properties over the ocean using polarization as well as intensity of reflected sunlight. *J. Geophys. Res. Atmos.*, **102**, 16989–17013, doi:10.1029/96JD02425. http://doi.wiley.com/10.1029/96JD02425.

Mobley, C. D., 1994: *Light and water: Radiative transfer in natural waters*. Academic Press, San Diego, CA.

Moncet, J.-L., G. Uymin, A. E. Lipton, and H. E. Snell, 2008: Infrared radiance modeling by optimal spectral sampling. *J. Atmos. Sci.*, **65**, 3917–3934, doi:10.1175/2008JAS2711.1. http://journals.ametsoc.org/doi/abs/10.1175/2008JAS2711.1.

Morel, A. and L. Prieur, 1977: Analysis of variations in ocean color 1. *Limnol. Oceanogr.*, **22**, 709–722, doi:10.4319/lo.1977.22.4.0709. http://doi.wiley.com/10.4319/lo.1977.22.4.0709.

Morel, A. and S. Maritorena, 2001: Bio-optical properties of oceanic waters: A reappraisal. *J. Geophys. Res. Ocean.*, **106**, 7163–7180, doi:10.1029/2000JC000319. http://doi.wiley.com/10.1029/2000JC000319.

Nakajima, T. and M. Tanaka, 1988: Algorithms for radiative intensity calculations in moderately thick atmospheres using a truncation approximation. *J. Quant. Spectrosc. Radiat. Transf.*, **40**, 51–69, doi:10.1016/0022-4073(88)90031-3. http://linkinghub.elsevier.com/retrieve/pii/0022407388900313.

National Academies of Sciences, Engineering, and Medicine, 2018: *Thriving on our changing planet: A decadal strategy for earth observation from space*. The National Academies Press, Washington, DC., https://doi.org.10.17226/24938.

Ota, Y., A. Higurashi, T. Nakajima, and T. Yokota, 2010: Matrix formulations of radiative transfer including the polarization effect in a coupled atmosphere–ocean system. *J. Quant. Spectrosc. Radiat. Transf.*, **111**, 878–894, doi:10.1016/j.jqsrt.2009.11.021. http://dx.doi.org/10.1016/j.jqsrt.2009.11.021.

Ottaviani, M., K. Knobelspiesse, B. Cairns, and M. Mishchenko, 2013: Information content of aerosol retrievals in the sunglint region. *Geophys. Res. Lett.*, **40**, 631–634, doi:10.1002/grl.50148. http://doi.wiley.com/10.1002/grl.50148.

PACE Technical Report Series, 2018: *Pre-Aerosol, Clouds, and ocean Ecosystem (PACE) mission science definition team report*. http://www.sti.nasa.gov.

Parol, F. and Coauthors, 2004: Review of capabilities of multi-angle and polarization cloud measurements from POLDER. *Adv. Sp. Res.*, **33**, 1080–1088, doi:10.1016/S0273-1177(03)00734-8. https://linkinghub.elsevier.com/retrieve/pii/S0273117703007348.

Platnick, S. and Coauthors, 2017: The MODIS cloud optical and microphysical products: Collection 6 updates and examples from Terra and Aqua. *IEEE Trans. Geosci. Remote Sens.*, **55**, 502–525, doi:10.1109/TGRS.2016.2610522. http://ieeexplore.ieee.org/document/7707459/.

Pope, R. M. and E. S. Fry, 1997: Absorption spectrum (380–700 nm) of pure water II Integrating cavity measurements. *Appl. Opt.*, **36**, 8710, doi:10.1364/AO.36.008710. https://www.osapublishing.org/abstract.cfm?URI=ao-36-33-8710.

Potter, J. F., 1970: The Delta function approximation in radiative transfer theory. *J. Atmos. Sci.*, **27**, 943–949, doi:10.1175/1520-0469(1970)027<0943:TDFAIR>2.0.CO;2.

http://journals.ametsoc.org/doi/abs/10.1175/1520-0469%281970%29027%3C0943%3ATDFAIR%3E2.0.CO%3B2.

Rozanov, V. V. and A. A. Kokhanovsky, 2006: The solution of the vector radiative transfer equation using the discrete ordinates technique: Selected applications. *Atmos. Res.*, **79**, 241–265, doi:10.1016/j.atmosres.2005.06.006. https://linkinghub.elsevier.com/retrieve/pii/S0169809505001584.

Sancer, M., 1969: Shadow-corrected electromagnetic scattering from a randomly rough surface. *IEEE Trans. Antennas Propag.*, **17**, 577–585, doi:10.1109/TAP.1969.1139516. http://ieeexplore.ieee.org/document/1139516/.

Sanghavi, S. and G. Stephens, 2015: Adaptation of the delta- m and δ -fit truncation methods to vector radiative transfer: Effect of truncation on radiative transfer accuracy. *J. Quant. Spectrosc. Radiat. Transf.*, **159**, 53–68, doi:10.1016/j.jqsrt.2015.03.007. http://dx.doi.org/10.1016/j.jqsrt.2015.03.007.

Schwenger, F. and E. Repasi, 2003: Sea surface simulation for testing of multiband imaging sensors. Proc. SPIE 5075, *Targets and Backgrounds IX: Characterization and Representation*, 72-84, doi: 10.1117/12.488472. http://proceedings.spiedigitallibrary.org/proceeding.aspx?doi=10.1117/12.488472.

Siewert, C. E., 2000: A discrete-ordinates solution for radiative-transfer models that include polarization effects. *J. Quant. Spectrosc. Radiat. Transf.*, **64**, 227–254, doi:10.1016/S0022-4073(99)00006-0. http://linkinghub.elsevier.com/retrieve/pii/S0022407399000060.

Smith, B., 1967: Geometrical shadowing of a random rough surface. *IEEE Trans. Antennas Propag.*, **15**, 668–671, doi:10.1109/TAP.1967.1138991. http://ieeexplore.ieee.org/document/1138991/.

Spurr, R. J. D., 2006: VLIDORT: A linearized pseudo-spherical vector discrete ordinate radiative transfer code for forward model and retrieval studies in multilayer multiple scattering media. *J. Quant. Spectrosc. Radiat. Transf.*, **102**, 316–342, doi:10.1016/j.jqsrt.2006.05.005. https://linkinghub.elsevier.com/retrieve/pii/S0022407306001191.

Stamnes, K., S.-C. Tsay, W. Wiscombe, and K. Jayaweera, 1988: Numerically stable algorithm for discrete-ordinate-method radiative transfer in multiple scattering and emitting layered media. *Appl. Opt.*, **27**, 2502, doi:10.1364/AO.27.002502. https://www.osapublishing.org/abstract.cfm?URI=ao-27-12-2502.

Stegmann, P. G. and P. Yang, 2017: A regional, size-dependent, and causal effective medium model for Asian and Saharan mineral dust refractive index spectra. *J. Aerosol*

Sci., **114**, 327–341, doi:10.1016/j.jaerosci.2017.10.003. https://linkinghub.elsevier.com/retrieve/pii/S002185021730071X.

Stephens, G. L. and Coauthors, 2002: The CloudSat mission and the A-Train: A new dimension of space-based observations of clouds and precipitation. *Bull. Am. Meteorol. Soc.*, **83**, 1771–1790+1742, doi:10.1175/BAMS-83-12-1771. http://journals.ametsoc.org/doi/10.1175/BAMS-83-12-1771.

Strow, L. L., S. E. Hannon, S. De Souza-Machado, H. E. Motteler, and D. Tobin, 2003: An overview of the AIRS radiative transfer model. *IEEE Trans. Geosci. Remote Sens.*, **41**, 303–313, doi:10.1109/TGRS.2002.808244. http://ieeexplore.ieee.org/document/1196048/.

Sun, B., G. W. Kattawar, P. Yang, and E. Mlawer, 2017a: An improved small-angle approximation for forward scattering and its use in a fast two-component radiative transfer method. *J. Atmos. Sci.*, **74**, 1959–1987, doi:10.1175/JAS-D-16-0278.1. http://journals.ametsoc.org/doi/10.1175/JAS-D-16-0278.1.

Sun, B., P. Yang, G. W. Kattawar, and X. Zhang, 2017b: Physical-geometric optics method for large size faceted particles. *Opt. Express*, **25**, 24044, doi:10.1364/OE.25.024044. https://www.osapublishing.org/abstract.cfm?URI=oe-25-20-24044.

Tynes, H. H., G. W. Kattawar, E. P. Zege, I. L. Katsev, A. S. Prikhach, and L. I. Chaikovskaya, 2001: Monte Carlo and multicomponent approximation methods for vector radiative transfer by use of effective Mueller matrix calculations. *Appl. Opt.*, **40**, 400, doi:10.1364/AO.40.000400. https://www.osapublishing.org/abstract.cfm?URI=ao-40-3-400.

Wang, C., P. Yang, and X. Liu, 2015: A high-spectral-resolution radiative transfer model for simulating multilayered clouds and aerosols in the infrared spectral region. *J. Atmos. Sci.*, **72**, 926–942, doi:10.1175/JAS-D-14-0046.1. http://journals.ametsoc.org/doi/10.1175/JAS-D-14-0046.1.

Wang, C., P. Yang, S. L. Nasiri, S. Platnick, B. A. Baum, A. K. Heidinger, and X. Liu, 2013: A fast radiative transfer model for visible through shortwave infrared spectral reflectances in clear and cloudy atmospheres. *J. Quant. Spectrosc. Radiat. Transf.*, **116**, 122–131, doi:10.1016/j.jqsrt.2012.10.012. http://dx.doi.org/10.1016/j.jqsrt.2012.10.012.

Wendisch, M. and P. Yang, 2012: *Theory of atmospheric radiative transfer: A compresensive introduction*. Wiley-VCH, Weinheim, Germany.

Winker, D. M., M. A. Vaughan, A. Omar, Y. Hu, K. A. Powell, Z. Liu, W. H. Hunt, and S. A. Young, 2009: Overview of the CALIPSO mission and CALIOP data processing algorithms. *J. Atmos. Ocean. Technol.*, **26**, 2310–2323, doi:10.1175/2009JTECHA1281.1. http://journals.ametsoc.org/doi/abs/10.1175/2009JTECHA1281.1.

Wiscombe, W. J., 1976: Extension of the doubling method to inhomogeneous sources. *J. Quant. Spectrosc. Radiat. Transf.*, **16**, 477–489, doi:10.1016/0022-4073(76)90083-2. http://linkinghub.elsevier.com/retrieve/pii/0022407376900832.

Wiscombe, W. J., 1977: The Delta– M method: Rapid yet accurate radiative flux calculations for strongly asymmetric phase functions. *J. Atmos. Sci.*, **34**, 1408–1422, doi:10.1175/1520-0469(1977)034<1408:TDMRYA>2.0.CO;2. http://journals.ametsoc.org/doi/abs/10.1175/1520-0469%281977%29034%3C1408%3ATDMRYA%3E2.0.CO%3B2.

Xu, G., B. Sun, S. D. Brooks, P. Yang, G. W. Kattawar, and X. Zhang, 2017: Modeling the inherent optical properties of aquatic particles using an irregular hexahedral ensemble. *J. Quant. Spectrosc. Radiat. Transf.*, **191**, 30–39, doi:10.1016/j.jqsrt.2017.01.020. https://linkinghub.elsevier.com/retrieve/pii/S0022407316306598.

Yang, P., L. Bi, B. A. Baum, K.-N. Liou, G. W. Kattawar, M. I. Mishchenko, and B. Cole, 2013: Spectrally consistent scattering, absorption, and polarization properties of atmospheric ice crystals at wavelengths from 0.2 to 100 μ m. *J. Atmos. Sci.*, **70**, 330–347, doi:10.1175/JAS-D-12-039.1. http://journals.ametsoc.org/doi/abs/10.1175/JAS-D-12-039.1.

Yang, P., J. Ding, R. L. Panetta, K. Liou, G. W. Kattawar, and M. Mishchenko, 2019: On the convergence of numerical computations for both exact and approximate solutions for electromagnetic scattering by nonspherical dielectric particles. *Prog. Electromagn. Res.*, **164**, 27–61. http://www.jpier.org/PIER/pier.php?paper=18112810.

Zhai, P.-W., Y. Hu, J. Chowdhary, C. R. Trepte, P. L. Lucker, and D. B. Josset, 2010: A vector radiative transfer model for coupled atmosphere and ocean systems with a rough interface. *J. Quant. Spectrosc. Radiat. Transf.*, **111**, 1025–1040, doi:10.1016/j.jqsrt.2009.12.005. http://dx.doi.org/10.1016/j.jqsrt.2009.12.005.

Zhai, P.-W., Y. Hu, C. R. Trepte, and P. L. Lucker, 2009: A vector radiative transfer model for coupled atmosphere and ocean systems based on successive order of scattering method. *Opt. Express*, **17**, 2057, doi:10.1364/OE.17.002057. https://www.osapublishing.org/oe/abstract.cfm?uri=oe-17-4-2057.

Zhai, P.-W., Y. Hu, D. M. Winker, B. A. Franz, J. Werdell, and E. Boss, 2017: Vector radiative transfer model for coupled atmosphere and ocean systems including inelastic sources in ocean waters. *Opt. Express*, **25**, A223, doi:10.1364/OE.25.00A223. https://www.osapublishing.org/abstract.cfm?URI=oe-25-8-A223.

Zhang, X. and D. J. Gray, 2015: Backscattering by very small particles in coastal waters. *J. Geophys. Res. Ocean.*, **120**, 6914–6926, doi:10.1002/2015JC010936. http://doi.wiley.com/10.1002/2015JC010936.

Zhang, X., R. H. Stavn, A. U. Falster, J. J. Rick, D. Gray, and R. W. Gould, 2017: Size distributions of coastal ocean suspended particulate inorganic matter: Amorphous silica and clay minerals and their dynamics. *Estuar. Coast. Shelf Sci.*, **189**, 243–251, doi:10.1016/j.ecss.2017.03.025. http://dx.doi.org/10.1016/j.ecss.2017.03.025.